May 2021

First Principles Methods for Calculating Thermoelectric Transport Properties

Fanchen Meng
Clemson University, fanchem@g.clemson.edu

First Principles Methods for Calculating Thermoelectric Transport Properties

---

A Dissertation
Presented to
the Graduate School of
Clemson University

In Partial Fulfillment
of the Requirements for the Degree
Doctor of Philosophy
Physics

---

by
Fanchen Meng
May 2021

Accepted by:
Dr. Jian He, Committee Chair
Dr. Feng Ding
Dr. Huijuan Zhao
Dr. Endre Takacs

Abstract

Thermoelectricity, as a substantial energy form alternate to the traditional fossil fuels, has attracted tremendous attentions nowadays. The energy conversion efficiency of the thermoelectric device is mainly governed by the dimensionless thermoelectric figure of merit (*aka* zT) of thermoelectric materials, which consists of both electrical and phonon transport properties. Nowadays, the exploration of high figure of merit thermoelectric materials still rely greatly on the experimental efforts due to the lack of first principles methods for calculating the thermoelectric transport properties. Comparing with the computational methods for the phonon transport properties (*aka* lattice thermal conductivity), which can be calculated considering the phonon-phonon interactions as the scattering term in the Boltzmann transport equation (BTE), the first principles methods for calculating the electrical transport properties fall behind. Till now, the most common methods for calculating the electrical transport properties usually employ the combination of BTE along with the relaxation time approximation. The human-adjustable and single-value nature of the relaxation time makes this calculation scheme for the electrical conductivity lack physical meaning and predictive power.

In this dissertation, we developed first principles algorithms for calculating the electrical transport properties using the electron-phonon interaction as the scattering term in the electron BTE, which can be combined with available methods for phonon

transport properties to provide a full description of the thermoelectric figure of merit. The complete methodology is presented in Chapter 2. Although 3C-SiC possesses a simple structure, the polar nature of this material makes it a good candidate to examine the accuracy of our algorithms for calculating the electrical transport properties. The calculated charge carrier (both electron and hole) mobilities as a function of temperature agree well with the experimental results. Besides, a temperature dependent scattering mechanism is observed through our calculations in Chapter 3.

Despite the excellent thermoelectric performance of n-type Mg_3Sb_2, the low thermoelectric figure of merit of the p-type counterpart prevents this material from practical applications. In Chapter 4 of this dissertation, we presented our work on the anisotropic transport properties of both n- and p-type Mg_3Sb_2, which are hard to explore experimentally. Our calculated n-type thermoelectric figure of merit using the methods developed in Chapter 2 is in excellent agreement with the experimental value, showing the excellent predictive power of our methods. Most importantly, strong anisotropic thermoelectric figure of merit of the p-type Mg_3Sb_2 is observed, with the out-of-plane figure of merit beyond unity, making it possible for device applications. Moreover, we further proposed through highly oriented polycrystalline samples, it is possible to greatly improve the p-type performance of Mg_3Sb_2 experimentally.

Nanomaterials, especially the two-dimensional materials, have drawn great attentions these days after the discovery of graphene. Although it remains challenging to measure the thermoelectric transport properties of two-dimensional materials experimentally, it can be easily calculated using our algorithms developed in Chapter 2. In Chapter 5, we presented our work on the thermoelectric transport properties of two-dimensional α-Tellurium (α-Te). We found despite the thermoelectric figure of merits of both n-type and p-type two-dimensional α-Te are already promising compared with other two-dimensional materials, small tensile strain (less than 4%) could

further boost the n-type thermoelectric performance. However, the tensile strain has a negative effect on the p-type thermoelectric properties. Lastly, in Chapter 6, we discussed possible future efforts following the vein of the first principles methods for calculating the thermoelectric transport properties.

Dedication

This dissertation is dedicated to my mother.

Acknowledgments

Foremost, I would like to express my sincere gratitude to my advisor, Dr. Jian He, for the continuous support of my Ph.D. study and related research. He has been patient, supportive, and helped with my research and writing of this dissertation. I am grateful for having the opportunity to work on several projects and for the knowledge I gained while working with him.

Thanks also go to my co-mentors, without whom the work could not be done. They are Dr. Wu Li from Shenzhen University, China and Dr. Jingsong Huang from Oak Ridge National Lab, US for their support and guidance in the theoretical/computational techniques. Dr. Li, thank you for your kind host every time I visited your group, especially the one following the International Thermoelectric Society Summer Fellowship in 2018. Dr. Huang, thank you for your wisdom and critical thinking not only on the scientific topics but also on daily life, which inspired me a lot.

Additionally, I am grateful to the rest committee members: Dr. Feng Ding, Dr. Huijuan Zhao and Dr. Endre Takacs for their encouragement and insightful advice and guidance on this dissertation.

My gratitude extends to the current or former group members in Drs. He's, Tritt's and Li's lab: Dr. Yufei Liu, Dr. Menghan Zhou, Dr. Xiaoyu (Bella) Zeng, Dr. Jinlong Ma, Mr. Allen Benton, Ms. Samantha Hardin, Mr. Charles Chronister, Ms.

Yamei Liu for their fruitful discussions and suggestions. I would also like to thank my friends I meet at Clemson: Dr. Jingyi Zhu, Dr. Yunxiang Sun, Dr. Chuanchang Zheng, Dr. Lin Li, Dr. Jia Zhe, Dr. Andrew Garmon, Mr. Xiurui Zhao, Ms. Yang Yang, Mr. Chi Zhang, Mr. Tu Lyu, Dr. Jintai Li, Mr. Haonan Wu, Ms. Mengke Li, Mr. Zhiyuan Song and Mr. Chendi Xie. My life at Clemson would not be so colorful and pleasant without you.

Taking this opportunity, I would also like to acknowledge my best friends back in China, Mr. Yang Yang, Mr. Chao Hou, Mr. Song Song, Mr. Jie Yu, Ms. Chen Li, Dr. Xiangnan Chen, Dr. Songsong Sun for taking care of my family while I am overseas.

Last but not least, I would like to thank my parents, relatives and especially, my fiancée Ms. Zhenzhen Zhang for their endless love, support and encouragement.

Table of Contents

List of Tables

List of Figures

Chapter 1

Introduction to Thermoelectricity and Electron-phonon Interactions

Energy consumption is an important issue getting significant attentions from the entire world. Till now, most common energy resources still come from the burning of the fossil fuels, such as petroleum, coal, natural gas, *etc*. According to an annual report from Lawrence Livermore National Laboratory, in the year 2019, the energy rejected (wasted) was twice the amount of the energy utilized. These data indicate serious problems with the energy consumption structure on both ends: the resources and the usage. To tackle this problem, one can deal with the resource end, that is to use clean and sustainable energy, such as the wind, solar, nuclear, *etc*, instead of the fossil fuels; while on the usage end, one can focus on re-utilizing (harvesting) the wasted energy. If 20% of the wasted energy can be harvested, it is comparable to building 10-30 nuclear power plants for free. Since most of the energy is wasted in the form of thermal energy (heat), it is natural to seek methods to convert the wasted heat back into power that can be used.

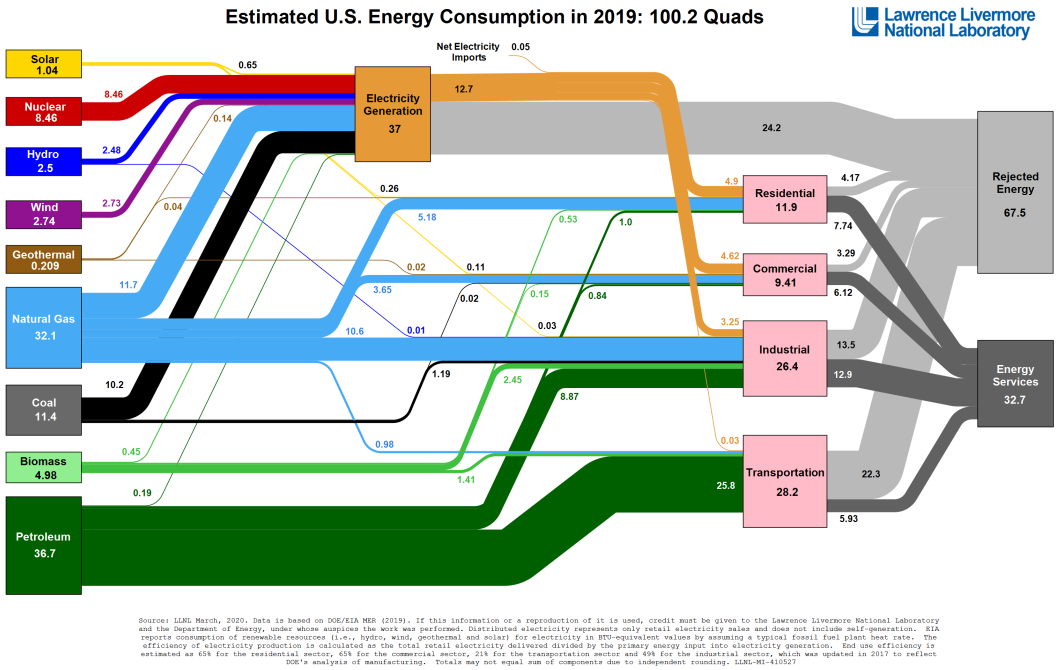

Figure 1.1: 2019 Energy Consumption in the United States.

1.1 Brief Introduction to Thermoelectrics

Thermoelectrics can be traced back to the year 1821. Thomas Johann Seebeck, a German scientist, found a magnetic needle was deflected if a temperature difference was maintained on two materials in a closed loop. [31] A few years later, a French scientist, Jean Peltier, discovered a temperature difference across the junction of two dissimilar conducting materials in a closed loop when a current was driven through the loop. [32] These two effects (Seebeck effect and Peltier effect) constructing the foundation of thermoelectrics are named after these two famous scientists. [33]

1.1.1 Seebeck effect and Peltier effect

Seebeck effect

In a particle-like picture, the microscopic origin of the Seebeck effect can be

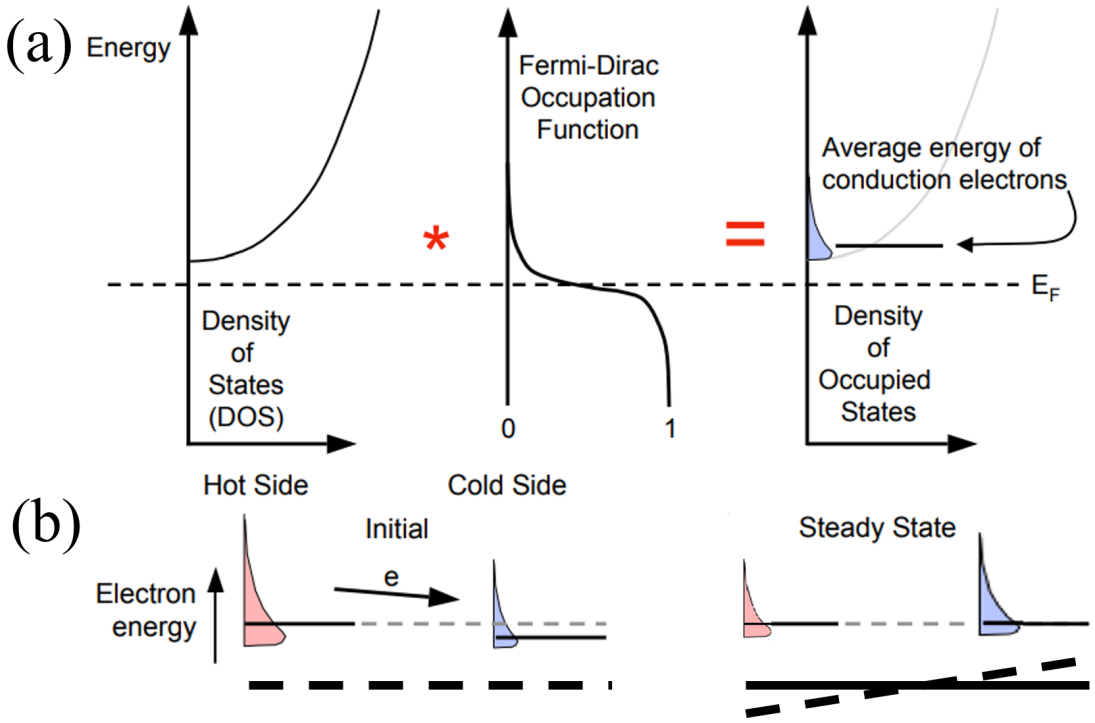

Figure 1.2: Schematic diagram of (a) density of occupied states in n-type semiconductor and its decomposition to density of states and Fermi-Dirac occupation function and (b) the electron diffusion in the n-type semiconductor when a temperature difference is held at the two ends. [1] We have modified this figure from its original form to reflect the density of occupied states on the right (cold) end is much larger than the one on the left (hot) end in the final steady state as a result of carrier diffusion, and the fact that the chemical potential on the left (cold) end is lowered while the chemical potential on the right (hot) end is elevated.

understood as follows. Taking a semiconductor under a temperature difference as an example without losing generality, the chemical potential at the two ends tend to stay the same as in the equilibrium state at the moment an external temperature gradient is applied at the two ends of the semiconductor (Figure 1.2). Heat excites charge carriers (either electrons or holes) according to the Fermi-Dirac distribution. Therefore, both the number of charge carriers and the average energy of charge carriers at the hot end tend to be higher than the counterparts at the cold end. Then, hot charge carriers, driven by the difference in the average energy, diffuse from the hot end towards the

cold end, with charge carriers with one sign (either positive or negative) accumulating at the cold end and the charge carriers with the opposite sign accumulating at the hot end [2], developing an internal electric field between the hot and cold ends. At the final steady state, the resultant electric field counterbalances the further diffusion of hot charge carriers (Figure 1.3). Alternatively, one can image this process as the accumulation of charge carriers at the cold end shifts the local chemical potential in such a way that the average energy of the charge carriers at the hot and cold end equal each other. Consequently, a potential difference is built up due to the temperature difference. This phenomenon is called the absolute Seebeck effect.

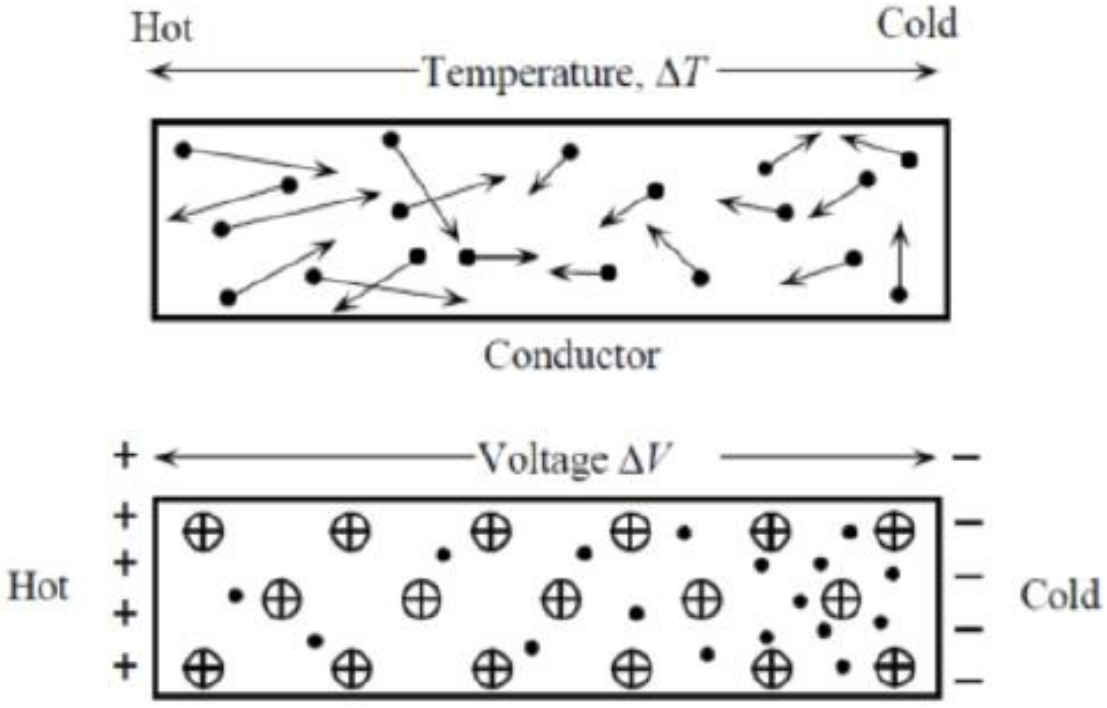

Figure 1.3: Representation of diffusion of carriers under temperature gradient in an electric conductor (upper panel) and finally a steady electric field builds up in the conductor (bottom panel). [2]

In addition, there is also a relative Seebeck effect, where a thermocouple consisting of two dissimilar electric conductors is involved (Figure 1.4 (a)). In the ther-

mocouple, the two junctions between the two dissimilar materials (A and B in Figure 1.4 (a)) are kept at different temperatures T_h and T_c with $T_h > T_c$. A potential difference V can be measured between the two junctions, which is defined as:

$$V = \alpha_{AB} \times (T_h - Tc), \tag{1.1}$$

where α_{AB} is the relative Seebeck coefficient between the two materials.

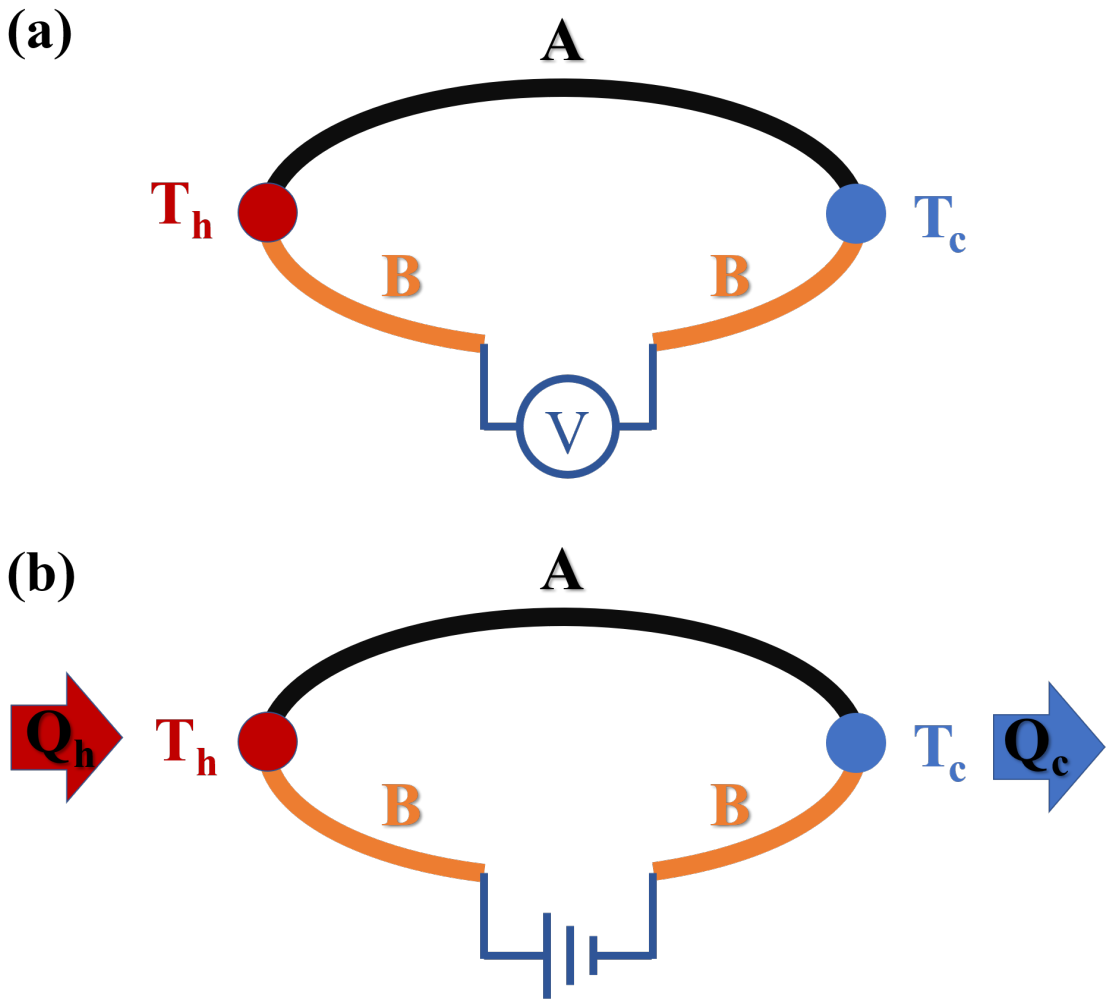

Figure 1.4: Schematic diagram of (a) Seebeck effect and (b) Peltier effect.

Peltier Effect

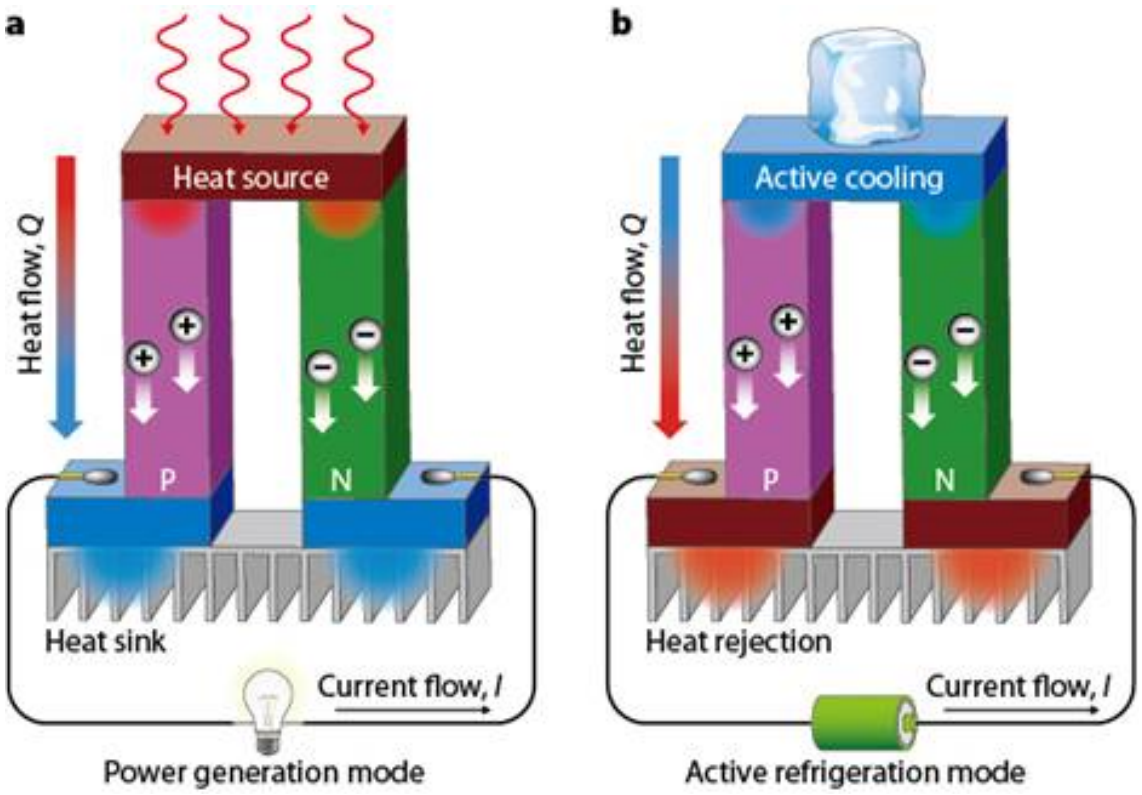

Figure 1.5: Schematic diagram for thermoelectric generator and cooler. [3]

If a current is driven through the thermocouple, heat is absorbed at one of the junctions, and released at the other (Figure 1.4 (b)). This is called the (relative) Peltier effect. Unlike Seebeck effect, Peltier effect can only be observed in dissimilar materials (relative Peltier effect). This is because the Peltier effect originates from the different chemical potential of the two materials in the closed circuit. In the closed circuit, when the charge carriers move from the high (low) chemical potential side to the low (high) chemical potential side due to the driven current, energy is released (absorbed). It is interesting to note that the Peltier effect should not be regarded as the exact inverse of the Seebeck effect because the Seebeck effect is observed in an open circuit, while Peltier effect is observed in a closed circuit. Suppose the current driven in the closed circuit is I, the heat absorption or emission rate can be expressed

as:

$$q = \Pi_{AB} I \tag{1.2}$$

where Π_{AB} is the relative Peltier coefficient similar to the relative Seebeck coefficient. It is obvious from Equation 1.2 that the heat absorption or emission rate is proportional to the current driven through the closed circuit.

1.1.2 Thermoelectric Generator and Cooler

The Seebeck effect discussed above provides the foundation for a thermoelectric generator. Figure 1.5(a) depict the schematic diagram of a thermoelectric generator consisting of both n-type and p-type semiconductors (*aka* n- and p-thermoelectric legs). When a temperature difference is maintained at the two junctions of two thermoelectric legs, more electrons in the n-type semiconductor and more holes in the p-type semiconductor are excited at the hot side. Under the influence of the concentration gradient, the electrons (holes) in the n-leg (p-leg) would diffuse from the hot side to the cold side, building a voltage difference between the two ends of the generator.

Thermoelectric cooler, which can be regarded as the inverse of the thermoelectric generator, is based on the Peltier effect. Similar to the thermoelectric generator, a thermoelectric cooler also consists of n-legs and p-legs, which are connected electrically in series and thermally in parallel. The schematic diagram for a thermoelectric cooler is depicted in Figure 1.5 (b). When a current is driven through the closed series loop, electrons in the n-legs would move in the direction opposite to that of the applied current; in the meanwhile, holes in the p-legs would move in the same direction as the current. When the charge carriers move from one junction to the other, energy carried by the charge carrier is released or absorbed depending on the average

energy of the charge carriers. As can be seen from Figure 1.5 (b), both electrons in the n-legs and holes in the p-legs run away from the top junction towards the bottom junction carrying heat with them, which finally results in the top junction cooled and the bottom junction heated. It should be noted that if the current in Figure 1.5 (b) is reversed, the cooling (heating) effect would occur at the top (bottom) junctions.

1.1.3 Thermoelectric Conversion Efficiency

The efficiency of a thermoelectric device, η, is given by Equation 1.3, where $\overline{zT}$ is the average figure of merit over the whole working temperature range, with T_C and T_H being the temperatures at the cold and hot ends, respectively.

$$\eta = \frac{T_H - T_C}{T_H} \times \frac{\sqrt{1 + \overline{zT}} - 1}{\sqrt{1 + \overline{zT}} + T_C/T_H} \tag{1.3}$$

According to the Equation 1.3, the thermoelectric conversion efficiency is constrained by the Carnot limit and the dimensionless figure of merit or the zT values. [34] It should be noted the zT values are the properties of materials. Therefore, Equation 1.3 is the linkage between the thermoelectric conversion efficiency and the thermoelectric materials. Figure 1.6 is represented to have a better visualization of the relationship between the thermoelectric device efficiency and the average figure of merit.

1.1.4 Thermoelectric Figure of Merit

As mentioned above, the dimensionless figure of merit or zT value which is used to characterize the performance of a thermoelectric material, is defined as [35]

$$zT = \frac{\alpha^2 \sigma T}{\kappa} \tag{1.4}$$

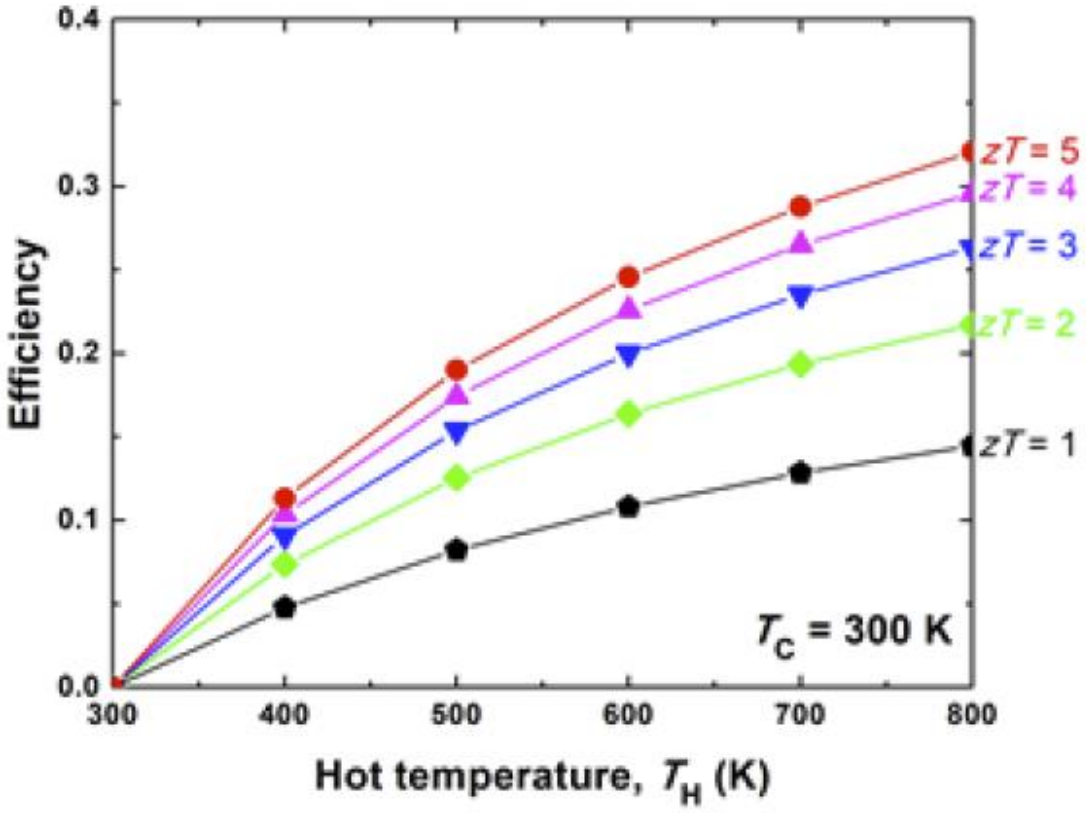

Figure 1.6: Thermoelectric device efficiency as a function of the hot-end temperature under the assumption that the cold-end is kept fixed at 300 K [4].

where α is the Seebeck coefficient, σ is the electrical conductivity, T is the absolute temperature, and κ is the total thermal conductivity contributed from charge carriers κ_e and phonons κ_L, respectively. P-type semiconductors, in which holes are the majority carriers, possess positive Seebeck coefficient, while n-type semiconductors exhibit negative Seebeck coefficient because the electrons are majority carriers. The power factor (PF) is defined as the product of α^2 and σ in Equation 1.5, which is mainly used to describe the electrical performance of a thermoelectric material.

$$PF = \alpha^2\sigma \tag{1.5}$$

1.2 Experimental Efforts to Explore High Figure of Merit

1.2.1 Optimizing the Carrier Concentration

All the physical quantities except κ_L in Equation 1.4 are coupled to each other as functions of carrier concentration, n. n is governed by the doping level, temperature, and defects. In general, the electrical conductivity increases as the carrier concentration increases. On the contrary, the Seebeck coefficient decreases with increase of the carrier concentration (Figure 1.7). As a result, there is no ideal method to optimize these quantities (except κ_L) separately. However, according to Figure 1.7, through optimizing the carrier concentration, it is possible that the power factor reaches an optimal value. The optimal carrier concentration of different thermoelectric materials differs from each other. However, it generally falls in the range 10^{18}-10^{20} cm^{-3}, which usually belongs to the range for the degenerate semiconductors. [35] Therefore, to optimize the power factor requires doping, alloying or other strategies to tune the carrier concentration. In addition, it is verified in Bi_2Te_3 that it is possible to tune the intrinsic point defect in Bi_2Te_3 through extrinsic doping, which in turn helps optimize the carrier concentration. [36]

However, it should be noted that the optimal carrier concentration for zT and power factor is different, which is due to that the optimal carrier concentration for power factor benefits not only the electrical performance but also the electrical thermal conductivity. With increasing electrical thermal conductivity, the total thermal conductivity is also elevated, negatively affecting the final zT. Therefore, the optimal carrier concentration for maximum zT should be slightly lower that corresponding to the maximum power factor.

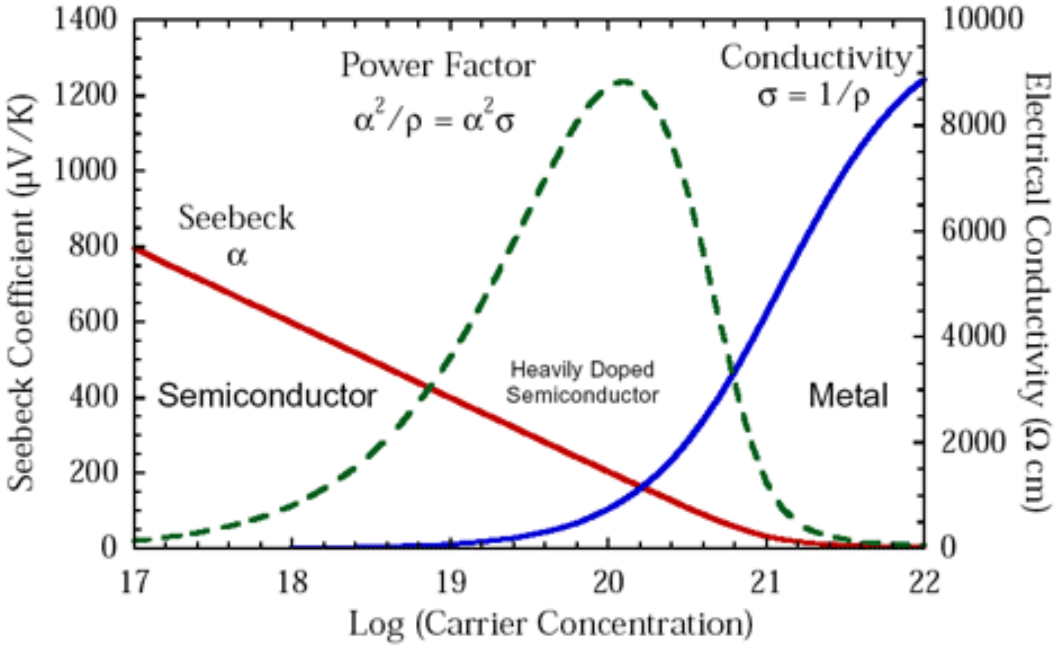

Figure 1.7: Relationship between the electrical transport properties (Seebeck coefficient, electrical conductivity, and power factor) and the carrier concentration [5].

1.2.2 Band Engineering

At a fixed carrier concentration, it is possible to further optimize the thermoelectric performance *via* band engineering. According to Equation 1.6,

$$\alpha = \frac{8\pi^2}{3}\frac{k_B^2 T}{eh^2} m^* \left(\frac{\pi}{3n}\right)^{\frac{2}{3}} \tag{1.6}$$

the Seebeck coefficient is not only determined by the carrier concentration but also proportional to the density of state (DOS) effective mass, indicating increasing the DOS effective mass of charge carrier, the Seebeck coefficient could be elevated. As can be seen from the DOS effective mass expression $m^* = N_v^{2/3} m_b^*$ [6, 37], where N_v is the band valley degeneracy and m_b^* is the band effective mass, that increasing N_v or m_b^* could increase the DOS effective mass, thus further optimizing the thermoelectric

performance. On the other hand, it should be noted that if the charge carrier is mainly scattered by phonons, which is usually the case for thermoelectric materials especially at high temperatures, the charge carrier and the band effective mass has a relation $\mu \propto 1/m_b^{*5/2}$ [6, 37]. In the meanwhile, according to the Drude model, $\sigma = nq\mu$, at a fixed carrier concentration, the carrier mobility is determinant for the electrical conductivity. Therefore, increasing the band effective mass must be accompanied by sacrificing the electrical conductivity and thus the thermoelectric performance. Compared to increasing the band effective mass, increasing the band valley degeneracy is more effective method to enhancing the DOS effective mass [38].

Some thermoelectric materials with high symmetry, such as PbTe, SnTe and half-Heusler [38] possess intrinsic large valley degeneracy if the band extrema deviate from the Gamma point in the Brillouin zone. In addition, through methods like alloying, it is possible to tune the position of the energy band, decreasing the energy difference between the light band and heavy band, *aka* the band convergence, which could also increase the band valley degeneracy. For example, Pei *et al.* [6] found in PbTe that the light valence band at the L point in the Brillouin zone moves downwards in the energy scale and merged with the heavy band at the Σ point, realizing the band convergence as in Figure 1.8. The number of the band valleys that contribute to the conduction of the charge carrier increases from 4 to 16 (4 from L point and 12 from the Σ point), leading to a great increase in the DOS effective mass, thus the Seebeck coefficient. Besides, through Rashba effect it is also possible to fulfill the band convergence. [39]

Apart from the methods mentioned above, introducing resonant level could also increase the Seebeck coefficient [40, 41]. Resonant level, like impurity level, is usually introduced by the dopants. Unlike the common impurity level, which usually lies inside the band gap of a semiconductor, the resonant level locates in the

conduction band or valence band depending on the type of dopants. Accordingly, the DOS shows a spike, which is beneficial in increasing the DOS effective mass. Typical examples include Tl doped PbTe [42], Al doped PbSe [43] and In doped SnTe [44], *etc.*

1.2.3 Efforts to Decrease Lattice Thermal Conductivity

As mentioned above, lattice thermal conductivity is the factor that could be decoupled from the electrical transport parameters, which could be optimized separately. In recent years, more and more methods to reducing the lattice thermal conductivity have been reported. For example, the multi-scale scattering center introduced by defect engineering could help shorten the phonon mean free path [45], thus decreasing the lattice thermal conductivity. From the dimensional viewpoint, in general, defects can be categorized into zero-dimensional (point defect), one-dimensional (dislocation), two-dimensional (grain boundary) and three-dimensional (nano inclusion or secondary phase) [46]. Point defect, including vacancy [47, 48], doping or alloying [49] and interstitial atoms [50], can scatter high-frequency phonon effectively. High density dislocation can scatter mid-frequency phonons, which can be introduced *via* plastic deformation of the samples. Large amount of grain boundaries can be introduced *via* grain refinement and nano-structuring, thus forming high density grain boundary scattering centers, which can scatter low-frequency phonons. However, it should be noted that the high density grain boundary scattering center not only scatters the low-frequency phonon but the charge carriers, which has negative effect on the electrical performance. Introducing the above discussed defects into one sample, we can construct multi-frequency and multi-scale scattering centers, thus realizing the reduction of lattice thermal conductivity. For instance, Biswas *et al.* introduced

the multi-scale scattering centers into PbTe and achieved a zT around 2.2 at 915 K [51].

In addition, the lattice thermal conductivity can also be effectively reduced *via* lattice anharmonicity [52], complex crystal structure[53], porous structure [54, 55], and introducing heavy element or weak chemical bonding [56].

1.2.4 Pre-screening Factor

It can be inferred from the discussion above that to explore the high performance thermoelectric materials, there are large amounts of work to be done experimentally due to the large phase space for the parent compounds to be dealt with, not to mention the fine-tuning of the electrical and thermal transport properties *via* doping or alloying. To reduce the size of the phase space, experimentalists came up with some pre-screening factor for excellent thermoelectric materials, such as degenerate semiconductors with carrier concentration between 10^{18} and 10^{20} cm^{-3}, semiconductors with small band gap, high symmetry crystal structure, small electronegativity difference among the constituent element, *etc.*

However, even with the pre-screening factors, to enumerate all the possible case in the large phase space or to fast-target some promising candidates for thermoelectric application is a great burden from the experimental point of view. Therefore, more advanced techniques should be developed not only in the vein of experiment but also the path along the theoretical efforts.

1.3 Calculations of the Thermoelectric Figure of Merit

The calculations of the thermoelectric figure of merit involves two parts: (i) the electrical transport properties, such Seebeck coefficient, electrical conductivity and electrical thermal conductivity; (ii) the phonon transport properties (*aka* lattice thermal conductivity). Solving the phonon Boltzmann transport equation (BTE) is an easy but efficient way to calculate both the electrical transport properties and phonon transport properties.

1.3.1 Phonon Transport Properties

In the presence of a temperature gradient ∇T, the Bose-Einstein distribution of a phonon mode, f, deviates from f^0, and this deviation can be obtained from the BTE. The phonon distribution function is influenced by both the diffusion due to the temperature gradient and the scattering from possible scattering processes, such as phonon-phonon scattering, phonon-isotope scattering, electron-phonon scattering, *etc.* For a steady state, the changing rate of the phonon distribution function must vanish, which can be expressed by the BTE [57, 58]:

$$-\mathbf{v}_{\mathbf{q}p} \cdot \nabla T \frac{\partial f_{\mathbf{q}p}}{\partial T} + \frac{\partial f_{\mathbf{q}p}}{\partial t}|_{scatt} = 0 \tag{1.7}$$

where $\mathbf{q}$ and p represent the wave vector and phonon band branch of a phonon mode. In the following, we will use λ to denote the phonon mode with wave vector $\mathbf{q}$ and phonon band branch p. v_λ is the phonon group velocity. In Equation 1.7, the first term is the temperature gradient induced diffusion term, and the second term is the scattering processes governed scattering term. Under a small temperature gradient,

the phonon BTE can be linearized with $f_\lambda = f_\lambda^0 + f_\lambda^0(1+f_\lambda^0)\Phi_\lambda$, where Φ_λ is a small perturbation. If only three-phonon processes within the phonon-phonon scattering are considered for the scattering term, the linearized phonon BTE can be written as [59, 60]

$$-\mathbf{v}_\lambda \cdot \nabla T \frac{\partial f_\lambda^0}{\partial T} = \frac{f_\lambda^0 (1+f_\lambda^0)}{N} \times \sum_{\lambda' \lambda''} \left[\left(\Phi_\lambda + \Phi_{\lambda'} - \Phi_{\lambda''}\right) \Gamma^+_{\lambda\lambda'\lambda''} + \frac{1}{2} \left(\Phi_\lambda - \Phi_{\lambda'} - \Phi_{\lambda''}\right) \Gamma^-_{\lambda\lambda'\lambda''} \right] \tag{1.8}$$

where a discretization of the Brillouin zone into a Gamma-point-centered regular grid of $N = N1 \times N2 \times N3$ $\mathbf{q}$ points is employed, with $N1$, $N2$ and $N3$ being the number of divisions along the three principal axes in the Brillouin zone. $\Gamma^+_{\lambda\lambda'\lambda''}$ and $\Gamma^-_{\lambda\lambda'\lambda''}$ are the transition rates due to the three phonon absorption (+) and emission (-) processes, respectively, which can be calculated directly from first principles. [61, 62, 63, 64, 65]

With the phonon BTE solved and the distribution function f obtained, it is then possible to calculate the lattice thermal conductivity. The detailed methods are provided in Chapter 2.

1.3.2 Electrical Transport Properties

Similar to the phonon transport properties, in the presence of an external electric field $\mathbf{E}$, the Fermi-Dirac distribution of an electronic state, f, deviates from its equilibrium distribution f^0, and this deviation can be calculated using the electron BTE. The electron distribution function is affected by the diffusion due to the external electric field, and the scattering from possible scattering processes, which is mainly governed by the electron-phonon interaction for single crystal samples at high temperature. When the external electric field $\mathbf{E}$ is small, the BTE for the electrical

transport properties has the form:

$$-\frac{q\mathbf{E}}{\hbar}\frac{\partial f_{n\mathbf{k}}}{\partial \mathbf{k}} + \frac{\partial f_{n\mathbf{k}}}{\partial t}|_{scatt} = 0 \tag{1.9}$$

where q is the elementary charge, $\hbar$ is the reduced Planck constant, $\mathbf{E}$ is the external electric field, $f_{n\mathbf{k}}$ is the electron distribution function with electron wave vector $\mathbf{k}$ and band branch n.

Compared to the full solution to the phonon BTE, the development of the solution to the electron BTE falls behind. Nowadays, the common way to deal with the scattering term (the second term on the left of Equation 1.9) in the electron BTE is to use the constant relaxation time approximation with the form:

$$\frac{\partial f_{n\mathbf{k}}}{\partial t}|_{scatt} = \frac{f_{n\mathbf{k}} - f^0_{n\mathbf{k}}}{\tau} \tag{1.10}$$

where τ is the relaxation time. It should be pointed out that the relaxation time is identical for different electronic state under the constant relaxation time approximation, which is physically meaningless. In addition, despite the relaxation time could be fit from experimental data or using some empirical expressions, this type of solution to the electron BTE lacks the predictive power. Therefore, the calculations of the electrical transport properties based on the constant relaxation time approximation could only provide phenomenological explanations to the experimental results, which is also the main reason why there is much less computational research work in the thermoelectric field than the experimental work. In order to make the calculations of the electrical transport properties fully from first principles, more advanced solution to the electron BTE is in high demand.

1.4 Electron-phonon interactions

The electron-phonon interactions, where an electron exchanges energy and momentum with phonons (collective modes of the lattice vibrations), play a key role in condensed matter physics and materials science and engineering. For example, the electron-phonon interaction is responsible for the fundamental physical phenomena such as the conventional superconductivity [66], Kohn anomaly [67] and the Peierls [68] distortions, *etc*. The broadening of the spectral lines in angle-resolved photoemission spectroscopy [69] and in vibrational spectroscopy [70], phonon-assisted photon absorption [71, 72, 73] as well as for the temperature dependence of the band gaps in semiconductors [74] are consequences of the interactions between electrons and lattice vibrations.

Most important to this dissertation is that electrical conductivity and related electrical transport properties [75] have a close relation with the electron-phonon interactions. Thus, the electron-phonon interaction also plays an important role in the thermoelectric effect [76]. According to the first order perturbation theory, an electron can change its state by absorbing or emitting a phonon, corresponding to the phonon absorption process and phonon emission process, respectively. According to the Fermi golden rule, it is possible to calculate the scattering rate of each process for each electronic state. The obtained scattering rates for each electronic state can then be fed into the electron BTE, which is the advanced first principles solution to the electron BTE we desire. Finally, it is possible to calculate the electron-phonon interaction limited electrical transport properties under the framework of BTE and electron-phonon interaction. The detailed methodology is presented in Chapter 2.

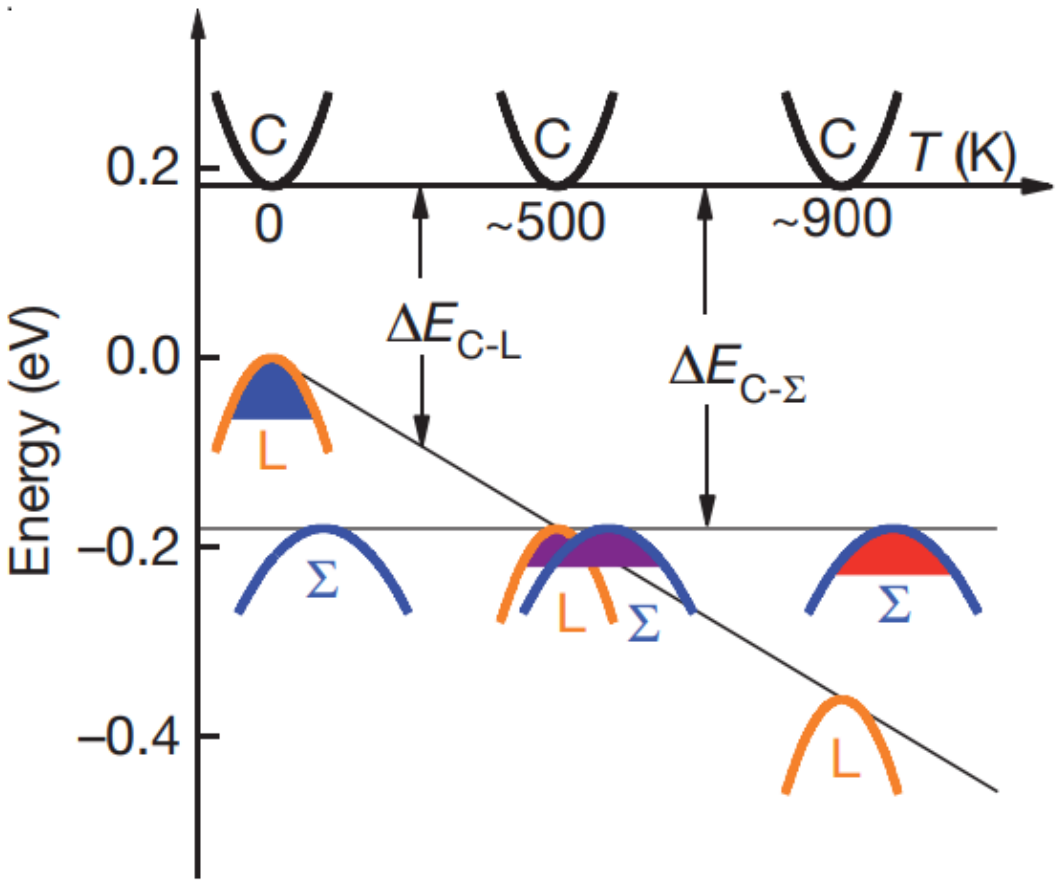

Figure 1.8: Relative energy of the valence bands in $PbTe_{0.85}Se_{0.15}$. At around 500 K the two valence bands converge, resulting in transport contributions from both the L and S bands. C denotes conduction band; L represents low degeneracy hole band; S is high degeneracy hole band. [6]. It should be noted that in the figure, only the relative shift of the band extrema makes sense since in reality it is impossible to rigidly shift the whole band.

Chapter 2

First Principles Methods for Electrical and Phonon Transport Calculations

2.1 Electrical Transport Properties

Recall the expression for the electron BTE:

$$-\frac{q\mathbf{E}}{\hbar}\frac{\partial f_{n\mathbf{k}}}{\partial \mathbf{k}} + \frac{\partial f_{n\mathbf{k}}}{\partial t}|_{scatt} = 0 \tag{2.1}$$

where q is elementary charge and $\hbar$ is the reduced Planck constant. If the external electric field $\mathbf{E}$ is small (low-field limit), $f_{n\mathbf{k}}$ could be expressed using Taylor expansion as $f_{n\mathbf{k}} = f^0_{n\mathbf{k}} + f_{n\mathbf{k}}(1 - f_{n\mathbf{k}})\Phi_{n\mathbf{k}}$, with $\Phi_{n\mathbf{k}}$ being a small perturbation which is linear with respect to $\mathbf{E}$. Therefore, it is convenient to express $\Phi_{n\mathbf{k}}$ as $\frac{q\mathbf{E}}{k_B T}\cdot F_{n\mathbf{k}}$, with k_B being the Boltzmann constant, and T being the temperature. $F_{n\mathbf{k}}$ can be considered as the mean free displacement [58, 77]. If the scattering term (second term) of Equation 2.1

is limited to the electron-phonon interactions, Equation 2.1 can be linearized [77]:

$$\mathbf{F}_{n\mathbf{k}} = \mathbf{v}_{n\mathbf{k}}\tau^0_{n\mathbf{k}} + \tau^0_{n\mathbf{k}} \sum_{\mathbf{q}pm} (\Gamma^{m\mathbf{k}+\mathbf{q}}_{n\mathbf{k},\mathbf{q}p} + \Gamma^{m\mathbf{k}+\mathbf{q},-\mathbf{q}p}_{n\mathbf{k}})\mathbf{F}_{m\mathbf{k}+\mathbf{q}}, \tag{2.2}$$

where $\mathbf{q}p$ represents the phonon mode with branch p and wave vector $\mathbf{q}$, $\mathbf{v}_{n\mathbf{k}}$ describes the group velocity of carrier defined as $\mathbf{v}_{n\mathbf{k}} = \frac{1}{\hbar}\frac{\partial \mathbf{E}_{n\mathbf{k}}}{\partial \mathbf{k}}$, and $\tau^0_{n\mathbf{k}}$ is the relaxation time which could be calculated as $[\sum_{\mathbf{q}pm} (\Gamma^{m\mathbf{k}+\mathbf{q}}_{n\mathbf{k},\mathbf{q}p} + \Gamma^{m\mathbf{k}+\mathbf{q},-\mathbf{q}p}_{n\mathbf{k}})]^{-1}$. Here, $\Gamma^{m\mathbf{k}+\mathbf{q}}_{n\mathbf{k},\mathbf{q}p}$ and $\Gamma^{m\mathbf{k}+\mathbf{q},-\mathbf{q}p}_{n\mathbf{k}}$ are transition rates for phonon absorption and emission processes, respectively [77], which can be obtained from electron-phonon coupling strength calculated *via* first principles method as:

$$\Gamma^{m\mathbf{k}+\mathbf{q}}_{n\mathbf{k},\mathbf{q}p} = \frac{2\pi}{\hbar}|g^{m\mathbf{k}+\mathbf{q}}_{n\mathbf{k},\mathbf{q}p}|^2(f^0_{\mathbf{k}+\mathbf{q}} + N^0_{\mathbf{q}p}) \times \delta(E_{n\mathbf{k}} + \hbar\omega_{\mathbf{q}p} - E_{m\mathbf{k}+\mathbf{q}}), \tag{2.3}$$

$$\Gamma^{m\mathbf{k}+\mathbf{q},-\mathbf{q}p}_{n\mathbf{k}} = \frac{2\pi}{\hbar}|g^{m\mathbf{k}+\mathbf{q}}_{n\mathbf{k},\mathbf{q}p}|^2(1 + N^0_{-\mathbf{q}p} - f^0_{m\mathbf{k}+\mathbf{q}}) \times \delta(E_{n\mathbf{k}} - \hbar\omega_{-\mathbf{q}p} - E_{m\mathbf{k}+\mathbf{q}}), \tag{2.4}$$

where $g^{m\mathbf{k}+\mathbf{q}}_{n\mathbf{k},\mathbf{q}p}$ is the electron-phonon interaction matrix element, N^0 is the Bose-Einstein distribution function for phonons, f^0 denote the Fermi-Dirac function for electrons and the δ function guarantees the conservation of energy and momentum during the scattering process.

Equation 2.2 can be solved iteratively to find $\mathbf{F}_{n\mathbf{k}}$, which is also called the exact solution. This method has been successfully applied to studying phonon transport properties [58, 78, 79] for a few years, but has not been introduced to the study of electron transport properties until very recently [77, 80, 81, 82, 83]. For the exact solution to $\mathbf{F}_{n\mathbf{k}}$, the $\mathbf{k}$ and $\mathbf{q}$ grids are required to be commensurate [84, 85]. Besides the exact solution, for comparison, two more solutions are also implemented in our calculations, which are the conventional relaxation time approximation (conventional RTA) method and momentum relaxation time approximation (momentum-RTA) method.

Conventional RTA neglects the sum term (second term) on the right-hand side of Equation 2.2. Momentum RTA also neglects this sum but further takes account for the relative change of momentum in each scattering process by multiplying the transition rates involved in $\tau^0_{n\mathbf{k}}$ by an efficiency factor of [77]

$$\lambda = 1 - \frac{\mathbf{v}_{n\mathbf{k}} \cdot \mathbf{v}_{m\mathbf{k}+\mathbf{q}}}{|\mathbf{v}_{n\mathbf{k}}|^2}. \tag{2.5}$$

At a finite temperature T, with the calculated $\mathbf{F}_{n\mathbf{k}}$, the electrical conductivity tensor can be expressed as:

$$\sigma^{\beta\gamma} = \frac{se^2}{VN_{\mathbf{k}}} \sum_{n\mathbf{k}} v^{\beta}_{n\mathbf{k}} F^{\gamma}_{n\mathbf{k}} \left(-\frac{\partial f^0_{n\mathbf{k}}}{\partial \epsilon_{n\mathbf{k}}} \right), \tag{2.6}$$

and the Seebeck coefficient as:

$$\alpha^{\beta\gamma} = \left(\sigma^{-1}\right)^{\beta\eta} \xi^{\eta\gamma}, \tag{2.7}$$

where $\xi^{\eta\gamma} = \frac{se}{TVN_{\mathbf{k}}} \Sigma_{n\mathbf{k}} \left(\epsilon_{n\mathbf{k}} - \epsilon_f\right) v^{\eta}_{n\mathbf{k}} F^{\gamma}_{n\mathbf{k}} \left(-\frac{\partial f^0_{n\mathbf{k}}}{\partial \epsilon_{n\mathbf{k}}} \right)$. With ξ defined above, the electrical thermal conductivity could be obtained as:

$$\kappa_e^{\beta\gamma} = \frac{s}{TVN_{\mathbf{k}}} \sum_{n\mathbf{k}} \left(\epsilon_{n\mathbf{k}} - \epsilon_f\right)^2 v^{\beta}_{n\mathbf{k}} F^{\gamma}_{n\mathbf{k}} \left(-\frac{\partial f^0_{n\mathbf{k}}}{\partial \epsilon_{n\mathbf{k}}} \right) - T\xi^{\beta\eta}\alpha^{\eta\gamma}, \tag{2.8}$$

In Equations 2.6-2.8, $N_{\mathbf{k}}$ is the number of $\mathbf{k}$ meshes for sampling the first Brillouin zone, V is the volume of the unit cell, and β and γ are the Cartesian directions. For example, $v^{\beta}_{n\mathbf{k}}$ is the electron velocity along β direction.

From Drude model, it is also possible to extract the carrier mobility:

$$\mu^{\beta\gamma} = \frac{\sigma^{\beta\gamma}}{n_c e}, \tag{2.9}$$

where n_c is the carrier concentration and can be calculated as $n_c = \frac{s}{N_k V} \Sigma_{n\mathbf{k}} f^0_{n\mathbf{k}}$ and

$n_c = \frac{s}{N_k V}\Sigma_{n\mathbf{k}}(1 - f^0_{n\mathbf{k}})$ for n-type and p-type semiconductors, respectively.

2.2 Lattice Thermal Conductivity

In the linearized phonon BTE in mentioned in Chapter 1 (Equation 1.7), it should be noted that the conservation of both energy ($\omega_\lambda \pm \omega_{\lambda'} = \omega_{\lambda''}$) and momentum ($\mathbf{q}_\lambda \pm \mathbf{q}_{\lambda'} = \mathbf{q}_{\lambda''} + \mathbf{G}$) must be obeyed in all the allowed scattering processes, where + and - are for absorption and emission processes, respectively, and $\mathbf{G}$ is a reciprocal lattice vector. In absorption processes, a phonon λ is scattered by absorbing a phonon λ' to yield a third phonon λ''; while in emission processes, a phonon λ decays into two phonons λ' and λ''. $\Gamma^+_{\lambda\lambda'\lambda''}$ and $\Gamma^-_{\lambda\lambda'\lambda''}$ can be expressed as [58]:

$$\Gamma^+_{\lambda\lambda'\lambda''} = \frac{\hbar\pi}{4}(f^0_{\lambda'} - f^0_{\lambda''}) \times |V^+_{\lambda\lambda'\lambda''}\|^2 \times \frac{\delta(\omega_\lambda + \omega_{\lambda'} - \omega_{\lambda''})}{\omega_\lambda\omega_{\lambda'}\omega_{\lambda''}}, \tag{2.10}$$

$$\Gamma^-_{\lambda\lambda'\lambda''} = \frac{\hbar\pi}{4}(f^0_{\lambda'} + f^0_{\lambda''} + 1) \times |V^-_{\lambda\lambda'\lambda''}|^2 \times \frac{\delta(\omega_\lambda - \omega_{\lambda'} - \omega_{\lambda''})}{\omega_\lambda\omega_{\lambda'}\omega_{\lambda''}}, \tag{2.11}$$

where

$$V^+_{\lambda\lambda'\lambda''} = \frac{\sum_{bl'b'l''b''}\sum_{\alpha\beta\gamma}\Phi^{\alpha\beta\gamma}_{0b,l'b',l''b''}\mathbf{e}^{\lambda}_{\alpha b}\mathbf{e}^{\lambda'}_{\beta b'}\mathbf{e}^{-\lambda''}_{\gamma b''}}{\sqrt{m_b m_{b'} m_{b''}}} \times e^{+i\mathbf{q}'\cdot\mathbf{r}_{l'}}e^{-i\mathbf{q}''\cdot\mathbf{r}_{l''}}, \tag{2.12}$$

$$V^-_{\lambda\lambda'\lambda''} = \frac{\sum_{bl'b'l''b''}\sum_{\alpha\beta\gamma}\Phi^{\alpha\beta\gamma}_{0b,l'b',l''b''}\mathbf{e}^{\lambda}_{\alpha b}\mathbf{e}^{-\lambda'}_{\beta b'}\mathbf{e}^{-\lambda''}_{\gamma b''}}{\sqrt{m_b m_{b'} m_{b''}}} \times e^{-i\mathbf{q}'\cdot\mathbf{r}_{l'}}e^{-i\mathbf{q}''\cdot\mathbf{r}_{l''}}. \tag{2.13}$$

$V^+_{\lambda\lambda'\lambda''}$ and $V^-_{\lambda\lambda'\lambda''}$ are the scattering matrix elements for absorption and emission processes, respectively. Since Φ_λ is linear with ∇T, we can write $\Phi_\lambda = -\frac{\hbar\omega_\lambda}{k_B T^2}\mathbf{F}_\lambda \cdot \nabla T$, where $\mathbf{F}_\lambda$ can be regarded as mean free displacement, a generalization of mean free path [58], and ω_λ is the angular frequency. To simplify the linearized phonon BTE

equation (Equation 1.8), we further define $\mathbf{E}_\lambda \equiv \omega_\lambda \mathbf{F}_\lambda$, and can obtain

$$\left\{-\omega_\lambda \mathbf{v}_\lambda + \frac{1}{N}\sum_{\lambda'\lambda''}[(\mathbf{E}_\lambda + \mathbf{E}_{\lambda'} - \mathbf{E}_{\lambda''})\Gamma^+_{\lambda\lambda'\lambda''} + \frac{1}{2}(\mathbf{E}_\lambda - \mathbf{E}_{\lambda'} - \mathbf{E}_{\lambda'})\Gamma^-_{\lambda\lambda'\lambda''}]\right\} \cdot \nabla T = 0. \tag{2.14}$$

Taking $\mathbf{E}_\lambda$ out of the summation term in Equation 2.14, we obtain its iterative form as

$$\mathbf{E}^{i+1}_\lambda = \mathbf{E}^0_\lambda + \frac{\tau^0_\lambda}{N}\sum_{\lambda'\lambda''}[(\mathbf{E}^i_{\lambda''} - \mathbf{E}^i_{\lambda'})\Gamma^+_{\lambda\lambda'\lambda'} + \frac{1}{2}(\mathbf{E}^i_{\lambda''} + \mathbf{E}^i_{\lambda'})\Gamma^-_{\lambda\lambda'\lambda'}], i = 1, 2, 3, ... \tag{2.15}$$

where N is the number of sampled $\mathbf{q}$-points in the reciprocal space. The iterative process starts with

$$\mathbf{E}^0_\lambda = \omega_\lambda \mathbf{v}_\lambda \tau^0_\lambda \tag{2.16}$$

with $\frac{1}{\tau^0_\lambda} = \frac{1}{N}\sum_{\lambda'\lambda''}(\Gamma^+_{\lambda\lambda'\lambda''} + \frac{1}{2}\Gamma^-_{\lambda\lambda'\lambda''})$. Notice it is also possible to include the phonon-isotope scattering the in expression for τ^0_λ using Matthiessen's rule, which is discussed in the Appendix A. In fact, setting $\mathbf{E}_\lambda$ equal to $\mathbf{E}^0_\lambda$ is equivalent to the conventional RTA solution to the linearized phonon BTE (Equation 1.8) [58]. The process is regarded as converged when the difference between the values of $\mathbf{E}_\lambda$ in two consecutive steps is below a convergence threshold. The $\mathbf{E}_\lambda$ should converge for all phonon modes in the iterative process, which is too slow from the computational point of view. Instead, the convergence criterion for κ_L is implemented [58]. When the deviation between the values of κ_L in two consecutive steps falls within the convergence threshold, the iteration scheme is terminated.

The heat current $\mathbf{J}$ generated from the small temperature gradient can be expressed in terms of the distribution function f_λ or $\mathbf{E}_\lambda$ in the linearized BTE (2.14))

[60, 86],

$$\mathbf{J} = \frac{1}{NV}\sum_{\lambda}\hbar\omega_{\lambda}\mathbf{v}_{\lambda}f_{\lambda} = -\frac{1}{k_B T^2 NV}\sum_{\lambda}\hbar^2\omega_{\lambda}f^0_{\lambda}\left(1+f^0_{\lambda}\right)\mathbf{v}_{\lambda}\left(\mathbf{E}_{\lambda}\cdot\nabla T\right) \tag{2.17}$$

where V is the volume of the unit cell, and we have used the fact the heat current is vanishing at the equilibrium state. From Fourier's law $J^{\alpha} = -\sum_{\beta}\kappa^{\alpha\beta}(\nabla T)^{\beta}$, it follows

$$\kappa^{\alpha\beta} = \frac{1}{k_B T^2 NV}\sum_{\lambda}\hbar^2\omega_{\lambda}f^0_{\lambda}(1+f^0_{\lambda})v^0_{\lambda}E^{\beta}_{\lambda}. \tag{2.18}$$

Chapter 3

Carrier Scattering Mechanism in 3C-SiC

We have developed the first principles methods for the calculations of electrical transport properties in Chapter 2, whose accuracy still needs further examination. In this chapter, we used 3C-SiC as an example to validate our methods for obtaining the electrical transport properties such as carrier mobility. Despite there are only two atoms inside the primitive unit cell of 3C-SiC, the two atoms belong to different elements, leading 3C-SiC to be a polar semiconductor, which is ideal to examine the accuracy of the interpolated electron-phonon interaction matrix elements with the polar-longitudinal-optical phonons. Also, the simple crystal structure that 3C-SiC possesses makes the calculations of the electrical transport properties limited by the electron-phonon interaction less expensive. In addition, there are abundant experimental data measured on the single crystal samples available for both n-type and p-type 3C-SiC, which makes it easy to compare our calculated electrical transport properties, such as the carrier mobility, to the available experimental data.

3.1 Introduction

Silicon carbide (SiC) is one of the most promising alternatives to silicon for high-temperature and/or high-power devices because of its unique combination of wide band gap [87, 88],high breakdown voltage [87, 88], and high thermal conductivity [89, 90]. The performance of SiC-based devices has been demonstrated in past decades [91, 92, 93, 94, 95, 96, 97]. From a fundamental research point of view, SiC is interesting in its own right. For example, SiC has numerous allotropes, among which the cubic phase (3C) and hexagonal phases (4H and 6H) are the most interesting. Note that the device applications of SiC rely on its electrical transport properties. Concerning the electrical transport properties, the 4H and 3C phases have been reported to have substantially higher electron mobility than the 6H phase [98]. In particular, 3C-SiC adopts a simple zinc-blende crystal structure, which is isotropic, with several advantages compared to other allotropes with respect to applications.

Despite the abundant data in literature, both experimental [9, 10, 99, 100] and theoretical [101, 102, 103, 104, 105, 106, 107, 108], the electrical transport properties of 3C-SiC have not yet been fully understood at the microscopic level. The experimental electron mobilities vary greatly from sample to sample, intimately related to the quality and growth conditions. For example, Nelson *et al.* [9] reported a room temperature electron mobility of 890 $cm^2/V \cdot s$ in n-type single crystalline 3C-SiC. Shinohara *et al.* [10] obtained a value larger than 750 $cm^2/V \cdot s$ in undoped 3C-SiC epitaxial film grown on carbonized silicon surfaces. Yamanaka *et al.* [99] obtained a much smaller value around 500 $cm^2/V \cdot s$ for incidentally doped n-type 3C-SiC layers epitaxially grown on silicon, and the authors argued that longitudinal acoustic (LA) phonons dominate the scattering mechanism at room temperature and above. On the theory side, a value of 1300 $cm^2/V \cdot s$ at 300 K has been reported which assumes polar

longitudinal optical (LO) phonon scattering being the dominant scattering mechanism [108]. These early studies focused mainly on n-type 3C-SiC, however, the research on p type 3C-SiC is scarce. Thus, there is a knowledge gap regarding p-type 3C-SiC, preventing us from obtaining a coherent and complete picture of the electrical transport properties of 3C-SiC.

As discussed above, electron-phonon interaction is at the core of understanding the electrical transport properties of 3C-SiC at the microscopic level. To this end, first-principles calculations of carrier transport properties are the tools of choice to fill this gap of knowledge. However, first-principles calculations of carrier transport properties are computationally expensive as very dense meshes of Brillouin zone sampling are required for both carriers and phonons. The lately developed interpolation methods for electron-phonon interaction matrix elements [77, 84, 85, 109] greatly reduced the time required for calculating the electron-phonon interaction matrix elements. The efficiency of these methods has been confirmed in both nonpolar materials and polar materials [77, 80, 81, 83, 110, 111, 112]. Therefore, in this paper, we carry out first-principles calculations to have a deeper understanding of the intrinsic electron and hole transport mechanism of single crystalline 3C-SiC. In particular, the Wannier function interpolation method [84, 85, 109, 113] 29313233is employed to obtain the electron-phonon interaction matrix elements, which are then used to calculate phonon-limited scattering rates and carrier mobilities by solving the electron BTE (Equation 2.1).

3.2 Computational Details

Density functional theory (DFT) is employed to calculate the geometric structure and electronic band structure, while density functional perturbation theory is

used to obtain phonon dispersion relation and initial electron-phonon interaction matrix elements as implemented in Quantum Espresso package [114] with norm-conserving pseudopotential under the local density approximation [115]. The planewave cutoff energy is set to be 58 Ry, and $16 \times 16 \times 16$ Monkhorst-Pack $\mathbf{k}$ meshes are used for structure relaxation, both of which are well converged. The lattice structure of 3C-SiC is shown in Figure 3.1(a) with the relaxed lattice constant of 4.326 Å, agreeing well with experimental value 4.360 Å[116]. To interpolate the electron-phonon interaction matrix elements, the EPW package [85] is employed to perform Wannier function interpolation. The initial coarse grids are chosen as $6 \times 6 \times 6$ for both $\mathbf{k}$ and $\mathbf{q}$. The chemical potential is manually chosen to be 0.3 eV in the band gap away from the band edges to ensure that the calculated mobility is intrinsically phonon-limited and corresponds to a low carrier concentration limit, where the defect scattering can be ignored.

3.3 Results and Discussions

It has been reported that the spin orbit coupling (SOC) effect, which leads to the splitting of the degenerate valence band, has a great influence on the hole mobility in different materials [81, 82, 83]. Therefore, in our calculation, SOC is included for the calculation of electronic band structure, phonon dispersion relation, and electron-phonon interaction matrix elements unless otherwise stated. The electronic band structure along high-symmetry paths [Figure 3.1](b) is shown in Figure 3.2(a). 3C-SiC has an indirect band gap, with the valence band maximum (VBM) located at Γ point, and the conduction band minimum (CBM) sitting at X point. The calculated band gap is 1.34 eV, smaller than the experimental value of 2.42 eV [117]. This is a result of DFT usually underestimating the energy of band gaps. However, the band

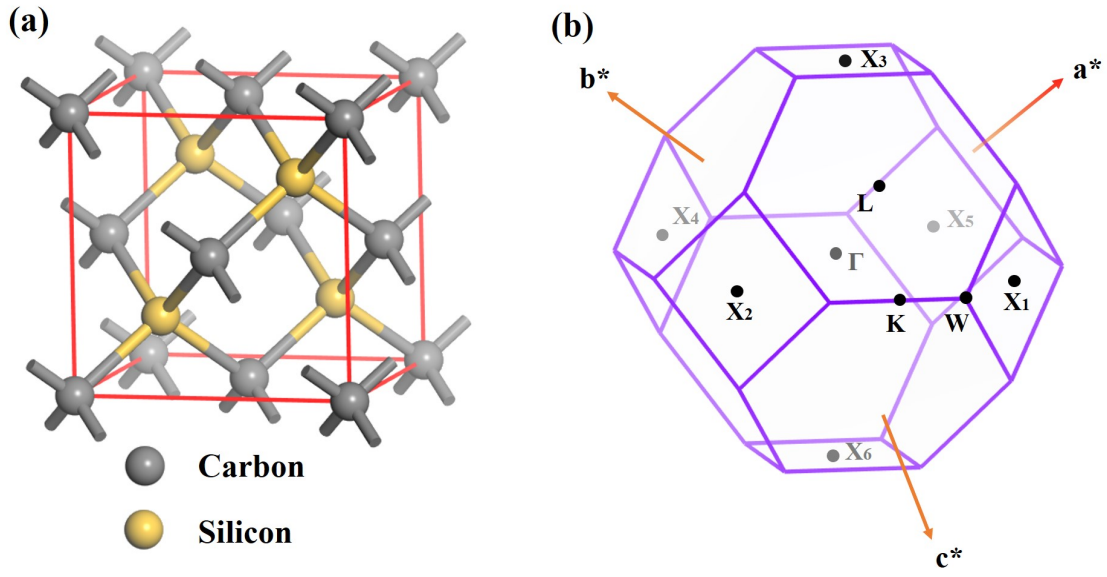

Figure 3.1: (a) Geometric structure of 3C-SiC (conventional unit cell) and (b) first Brillouin zone of 3C-SiC with the high symmetry points labeled. The fractional coordinates for the high symmetry points with respect to reciprocal lattice vectors are: X_1=(0.5, 0, 0.5), X_2=(0, 0.5, 0.5), X_3=(0.5, 0.5, 0), X_4=(-0.5, 0, -0.5), X_5=(0, -0.5, -0.5), X_6=(-0.5, -0.5, 0), K=(0.375, 0.375, 0.75), W=(0.5, 0.25, 0.75) and L=(0.5, 0.5, 0.5).

gap has no effect on the calculated transport properties. With SOC, as can be seen from the inset of Figure 3.2(a), there is a small split-off energy gap about 15 meV in the valence band, close to the experimental value of 10 meV [118]. The calculated phonon dispersion relation along with experimental data are shown in Figure 3.2(b). It is clear that the calculated phonon dispersion relation is in excellent agreement with the experimental values from both inelastic X-ray scattering [7] and Raman measurement [8]. It is worth noting that the highest frequency of the LO phonons is 121 meV, which is larger than those in conventional semiconductors such as silicon [81, 83] and GaAs [80, 81, 110].

The mobility calculation is very time and memory consuming, and it is always necessary to do a convergence test on the k and q grids. As can be seen in Figure 3.3,

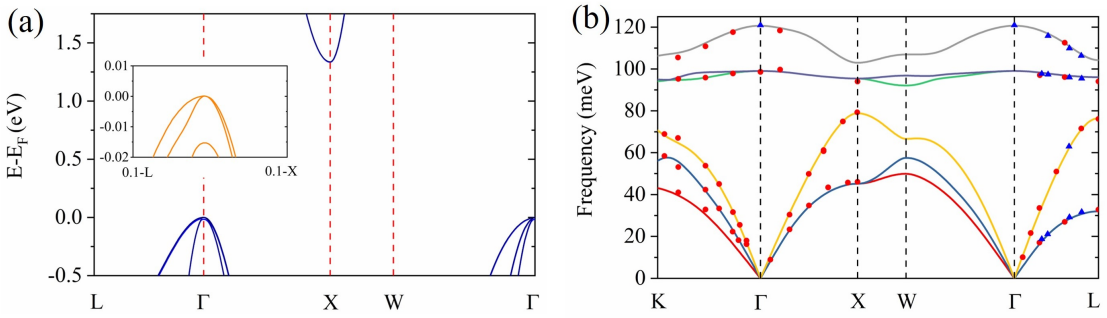

Figure 3.2: (a) Electronic band structure and (b) phonon dispersion relation along high-symmetry points in the first Brillouin zone. Inset: zoom-in of the valence band, where the split-off gap is significantly clearer. Experimental data for phonon dispersion are taken from Ref [7] and Ref [8]. Different branches: transverse acoustic (TA1 and TA2), longitudinal acoustic (LA), transverse optical (TO1 and TO2), and longitudinal optical (LO) are depicted in different colors.

at room temperature, the obtained mobilities of holes and electrons are well converged with the relative difference around 2% when the fine $\mathbf{k}$ and $\mathbf{q}$ meshes are both $120 \times 120 \times 120$.

With the converged $\mathbf{k}$ and $\mathbf{q}$ meshes mentioned above, the calculated carrier mobilities as a function of temperature are depicted in Figure 3.4. For both electrons and holes, the mobilities obtained with exact solution to the BTE (labeled as ITER in Figure 3.4) agree very well with the experimental results in a broad temperature range, from 200 K to 600 K. However, the conventional-RTA method strongly underestimates the mobilities by more than 31% and 17% variance for electrons and holes, respectively.

Mobilities obtained without SOC are also plotted in Figure 3.4 for comparison. Since SOC does not affect the conduction bands in 3C-SiC, the electron mobilities calculated with and without SOC are identical. On the other end, calculation without SOC slightly overestimates the hole mobilities compared to the valued obtained with SOC. For example, at 300 K, the mobilities obtained with and without SOC effect

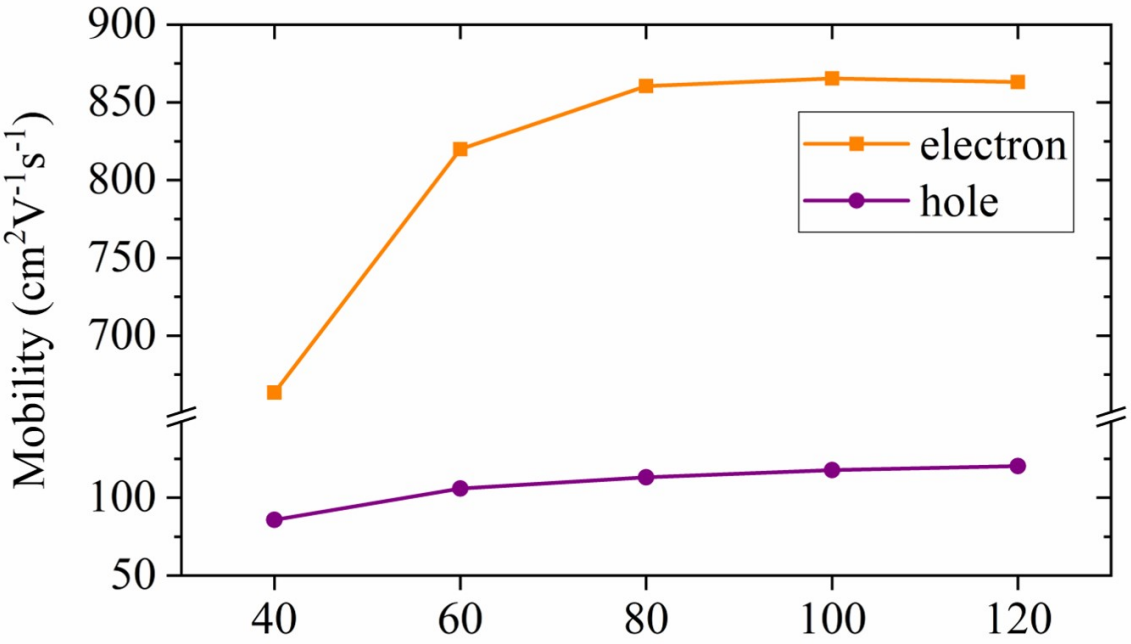

Figure 3.3: Convergence on the carrier mobilities at $300K$ with respect to **k** and **q** grids. Here, in light of the high symmetrical cubic structure of 3C-SiC, the number n on the horizontal axis represents $n \times n \times n$ **k** and **q** fine grids.

are 120.4 and 122.8 $cm^2/V \cdot s$, respectively. As temperature increases from 200 K to 800 K, the variance decreases from 2.0% to 1.0%. The thermal energy increasing with temperature can smear out the split-off gap. Only when the thermal energy is much smaller than the split-off gap, SOC can have appreciable effect on the carrier mobility. The split-off gap of 15 meV corresponds to a temperature of 174 K. Therefore, the SOC effect on the hole mobility in the temperature range (from 200 K to 800 K) studied in this paper is negligible and much smaller than that of silicon [81, 83] and GaAs [81] because of much smaller split-off energy gap of 3C-SiC (15 meV) when compared with silicon (∼44 meV) [81] and GaAs (∼330 meV) [81, 119, 120].

Figure 3.5 shows the scattering rates of electrons and holes decomposed into each phonon mode of 3C-SiC at 300 K. There are two sudden jumps, signifying the onset of emission processes of certain phonon modes. Electrons and holes share a

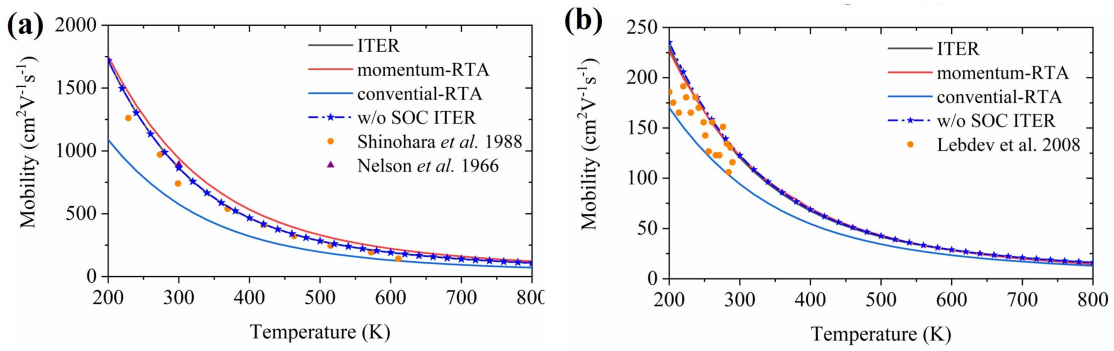

Figure 3.4: Mobilities of electron (a) and hole (b) as a function of temperature. The experimental results for electrons are taken from Ref [9] and Ref [10] and is from Ref [11] for holes. It should be noted that the mobilities obtained by full solution with and without SOC are overlaid on each other in the figure.

common jump at 121 meV, corresponding to the emission processes of the LO phonon at Γ point. For electrons, the other jump is located at 79 meV, related to the LA phonon at X point. For holes, the other sits at 99 meV which is relevant to the TO phonon at Γ point.

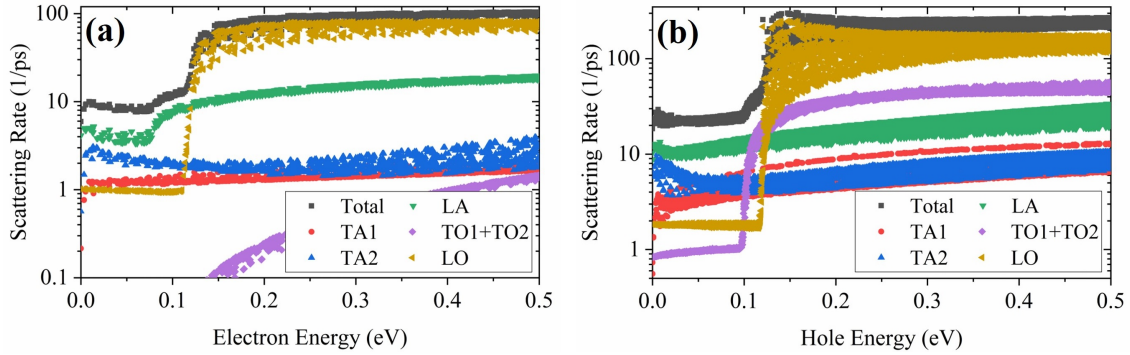

Figure 3.5: Total and decomposed scattering rates of (a) electrons and (b) holes in 3C-SiC at $300K$.

As can be seen, LA phonons dominate the electron-phonon scatterings for electrons with energy less than 121 meV, which actually contribute 97% to its total mobility. In the case of holes, LA phonons still govern the electron phonon interactions with hole energy less than 99 meV, from which 93% of the total mobility is reached.

This indicates that the LA phonon scattering is the governing scattering mechanism in 3C-SiC at 300 K, in consistent with experimental observation [99, 121]. This is, however, in contrast to other polar materials, such as GaAs [80, 81], PbTe [122], SnSe [111], and SnTe [112], in which polar LO phonons dominate the scattering for a wide energy range including band edges. Actually, LO-phonon scattering increases suddenly by two orders of magnitude at 121 meV due to the occurrence of phonon emission processes. As a result, LO phonons dominate the scattering above 121 meV. To understand the orders-of-magnitude smaller scattering below 121 meV for the LO-phonon absorption processes, we refer to Equations 2.3 and 2.4. Since the electron/hole occupation number can be neglected in the intrinsic limit, the scattering rates from phonon absorption and emission processes are proportional to $N_{\mathbf{q}}p^0$ and $1+N^0_{-\mathbf{q}p}$, respectively, which is due to the Boson nature of phonons. The LO phonon corresponds to an energy of 121 meV, which is much larger than the thermal energy at 300 K. Therefore, the LO phonon is almost unexcited at room temperature, and $(1+N^0_{\Gamma,LO})/N^0_{\Gamma,LO}$ is 105. This also indicates that the large LO phonon frequency typically suggests small scattering. It should be noted that the authors of a very recent paper [82] also mentioned that the frequency of LO phonons are also very high in boron-based semiconductors, leading to the suppression of the contribution of LO phonons to the total scattering rates.

Transverse optical (TO) phonon scatterings for holes are larger than those for electrons by more than one order of magnitude. As a result, the signature of the corresponding phonon emission processes is evident in the total scattering rates for holes but not for electrons. To understand this, we plot the electron-phonon interaction matrix elements $|g|$ of electrons and holes at band extrema with each phonon branch along high-symmetry paths in Figure 3.6(a) and 3.6(b), respectively. Clearly, the electron-phonon interaction matrix element $|g|$ with TO modes at Γ point

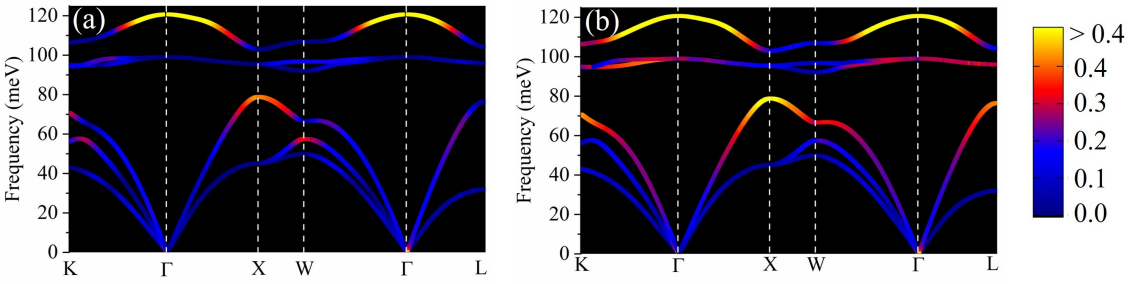

Figure 3.6: Calculated electron-phonon interaction matrix elements $|g^{m\mathbf{k}+\mathbf{q}}_{n\mathbf{k},\mathbf{q}p}|$ (in unit of eV) of (a) initial CBM and (b) initial VBM electron with different phonon branches along high-symmetry directions in the first Brillouin zone.

for holes is much larger than that for electrons. $|g|$ is actually very sensitive to the nature of electronic orbitals. For instance, $|g|$ is found to be weak for interaction between acoustic phonons and nonbonding orbitals [123]. We also note that $|g|$ with LO modes at Γ point for electrons and holes are comparable.

Since the VBM occurs at Γ point, there is no intervalley scattering for holes. However, the CBM is at the X point, and then intervalley scattering with phonon at X point is allowed for electrons. Due to symmetry, there are six equivalent X points, as shown in Figure 3.1(b). X_1, X_2, and X_3 are identical to X_4, X_5, and X_6, respectively, up to a certain reciprocal lattice vector. Two nonidentical X points can be connected with a vector going from the origin to another X point. For example, $X_2 - X_1 = X_3$. The intervalley scattering processes are facilitated by the large $|g|$ with LA modes at X point. In Figure 3.7, we quantify the individual contribution from intravalley and intervalley scatterings to the total LA scattering rates for electrons. The intravalley scattering actually dominates up to 79 meV, whereas the intervalley scattering governs above 79 meV. As aforementioned, the sudden jump of the intervalley scattering rates at 79 meV corresponds to the onset of the emission processes of the LA phonon at the X point. Those electrons below 79 meV contribute 82% to the total mobility.

Therefore, the mobilities are dominated by the intravalley LA phonon scattering for both electrons and holes at room temperature.

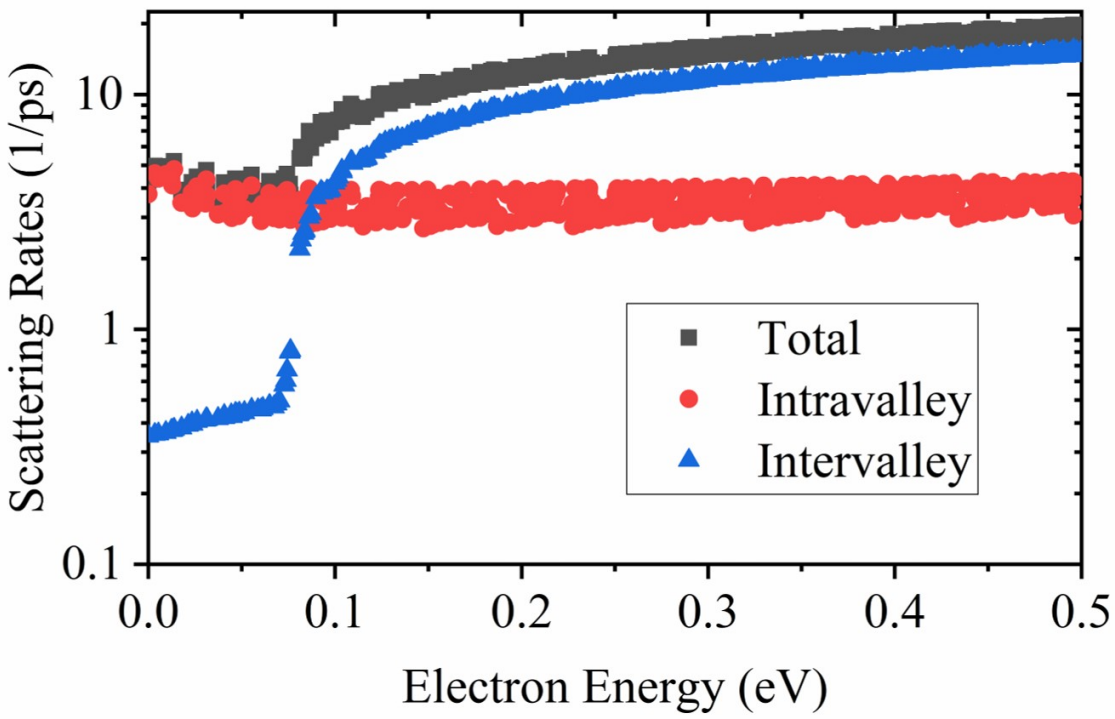

Figure 3.7: Contribution of intravalley and intervalley scattering to LA scattering rates for electrons at room temperature.

Figure 3.8 shows the total scattering rates and the contributions from LA and LO phonons for both electrons and holes at different temperatures. The phonon occupation number and, consequently, the scattering rates, increase with temperature. Notably, the relative increase $\frac{n^{T_2}(E)}{n^{T_1}(E)}$ in the occupation number of LO phonons is larger than that of LA phonons with increasing temperature. As a result, the LO scattering becomes comparable to the LA scattering near the band edges at 600 K and turns out to be completely dominant at 800K. This contrasts with the argument made in Ref. [99], in which the authors claimed that both electron and hole mobilities are limited by the acoustic phonon scattering above room temperature.

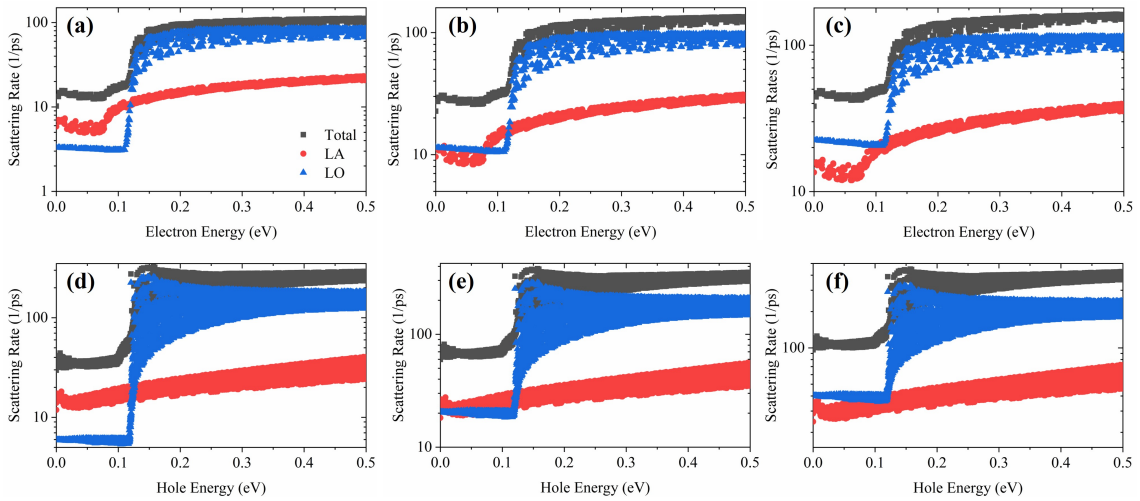

Figure 3.8: Total scattering rates and contributions from LA and LO phonons for electrons at (a) $400K$, (b) $600K$ and (c) $800K$; for holes at (d) $400K$, (e) $600K$ and (f) $800K$

The mode-specific analysis of mean free paths (MFPs) are shown in Figure 3.9. At room temperature, the largest MFPs of electrons and holes are about 40 nm and 15 nm, respectively. The largest MFPs of both carriers are found be of the energy range from 0.07 eV to 0.1 eV. In this energy range, the electrons contribute about 75%-94% to its total mobility, while holes contribute 71%-93% to the total mobility.

3.4 Summary

In summary, we performed entire first principles calculations of the mobilities for both n- and p-type 3C-SiC using Boltzmann transport equation (BTE) based on polar Wannier function interpolation of electron-phonon interaction matrix elements. The calculated electron and hole mobilities are reasonably consistent with the experimental data. We found a temperature dependent scattering mechanism in 3C-SiC. At room temperature, owing to unexcited longitudinal optical (LO) modes, the longitudinal acoustic (LA) phonons dominate the scatterings of electrons and holes

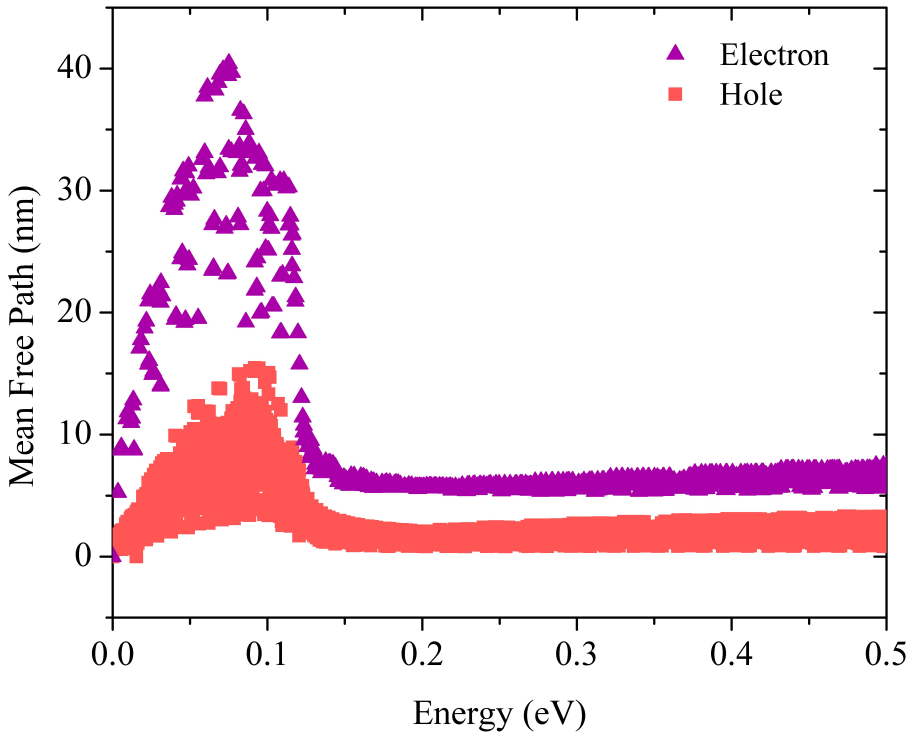

Figure 3.9: Mean free path of (a) electrons and (b) holes in 3C-SiC at $300K$.

contributing to the mobilities. Specifically, the intravalley LA phonons dominate the scatterings of electrons up to 79 meV, and the intervalley scattering becomes dominant between 79 and 121 meV. The intervalley scattering is not present for holes. At $800K$, LO-phonon interaction becomes the governing scattering mechanism for both electrons and holes. The spin-orbit coupling almost has no influence on the calculated mobilities, especially for the electrons. The largest carrier mean free path is about 40 nm for the electrons and 15 nm for the holes in 3C-SiC at room temperature.

Chapter 4

Anisotropic Thermoelectric Performance of Magnesium Antimonide

Till now, we have proved in Chapter 3 that our developed methods can successfully reproduce the experimental measured carrier mobility for 3C-SiC without any human-adjustable parameters. Combining with the phonon BTE, it is now possible to calculate the thermoelectric transport properties of thermoelectric materials. In this chapter, we choose Mg_3Sb_2, which is rising star for moderate temperature thermoelectric application. Another important reason for choosing Mg_3Sb_2 is that its trigonal structure implies possible anisotropic thermoelectric transport properties, which is hard to explore from the experimental point of view.

4.1 Introduction

Towards high zT, high crystal lattice symmetry is favored because high band degeneracy and multiple pockets at the Fermi surface tend to yield high power factor (PF). [6, 124] In this vein, many state-of-the-art thermoelectric materials adopt cubic structure: PbTe ($Fm\bar{3}m$, space group *No.* 225) [6, 125], SnTe ($Fm\bar{3}m$, space group *No.* 225) [126, 127, 128], Mg_2Si ($Fm\bar{3}m$, space group *No.* 225) [129, 130], $CoSb_3$ ($Im\bar{3}$, space group *No.* 204) [131, 132], half-Heusler alloys ($F\bar{4}3m$, space group *No.* 216) [133, 134, 135], and Si-Ge alloys ($F\bar{4}3m$, space group *No.* 216) [136]. On the other hand, some renowned thermoelectric materials possess lower crystal lattice symmetry: Bi_2Te_3 ($R\bar{3}m$, space group *No.* 166) [137, 138, 139], GeTe ($R\bar{3}m$, space group *No.* 166) [140], and SnSe (Pnma, space group *No.* 62) [52, 141, 142] and owe their state-of-the-art thermoelectric performance largely to their intrinsically low thermal conductivities. In the context of the classic phonon-glass and electron-crystal paradigm [143, 144, 145], the cubic structured thermoelectric materials are in line of electron-crystal, whereas lower lattice symmetry-structured materials emphasize the aspect of phonon-glass to make good thermoelectrics.

Among low lattice symmetry thermoelectric materials, Zintl phase compounds with a general formula AB_2X_2 and a space group $P\bar{3}m1$ (space group *No.* 162) constitute a notable family, in which A is the cation and BX together is the anion. Most AB_2X_2 Zintl compounds are p-type semiconductors because of cationic vacancies [146]. In light of the large phase space of AB_2X_2 to tune the electrical and thermal transport properties, the ground-breaking discovery of Te-doped n-type Mg_3Sb_2 with zT around 1.6 at 720 K has made Mg_3Sb_2-based compounds an active frontier of current thermoelectric materials research [19]. The highest reported zT of n-type Mg_3Sb_2 (Mn and Te co-doped $Mg_3Sb_{1.5}Bi_{0.5}$) is 1.85 at 723 K [147]. Meanwhile, n-

type Mg_3Bi_2 with similar geometric structure as Mg_3Sb_2 is known to possess a peak zT of around 0.9 at 350 K [148]. To date, the major challenge is the performance imbalance between n-type and p-type Mg_3Sb_2. From a thermoelectric device perspective, it is desired to fabricate a device using n-type and p-type polycrystalline legs made from the same parent compound and with comparable thermoelectric performance. However, despite great efforts, the present highest zT of p-type Mg_3Sb_2-based compounds is only about half of its n-type counterparts. The imposing need to develop higher performance p-type Mg_3Sb_2-based compounds is the motivation of the present work.

Toward higher performance p-type Mg_3Sb_2-based compounds, theoretical efforts *via* orbital engineering [149] and experimental efforts via optimizing hole concentration as mentioned in Chapter 1 [15, 23, 150] have been exerted. Given the relatively lower lattice symmetry (trigonal lattice), anisotropic electrical and thermal transport properties including zT of Mg_3Sb_2-based compounds are expected. Crystal structural anisotropy is not rare among thermoelectric materials, unnecessarily a disadvantage in performance optimization. For instance, the out-of-plane electrical resistivity of n-type is found to be three times higher than that of in-plane direction with a wide temperature range [151]; for p-type SnSe, the in-plane zT is much higher than that of out-of-plane direction [52, 141, 142]. However, experimentally exploring the anisotropic transport properties of a structurally anisotropic thermoelectric material is demanding; the characterization of single crystalline samples calls for large, high-quality single crystal samples and transport measurements (*aka* the electrical conductivity, Seebeck coefficient, and thermal conductivity) along major crystallographic axes; concerning the characterization of polycrystalline samples, especially those prepared under uniaxial pressure, one must ensure all thermoelectric properties are measured along the same direction to avoid the artifacts caused by the texture.

To date, there are only a few reports of the transport properties of single crystalline Mg_3Sb_2. The single crystals grown by Kim *et al.* were easily cleavable, and the electrical resistivity measurements were performed in the ab-plane (hereafter called in-plane) direction [12]. Another work on single crystalline $Mg_3Sb_{2-x}Bi_x$ by the same group reported large anisotropy in the electrical resistivity, with the resistivity in the out-of-plane (c-axis) direction orders of magnitude larger than the that along the in-plane direction [13]. Xin *et al.* has found that for pristine Mg_3Sb_2, the in-plane resistivity is two times larger than that of out-of-plane direction at 300 K [14]. Owing to the highly demanding requirements on the sample dimensions, the anisotropy of thermal conductivity and Seebeck coefficient has not been reported experimentally. To clarify the intrinsic thermoelectric properties, and thus the thermoelectric potential of Mg_3Sb_2, it is highly desired to experimentally grow large, high quality-single crystals and/or theoretically calculate the thermoelectric properties of pristine Mg_3Sb_2.

As mentioned in Chapter 2, first principles calculations employing semiclassical transport equations (*e.g.* Boltzmann transport equations for charge carriers and phonons) offer a great opportunity to fill out the knowledge gap of many anisotropic thermoelectric materials that are hard to experimentally explore, including Mg_3Sb_2. To this end, *ab initio* calculations of lattice thermal conductivity based on the three-phonon process have matured nowadays [58, 152]. Several groups reported the nearly isotropic lattice thermal conductivity of Mg_3Sb_2 along in-plane and out-of-plane directions [17, 18]. Meanwhile, as the electrical transport properties are governed by the electronic band structure and the specific carrier scattering mechanism, it is crucial to deal with the scattering properly in the calculations. Previous calculations of electrical transport properties on Mg_3Sb_2 employed constant relaxation time approximation (CRTA) [19, 146, 149, 153], in which relaxation time is an adjustable

single-value parameter. Apparently, it is hard for CRTA to capture the detailed scattering mechanism of charge carriers. Given the complexity of both the structural and electronic structure of Mg_3Sb_2, CRTA is oversimplified. On the other hand, it is customarily accepted that electron-phonon interactions become the dominant scattering mechanism at elevated temperatures. In Mg_3Sb_2, despite small contributions from alloy scattering, the electron-acoustic phonon interactions dominate above 500 K [19, 20]. Pristine Mg_3Sb_2 is a semiconductor with a band gap around 0.4-0.6 eV [17, 19, 154, 155] and a Debye temperature below 230 K [156]. Per the 10 k_BT_0 rule [157], the optimal working temperature for Mg_3Sb_2 should be around 700-800 K. At temperatures well above the Debye temperature, electron-phonon interaction is the dominant scattering mechanism of charge carriers, making the results of theoretical calculations based on electron-phonon interaction more reliable to be compared with the experimental data.

Here, we use the state-of-the-art ab initio method to calculate the electron-phonon interaction limited electrical transport properties *via* exact solutions of the Boltzmann transport equation. When calculating the electron-phonon interaction matrix elements, the contributions from all phonon branches (*aka* all modes in the first Brillouin zone) are taken into account. It is of great interest to note the zT of p-type Mg_3Sb_2 along its c-axis attained in this work is almost three times larger than that along the a(b)-axis, with a zT around 1.5 at 750 K along the c-direction. In n-type Mg_3Sb_2, both the electrical and thermal transport properties tend to be isotropic, and our calculated zT value agrees well with experimental data of n-type Mg_3Sb_2.

4.2 Computational Details

First principles calculations based on density functional theory (DFT) are carried out to calculate electronic band structure with a 10×10×6 Monkhorst-Pack **k** grid and cut-off energy of 50 Ry. Norm conserving fully relativistic pseudo-potentials with local density approximation (LDA) [115] are employed. The phonon dispersion relation is calculated using density functional perturbation theory (DFPT) with a 5×5×3 **q** grid mesh. All these calculations are performed using Quantum Espresso software package [114]. The relaxed geometrical structure of Mg_3Sb_2 is shown in Figure 4.1(a). The calculated lattice constants are a=4.492 Å and c=7.097 Å, which agree well with values measured experimentally (a=4.569 Å and c=7.245 Å) for Mg_3Sb_2 single crystal [14]. The calculated phonon dispersion relation of Mg_3Sb_2 [Figure 4.1(d)] agrees well with previous works [17, 18, 158, 159], especially for the low-frequency phonon modes. In addition, our calculated Born effective charges are 3.10, 1.77 and -3.32 for Mg1, Mg2 and Sb atoms are also in consistent with Ref[17, 18, 158, 159].

As aforementioned, the electrical transport properties in this work are based on electron-phonon interaction. The correctness of electronic band structure is of great importance. The calculated band gap of Mg_3Sb_2 using LDA is 0.051 eV as shown in Figure 4.1(c). However, the band gaps obtained using Heyd-Scuseria-Ernzerhof (HSE06) [160, 161, 162] and TB-mBJ potential [163] are 0.45 [17] and 0.6 eV [19], respectively. Although these two methods could provide more accurate values of band gap comparable to experimental measured values [154, 155], the band curvatures are basically the same compared with LDA or PBE, and only the energy eigenvalues are shifted [17]. The multivalley character of the conduction band is clear in our calculated band structure [cf. Figure 4.1(c)]. The conduction band minimum (labeled as CBM1) is located at point (0.0, 0.417,0.333) inside the first Brillouin zone as

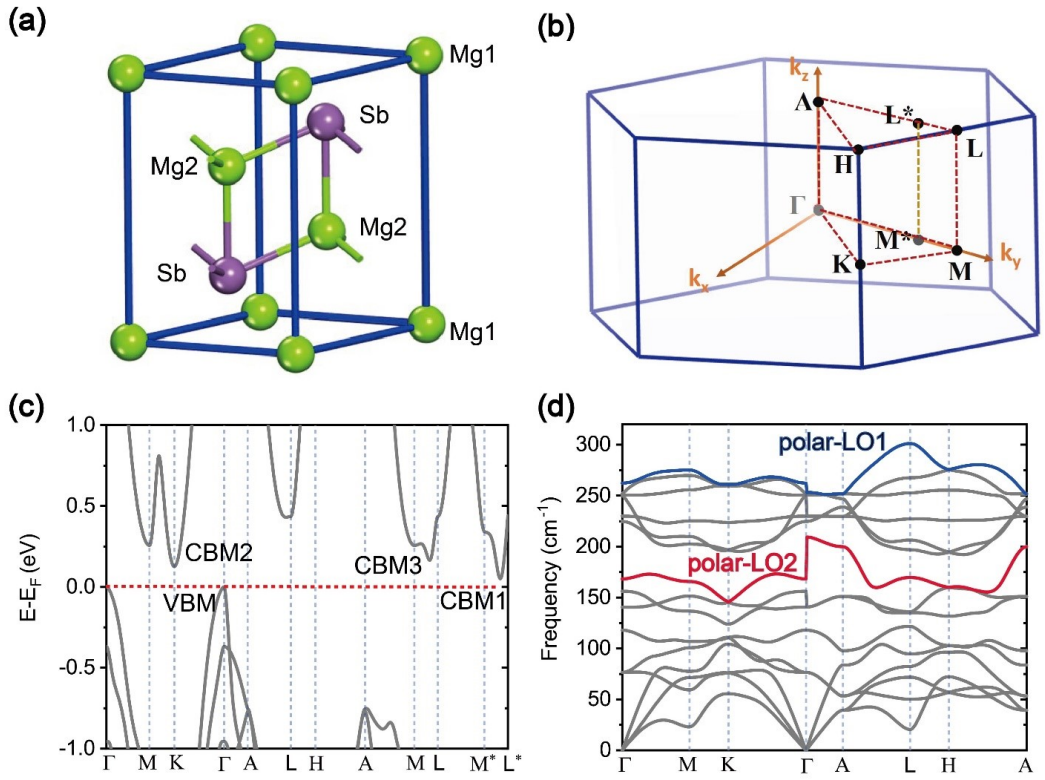

Figure 4.1: (a) Geometric structure of Mg_3Sb_2. (b) First Brillouin zone and high symmetry points. (c) Electronic band structure and (d) phonon dispersion relation along high-symmetry directions in the first Brillouin zone.

pointed out in Zhang *et al.* [20] There are other two conduction band valleys: one is at the K-point (labeled as CBM2) with an energy 0.067 eV above CBM1; the other (CBM3) sits along the M-L direction, and its energy is 0.039 eV higher than CBM2. The locations of these valleys and the energy difference among them are consistent with previously reported values [20]. A single valley in the valence band is observed at the point.

To calculate electron-phonon interaction limited electronic transport properties (aka electrical conductivity, Seebeck coefficient, and electrical thermal conductivity), Wannier function interpolation of electron-phonon coupling matrix is employed

as implemented in EPW package [85]. Both **k** (for electrons and holes) and **q** grids (for phonons) are interpolated to 75×75×50 in Mg_3Sb_2. The electronic transport properties are calculated with the methodology developed in Chapter 2, where the δ functions involved are treated as Gaussian functions with physically adaptive broadening parameters, making the calculation completely parameter free. To calculate, the third-order anharmonic interatomic force constants are obtained using a 4×4×4 supercell with a force cutoff distance of 0.55 nm employed [58, 65]. The ShengBTE package [58, 164] is used for solving the phonon BTE with 26×26×16 **q** sampling.

Owing to the relatively large atomic mass of Sb, spin-orbit coupling (SOC) needs to be considered when calculating the band structure. It is observed in Mg_3Sb_2 that SOC effect has a great influence on the valence band, whereas its effect on the conduction band is negligible as demonstrated in Chapter 3, which is consistent with previous calculations [20]. Hence, SOC is included when calculating the electron-phonon interaction matrix elements for valence band while excluded for conduction band. Because electrons and holes are treated separately in this work, the band gap has no influence on the calculated transport properties as indicated in Chapter 3 [165]. Given the band gap value of 0.45-0.6 eV [154, 155], the bipolar effect is less severe than the case of other narrow band gap materials, *e.g.* Bi_2Te_3 [166] and not taken into account in our calculations. As pointed out in the literature [20, 153] that alloying does not substantially affect the electronic band structure of Mg_3Sb_2, herein our calculations are conducted on the pristine Mg_3Sb_2.

4.3 Results and Discussions

The lattice thermal conductivity of materials depends largely on their bonding properties (*e.g.* bond type, bond strength, and so on). The interlayer and in-

tralayer interactions in chemical bonding networks can be characterized by the ratio of $\rho_{inter}/\rho_{intra}$, where ρ_{inter} and ρ_{intra} denote the electron density values at the bond critical points of the interlayer and intralayer bonds, respectively [18]. In Mg_3Sb_2, the value of $\rho_{inter}/\rho_{intra}$ is close to unity [18], attesting similar interlayer and intralayer interactions and thus nearly isotropic lattice thermal conductivity. Given a trigonal crystal lattice such as Mg_3Sb_2, the physical properties, like effective mass and lattice thermal conductivity in the ab-plane, should be isotropic because of symmetry. In our calculations, it is found the lattice thermal conductivities are identical along a- and b-axis. The lattice thermal conductivity along c axis is slightly larger than that along a(b)-axis with the largest anisotropy (κ_L^c/κ_L^a) around 1.05, agreeing with the analyses based on interlayer and intralayer interactions and Huang *et al.* and Tamaki *et al.* [17, 21]. Hereafter, the degree of anisotropy is defined as the relevant physical quantity along the c-axis divided by the counterpart along a(b)-axis.

In general, the temperature dependency of lattice thermal conductivity attained in this work is in reasonable agreement with previous experimental efforts. It is expected that the calculated lattice thermal conductivity [Figure 4.2(a)] is slightly larger than the experimental results because our calculations do not take into account other phonon scattering mechanisms such as point-defects and grain boundary scattering. Meanwhile, the calculated values obtained via similar methods by other groups are smaller than experimental data [17, 18]. The discrepancy is likely because of different functionals employed in computing the interatomic force constants. Thus, LDA outperforms PBE in obtaining the lattice thermal conductivity for Mg_3Sb_2.

The anisotropy of the electrical conductivity is because of the difference of the carrier velocity squared along different directions. Considering the carrier velocity squared is inversely proportional to the effective mass, the effective mass difference along different crystallographic axes could reflect the anisotropy of electrical conduc-

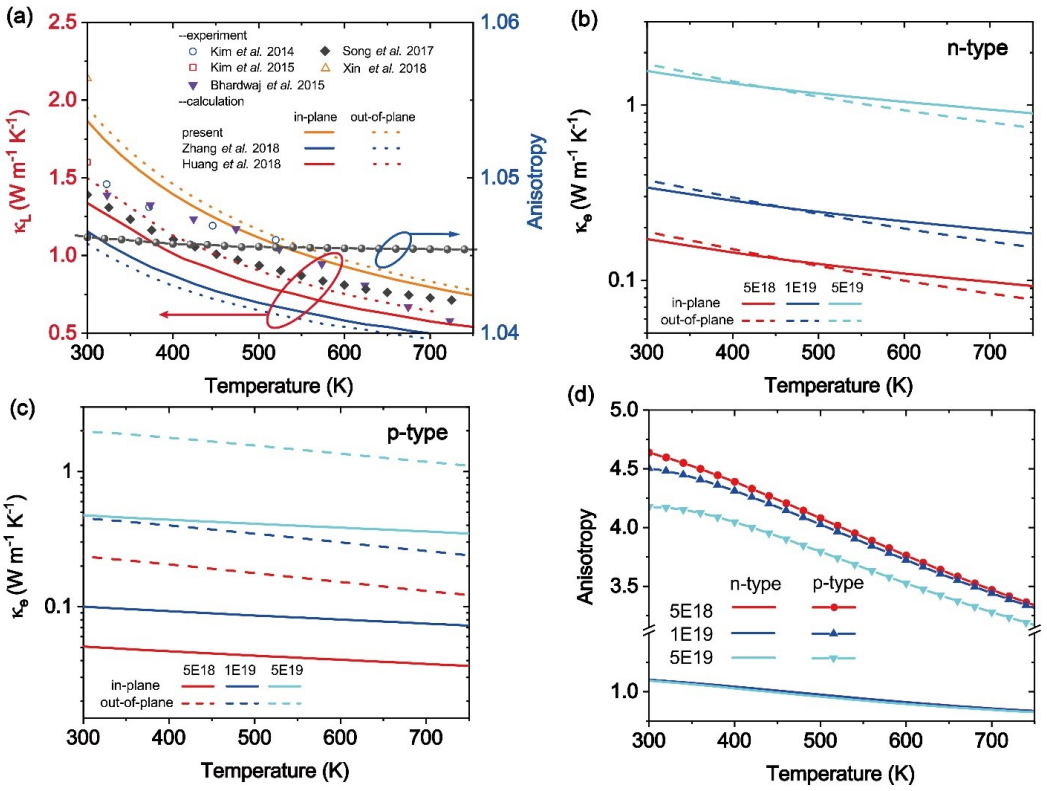

Figure 4.2: Temperature dependent lattice thermal conductivity along with anisotropy (κ_L^c/κ_L^a). (b) Temperature dependent (b) n-type and (c) p-type electrical thermal conductivity. (d) Temperature dependent anisotropy (κ_e^c/κ_e^a) of electrical thermal conductivity in both types. The experimental lattice thermal conductivity data are taken from Ref[12, 13, 14] and Ref[15, 16] for single crystal and p-type polycrystalline samples, respectively. The calculated lattice thermal conductivity data are taken from Ref[17, 18].

tivity and electrical thermal conductivity [111]. According to our calculations, the effective masses at CBM1 are $m^*_{k_x} = 0.15m_0$, $m^*_{k_y} = 0.49m_0$ and $m^*_{k_z} = 0.16m_0$, in accordance with existing data [17, 20, 153]. However, as aforementioned, because of the symmetry, the physical properties in the ab-plane should be isotropic. At CBM1, it is obvious that $m^*_{k_x}$ differs greatly from $m^*_{k_y}$. To understand the strong anisotropy in effective mass along k_x- and k_y-axis, we carefully examined the isoenergy surface with the energy 0.05 eV above CBM1 [Figure 4.3(a)]. Because the CBM1 is located

inside the first Brillouin zone, there are six equivalent electron valleys originating from the symmetry of Mg_3Sb_2 ($P\bar{3}m1$). Therefore, the effective mass in the ab-plane should be averaged over the six valleys. After averaging, the effective masses along the principal axes in the reciprocal space are exactly identical as can be seen from Figure 4.3(b). The value of the averaged effective mass along the k_x (k_y) direction is 0.22 m_0. The small deviation of effective mass along the in-plane and out-of-plane direction implies that both electrical conductivity and electrical thermal conductivity in n-type Mg_3Sb_2 might be less anisotropic.

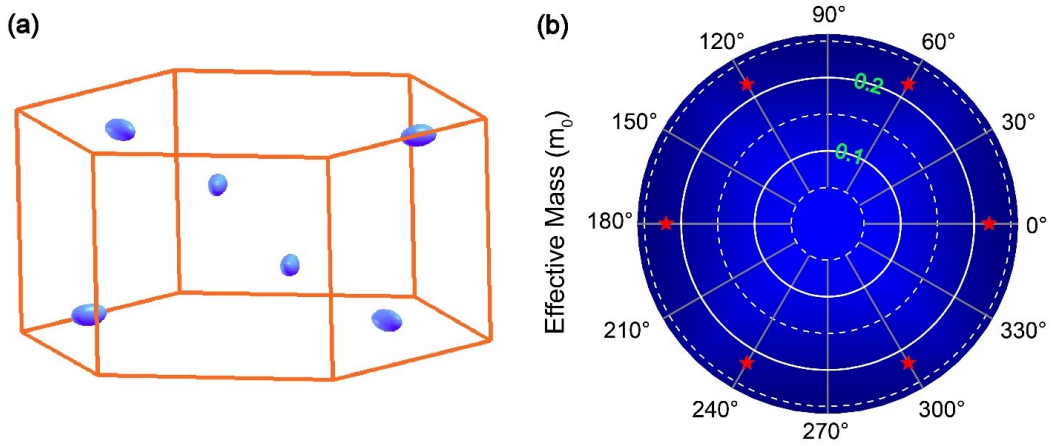

Figure 4.3: (a) Isoenergy surface of Mg_3Sb_2 with energy 0.05 eV above CBM1. (b) Electron effective mass in the ab-plane according to spatial directions, where 0° and 60° correspond to the k_x- and k_y-axis in the reciprocal space, respectively.

The effective masses at Γ for the valence band maximum (VBM) are $m^*_{k_x} = m^*_{k_y} = 0.61m_0$ and $m^*_{k_z} = 0.07m_0$, in reasonable agreement with previously reported values [17]. The small effective mass along the c-axis in p-type Mg_3Sb_2 is an outcome of the small distance between layers leading to strong interlayer interactions, unlike Bi_2Te_3 in which the interlayer interactions is mainly the van der Waals interactions. It is obvious that the effective masses of holes are strongly anisotropic, suggesting the anisotropy of electrical transport properties. Meanwhile, it is generally accepted

for a layered structure that electrical conductivity along the in-plane direction should outperform that along the out-of-plane direction. For example, in n-type Bi_2Te_3, the in-plane electrical conductivity is three times greater than in the out-of-plane direction [151]. Considering the effective mass of VBM along the k_z direction (corresponding to the crystallographic c-axis) is almost one order of magnitude smaller than that in the ab-plane, electrical conductivity and electrical thermal conductivity are expected to be superior along the out-of-plane direction than those along in-plane direction in p-type Mg_3Sb_2.

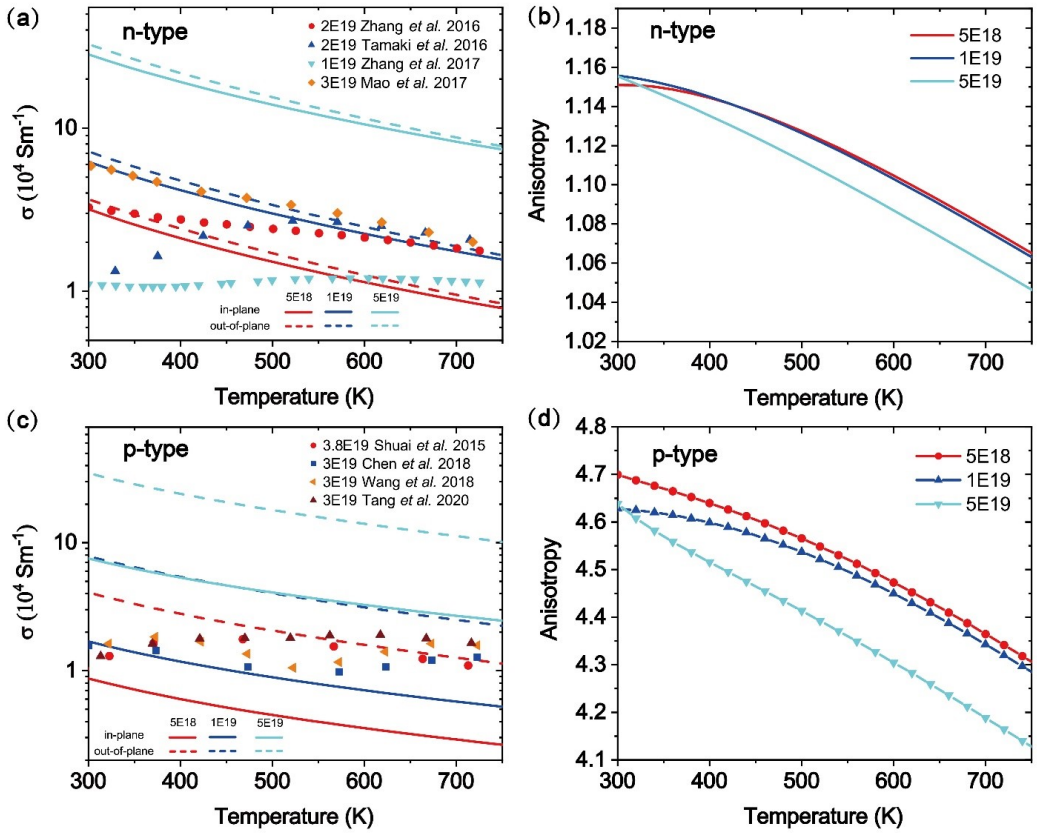

Figure 4.4: Temperature dependent (a) n-type and (c) p-type electrical conductivity. Corresponding temperature dependent anisotropy (σ^c/σ^a) for (b) n-type and (d) p-type Mg_3Sb_2. The experimental data for n- and p-type are taken from Refs[19, 20, 21, 22] and Refs[23, 24, 25, 26], respectively.

According to our calculations, the electrical conductivity [Figure 4.4(c)] and

electrical thermal conductivity [Figure 4.2(c)] of p-type Mg_3Sb_2 along the c-axis are indeed much larger than that in the ab-plane. At room temperature, the ratio of anisotropy in both electrical conductivity and electrical thermal conductivity are close in value; the largest ratio of anisotropy is around 4.6 [cf. Figures 4.2(d) and 4.4(d)]. The anisotropy value attained for p-type electrical conductivity at room temperature is slightly larger than the experimental value reported by Xin *et al.* [14]. For the n-type counterpart, both the attained electrical conductivity and electrical thermal conductivity are nearly isotropic with the highest anisotropy around 1.15 at room temperature [cf. Figures 4.2(d) and 4.4(b)], which is consistent with our analyses based on effective mass.

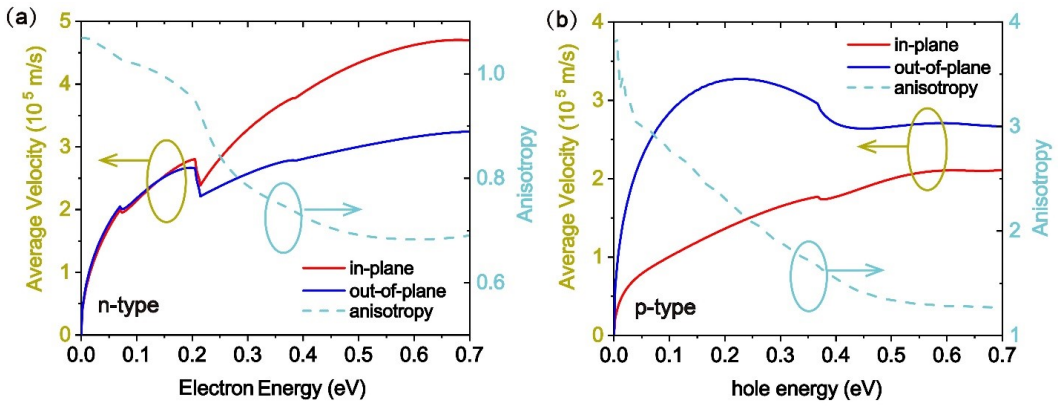

Figure 4.5: Average carrier velocity and corresponding anisotropy (v^c/v^a) for (a) n-type and (b) p-type Mg_3Sb_2.

To analyze the anisotropy quantitatively, we calculate the average carrier velocity along different directions, which is obtained as:

$$\bar{v}^{\alpha}(\varepsilon) = \sqrt{\sum_{n\mathbf{k}} \left|v^{\alpha}_{n\mathbf{k}}\right|^2 \delta\left(\varepsilon - \varepsilon_{n\mathbf{k}}\right) / \sum_{n\mathbf{k}} \delta\left(\varepsilon - \varepsilon_{n\mathbf{k}}\right)}, \tag{4.1}$$

where $\varepsilon_{n\mathbf{k}}$ is the carrier energy at the $n\mathbf{k}$ state. It is clear from Figure 4.5(b) that the average velocity along the c-direction is much larger than in the a(b)-direction

in p-type Mg_3Sb_2. The presence of a kink at around 0.35 eV indicates the second valence band starts to contribute to electrical transport. The contribution from the second valence band can also be seen from the hole scattering rates [Figure 4.6]. As can be seen from the band structure [Figure 4.1(c)], the effective mass along the ab-plane of the second valence band does not vary much compared with VBM, whereas it is larger in the c-direction, leading to a smaller v_c/v_a at energies larger than 0.35 eV. For n-type [Figure 4.5(a)], when the electron energy is below 0.2 eV, the average velocities along a(b)- and c-axis are nearly identical, with an almost-flat anisotropy within this energy range. Multiband conduction behavior is obvious for n-type Mg_3Sb_2 from Figure 4.5(a) with more kinks as compared with p-type Mg_3Sb_2, which are mainly because of the participation from sub-bands. Careful inspection of the mode-specific scattering rates as a function of carrier energy (Figure 4.6) revealed that for both conduction types, carriers with low energy are scattered dominantly by the two polar-LO-phonons [as demonstrated in Figure 4.1(d)], owing to the large electron-phonon coupling constant of these two phonon branches because of the electron-phonon interaction matrix elements of these two branches diverge as $1/|\mathbf{q}|$ for $|\mathbf{q}|$ approaching zero [167]. As the energy of carriers increases, other phonon modes start to contribute significantly to the total scattering.

Note that the carrier scattering by polar-LO phonons is sensitive to the dielectric constant. The calculated dielectric constants are 13.5 and 16.2 along a(b)-axis and c-axis, in good agreement with the literature data 13.8 and 16.4 along a(b)-axis and c-axis, respectively [27]. In general, high carrier concentration tends to weaken the screening effect, yielding longer carrier lifetime and higher carrier mobility [122]. In this work, the screening effect is not taken into account. Nonetheless, high carrier concentration enhances electron-electron and electron-defect scattering, which decrease the carrier mobility and somewhat compensate for the effect of the weakened

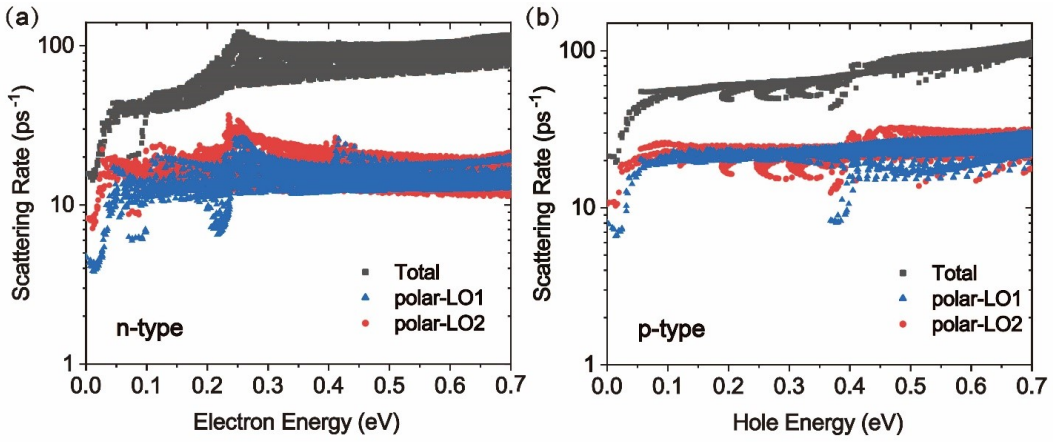

Figure 4.6: Room temperature scattering rates as a function of carrier energy for (a) n-type and (b) p-type Mg_3Sb_2 with carrier concentration at 5×10^{18} cm^{-3}.

screening effect [168].

It is generally accepted that the anisotropy of the Seebeck coefficient is weaker than that of the electrical conductivity in an anisotropic thermoelectric material. SnSe, as an example, regardless of the ratio in zT along a- and c-axis is around three at 700 K; the corresponding ratio for Seebeck coefficient is merely around one [141]. In this work, it is apparent from Figure 4.7(b) and (d) that the Seebeck coefficients are also nearly isotropic with the anisotropy (α^c/α^a) between 0.9 and 1 within a wide temperature and carrier concentration range. In physics, the pair superscripts for a physical quantity can be regarded as the action-reaction relation. Taking $\sigma^{\beta\gamma}$ as an example, the action is along the γ direction, while the reaction is along the β direction. The ξ term of Equation 2.7 is the entropy flow. According to Equation 2.7 for Seebeck coefficient, the direction of reaction for the entropy flow (ξ) is the action direction of the σ^{-1} term. In other work, the Seebeck coefficient can be viewed as the average entropy flow weighted by the σ^{-1} terms along the three principal axes. Therefore, the Seebeck coefficient should be less anisotropic than the electrical conductivity.

The near isotropy of Seebeck coefficient may be further understood from the

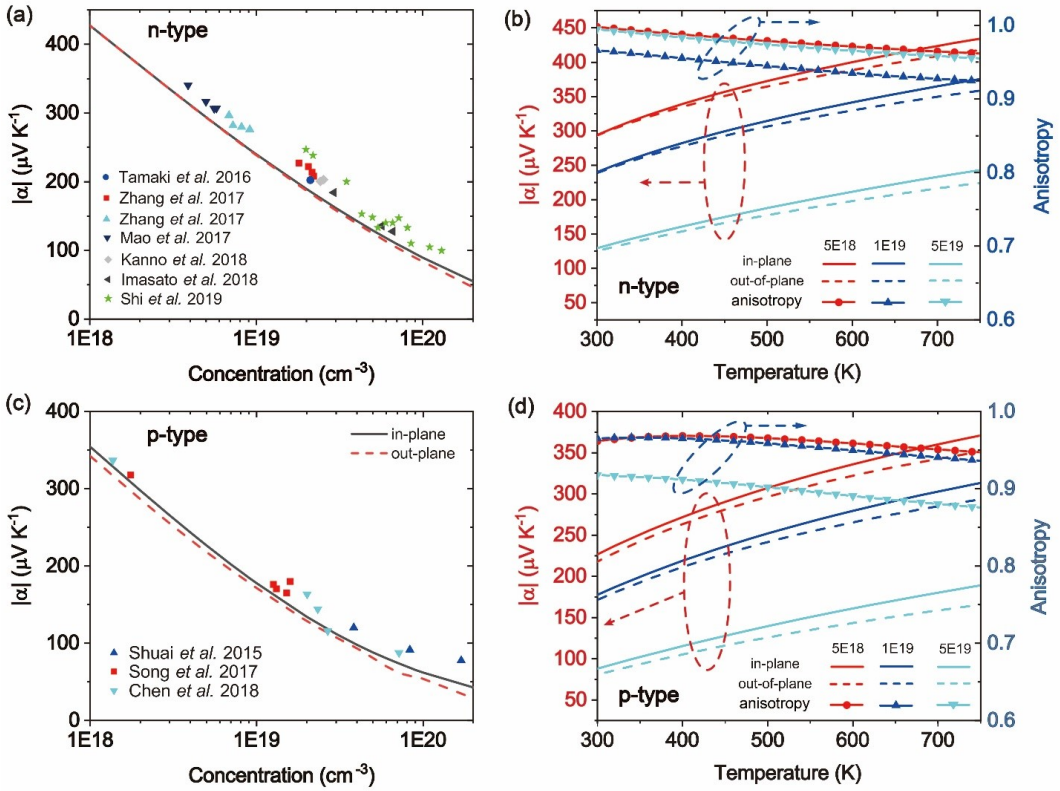

Figure 4.7: Room temperature Seebeck coefficient of (a) n-type and (c) p-type as a function of carrier concentration. Temperature dependent Seebeck coefficient and corresponding anisotropy (α^c/α^a) for (b) n-type and (d) p-type Mg_3Sb_2. The experimental data for n-type are taken from n-type Mg_3Sb_2-based alloys, e.g. Mg_3Sb_2-Mg_3Bi_2. [19, 20, 27, 28, 29, 30]. The p-type experimental data are taken from Refs[15, 23, 24].

average velocity. Per Equation 2.6, σ^{-1} is inversely proportional to the velocity squared; the velocity is also implicitly contained in $\mathbf{F}$ ($\mathbf{F} = \mathbf{v} \times \tau$), whereas ξ in Equation 2.7 is proportional to the velocity squared. So the velocity squared is cancelled out in the expression of Seebeck coefficient, leading to a nearly isotropic Seebeck coefficient. For both types, the calculated Seebeck coefficients are consistent with the experimental measured data over a wide range of carrier concentration [Figure 4.7(a) and (c)].

Because Seebeck coefficients depend more on the electronic band structure, it can be inferred from the alignment between our calculations and experimental

data that doping (for p-type) or alloying (for n-type) does not alter the electronic band structure to the first order, which thus justifies our calculations of electronic transport properties of n-type and p-type Mg_3Sb_2 by simply shifting the chemical potential of pristine Mg_3Sb_2. Experimentally, n-type Mg_3Sb_2 is achieved by alloying the Sb site with Bi element. Because the conduction band minimum is dominated by the s-orbital of Mg, alloying has trivial effect on the conduction band. In addition, the electrical transport properties of p-type Mg_3Sb_2 are typically optimized through minute doping, so the influence on the valence band is expected to be small.

With all the determinant quantities obtained, we calculate the zT for Mg_3Sb_2. Figure 4.8 depicts the contour map of zT for n- and p-type Mg_3Sb_2 as a function of temperature and carrier concentration. Nearly isotropic zT is attained for n-type Mg_3Sb_2, and the highest zT in both directions approaches 2.1 at 750 K with carrier concentration around 3×10^{19} cm^{-3}. To date, the highest zT achieved experimentally in n-type Mg_3Sb_2 is 1.85 at 723 K with carrier concentrations ranging from 3×10^{19} cm^{-3} to 3.5×10^{19} cm^{-3} [147]. The good agreement between experimental and our calculated zT confirms the reliability of our calculation methods. Strong anisotropic zT is obtained for p–type Mg_3Sb_2. In the ab-plane, the highest calculated zT is around 0.6 at 750 K with carrier concentration at 2×10^{19} cm^{-3}. This value is relatively smaller than what has been achieved from experiments of 0.8 at 773 K with carrier concentration around 10^{20} cm^{-3} for bulk polycrystalline p-type Mg_3Sb_2. However, it is astounding to find our calculated zT along the c-axis goes beyond unity, reaching a maximum value of 1.5 at 750 K with carrier concentration at 4×10^{19} cm^{-3}. In reality, Mg_3Sb_2 has native defects, like Mg vacancies [146]. Meanwhile, to tune the carrier concentrations, external defects are also introduced. Herein, we have employed the Brooks Herring model to study the defects scattering [169, 170] and find that the defects have a weak effect on the electrical transport properties (see Appendix B for

details). Specifically, the zT along the c-axis of p-type Mg_3Sb_2 is still greater than unity, with a maximum value of 1.42 at 750 K at a carrier concentration of 2×10^{19} cm^{-3}. This outcome is of great significance because it has been a long-going project to discover the p-type Mg_3Sb_2 with zT above unity considering that both p- and n-type legs are needed for power generation devices to maximize power output. It has been reported that highly oriented, textured Bi_2Te_3 could have significantly enhanced zT compared with a less-oriented sample [171, 172, 173]. Our finding could provide an insightful guide for experimental work. For example, it might be possible to achieve zT above unity for p-type Mg_3Sb_2 by properly oriented samples.

4.4 Summary

Anisotropic thermoelectric transport properties of pristine Mg_3Sb_2 are explored via parameter-free first principles calculations along with electron-phonon interactions (phonon-phonon interaction) limited Boltzmann transport equation for carriers (phonons) as implemented in Chapter 2. Nearly isotropic lattice thermal conductivity and Seebeck coefficient are observed, both of which align with the experimental data. Electrical conductivity and carrier thermal conductivity for n-type Mg_3Sb_2 are also nearly isotropic, originating from the similar effective masses along the a(b)- and c-direction. In contrast, large anisotropy was found for p-types, with the electrical conductivity and electrical thermal conductivity along the c-axis being four times of those in the ab-plane. The abnormal anisotropy is attributed to the much lower effective mass along the c-direction than that along a(b)-direction. Unlike Bi_2Te_3, Mg_3Sb_2 has strong inter-plane interactions, leading to a dispersive band along the Γ-A direction (crystallographic c-axis). The calculated zT for n-type Mg_3Sb_2 was 2.1 at 750 K in accordance with experimental data. Strong anisotropy of zT is found

in p-type Mg_3Sb_2; the largest zT in ab-plane and c-direction are 0.6 and 1.5 at 750 K, respectively. We also propose that, in practice, the performance of p-type zT might be enhanced by properly texturing polycrystalline samples.

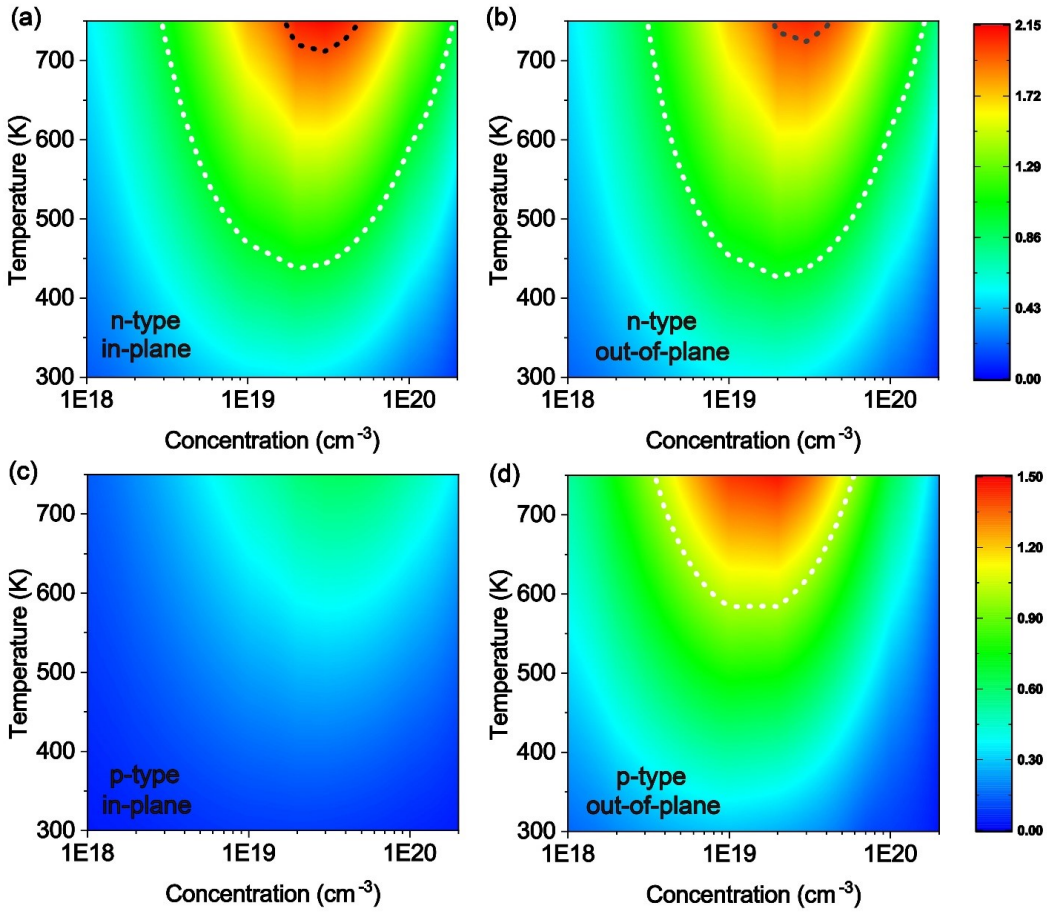

Figure 4.8: Contour map of zT as a function of both temperature and carrier concentration for Mg_3Sb_2: (a) n-type along the in-plane direction, (b) n-type along the out-of-plane direction, (c) p-type along the in-plane direction and (d) p-type along the out-of-plane direction. (a) and (b) share the same color bar, while (c) and (d) share the same color bar. The white (black) dotted line corresponds to zT equaling to 1.0 (2.0).

Chapter 5

Strain Effects on the Thermoelectric Performance of Two-dimensional alpha-Tellurium

After the discovery of graphene in the year 2004, physical properties of two dimensional materials have attracted tremendous attention. The thermoelectric performance of two dimensional materials is still an open question. Two dimensional transition metal dichalcogenides are reported to have large power factors; however, they are accompanied by large lattice thermal conductivity. Recently, it has been found that two dimensional alpha-tellurium exhibits low lattice thermal conductivity, which is a prefactor for excellent thermoelectric performance. Nevertheless, its thermoelectric performance is less studied. In this chapter, we calculated the thermoelectric transport properties of two dimensional alpha-tellurium without external strain and with tensile strain up to 4%, with the expectation to show our developed methods are able to handle the cases with reduced dimensionality.

5.1 Introduction

Two-dimensional (2D) materials have attracted tremendous interests from the point of view of reduced dimensionality as they can be cleaved or made nanosized. In the field of thermoelectric material research, 2D materials such as transition metal dichalcogenides (TMDs) [174, 175] have demonstrated their promise by possessing a large power factor (PF) comparable with the state-of-the-art bulk thermoelectric materials. On the other hand, TMDs often have thermal conductivities too high for good thermoelectrics. In parallel with the experimental study, theoretical calculations typically involved with simplifications on an electronic band structure and a scattering rate have been carried out to explore the thermoelectric promise of many 2D materials including MX_2 (M = Mo, W; X = S, Se), [176, 177, 178] MCO_2 (M = Ti, Zr, Hf) [179], TiS_2 [180], ZrS_2 [181], TiS_3 [182], black phosphorene [183], PdXY (X, Y = S, Se, Te) [184, 185], and Bi_2Te_2X (X = S, Se, Te) [186], to name a few. The results of these calculations do not yield zT values above unity due to a low power factor and/or high thermal conductivity. Recently, promisingly high zT values are predicted in emerging 2D materials, such as PbI_2 [187], KAgSe [188] and pentasilicene [189]. Nonetheless, the phenomenological models with simplifications generally lack enough predictive power. Hence, there is a demanding need for first principles (parameter-free) calculations of the performance of thermoelectric materials using the methods developed in Chapter 2.

From the computational perspective, the materials to be modeled would be structurally simple enough so the results are reliable yet thermoelectrically good enough. Therefore, the results are of immediate practical implication. Elemental Te is such a material. Recently, Lin *et al.* [190] reported polycrystalline bulk Te as a good thermoelectric material with zT up to 1.0 at 600 K. zT = 1.0 is regarded as the

benchmark for practical thermoelectric materials. This discovery is ground breaking in that most known good thermoelectric materials are multinary semiconductors or semimetals, whereas Te is elemental. On the other hand, the experimental results of Te are derived from polycrystalline samples, which does not fully reflect the thermoelectric potential of Te, given its anisotropic crystal structure. Hence, inspired by the reduced dimensionality approach mentioned above and in the light of the layered crystal structure of Te, the intrinsic thermoelectric performance of monolayer Te needs to be studied.

To this end, Zhu *et al.* [191] predicted that monolayer Te could possess two semiconductor phases, named α-Te and β-Te using density functional theory (DFT) calculations. The α-Te phase is stable, whereas β-Te is metastable. [191] The authors also pointed out that monolayer α-Te could be readily obtained *via* a thickness-dependent structural phase transition along the [001] direction of the trigonal bulk Te, whereas the β-Te phase could be derived by the structural relaxation when the bulk helical chain structure is truncated along the equivalent [010] or [100] direction. So far, only the β-Te phase has been experimentally obtained using molecular beam epitaxy growth on a highly oriented pyrolytic graphite (HOPG) substrate [191, 192] and a graphene/6H-SiC substrate [193]. The interactions from the substrate during Te growth prevent β-Te from transforming into a more stable α phase. Nonetheless, when grown on a substrate that is more chemically bounded (yet not too strong) than HOPG and graphene/6H-SiC substrate, α-Te is expected. [191]

Regarding the thermoelectric performance of monolayer Te, previous studies showed that κ_L of α- and β-Te are lower than 10 $Wm^{-1}K^{-1}$ above room temperature, [194, 195, 196] much smaller than that of monolayer TMDs. [197, 198] Nonetheless, the studies of full thermoelectric transport properties are scarce. The electrical transport properties in previous studies are estimated based on a roughly constant

relaxation time, [195, 196] which in real life depends on carrier modes, carrier concentrations, and temperatures. Therefore, more accurate study is highly desired. To accurately calculate the electrical transport properties, first principles calculations have not been made possible until recently by solving the Boltzmann transport equations (BTE) with scattering limited by the electron-phonon interactions obtained from DFT and density functional perturbation theory (DFPT). [77, 81, 199, 200, 201] Electron phonon interactions are typically the dominant mechanism at an elevated temperature, where the zT value peaks. In this work, we calculate full thermoelectric transport properties along with zT of the monolayer α-Te from first principles and parameter-free BTE. Considering the fact that the monolayer Te is grown on a substrate, mismatch in the lattice constants could result in strain, either compressive or tensile; the strain effect is studied.

5.2 Computational Details

The DFT and DFPT calculations were carried out in the Quantum Espresso package [114] using full relativistic norm-conserving pseudopotentials with local density approximation (LDA) exchange-correlation functional. [115] Figure 5.1 shows the crystal structure of monolayer α-Te in the real space, which adopts a trigonal P$\bar{3}$m1 (No. 164) space group. The relaxed lattice constant is a = 4.14 Å, in agreement with the literature data. [191, 195] In a side view, there are three Te atomic planes, with a distance between the upper and lower atomic planes of d = 3.60 Å. The crystal structure is not mirror symmetrized with respect to the middle atomic plane. The vacuum space perpendicular to the atomic plane was fixed to be 20 Å to eliminate the interactions between layers. For the properties normalized by volume, an effective thickness of 7.72 Å was adopted, also known as the distance between surface Te

atomic planes plus the van der Waals radii of a Te atom. [195] The electron energy, phonon dispersion, and electron-phonon coupling were initially calculated on 8×8×1 **k** and 8×8×1 **q** grids. To calculate electrical transport properties, Wannier function interpolation was employed as implemented in EPW package. [85] To calculate κ_L, the thirdorder anharmonic interatomic force constants were calculated using a 4×4×1 supercell with 3×3×1 **k** sampling, and a force cutoff distance of 0.6 nm was employed. The ShengBTE package [58] was used for iteratively solving the phonon BTE. Considering the melting point of bulk Te is about 723 K, the thermoelectric properties of monolayer α-Te are discussed between 300 and 700 K. Here, we focus on the bulk transport properties of α-Te, a 2D hexagonal lattice structure with infinite in-plane extension. The isotropy of in-plane bulk transport properties is guaranteed by the lattice symmetry. The impact of zigzag and armchair configurations, which may yield directional transport properties in nanoribbons, is thus not relevant in this work. Thus, the electrical and thermal transport properties of monolayer α-Te in the basal plane are regarded as scalars hereafter.

5.3 Results and Discussions

5.3.1 Mobility and Lattice Thermal Conductivity

The calculated band structure of α-Te with the spin-orbit coupling (SOC) considered is shown in Figure 5.2. As shown, the SOC significantly alters the band structure. Since the electrical transport properties are markedly affected by the band structure as demonstrated in Chapter 3, the SOC must be included to achieve high accuracy for the calculated mobility. α-Te has an indirect band gap, about 0.37 eV, with the conduction band minimum (CBM) located at Γ and the valence band

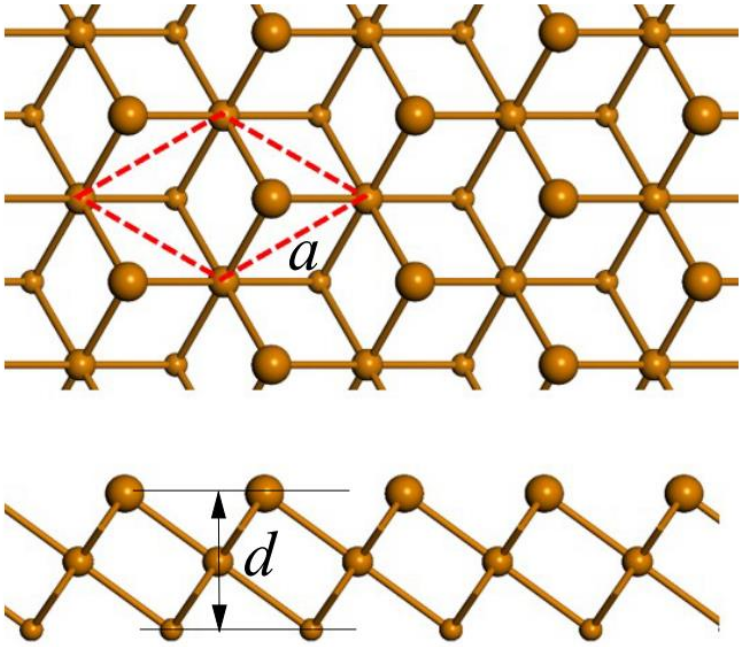

Figure 5.1: Top and side views of the crystal structure of monolayer α-Te with the primitive cell indicated by the red dashed lines.

maximum (VBM) located in the Γ-M line and its equivalent positions in the first Brillouin zone. Since LDA underestimates the band gap, the GW correction was employed using YAMBO code [202], and the band gap is opened up to 0.69 eV (cf. Figure 5.3), only a little smaller than the previous calculation (0.75 eV) [191] using VASP [203] with HSE06 functional [160, 161, 162] including SOC. The real band gap is 10 times larger than thermalization energy below 700 K, *i.e.*, 10 $k_BT \approx 0.60$ eV; thus the bipolar effect is negligible in the electrical transport. [204, 205] Therefore, the electron and hole transports were calculated using conduction and valence bands separately, with chemical potential manually shifted with respect to CBM and VBM, respectively.

The band structure is flatter near the VBM compared to that near the CBM, suggesting a larger effective mass for VBM. In previous studies, the valence and conduction bands around band edges were treated as isotropic. [191, 195] However, we

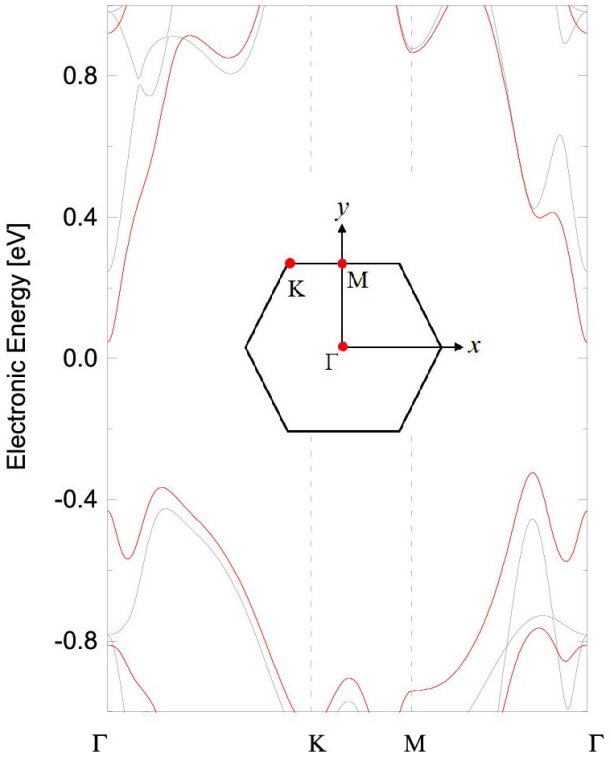

Figure 5.2: Electronic band structure with (red) and without (gray) the spin-orbital coupling effect along high symmetry directions of reciprocal space shown in the inset.

found that such isotropy is oversimplified for holes. As seen in the energy-momentum contours of Figure 5.4, the CBM edge is indeed isotropic with an effective mass of 0.10 m_0, in agreement with previous results. [191, 195] However, the VBM edge is strongly anisotropic, with $m_x^* = 0.39m_0$ and $m_y^* = 0.17m_0$ when fitting the valley in the Γ-M line along the x and y directions. Previous studies only fitted the hole effective mass along the Γ-M line, *i.e.*, m_y^*, and reported similar values. [191, 195] It is important to note that despite the anisotropic shape of each hole pocket and thus the anisotropic hole effective masses along the x and y axes, as shown in Figure 5.4(b), the hole transport properties are isotropic in the basal plane due to the crystal lattice symmetry embodied in the space group P$\bar{3}$m1 (No. 164) of α-Te. Figure 5.5 shows the phonon dispersion of α-Te. The maximum phonon frequency corresponds to an

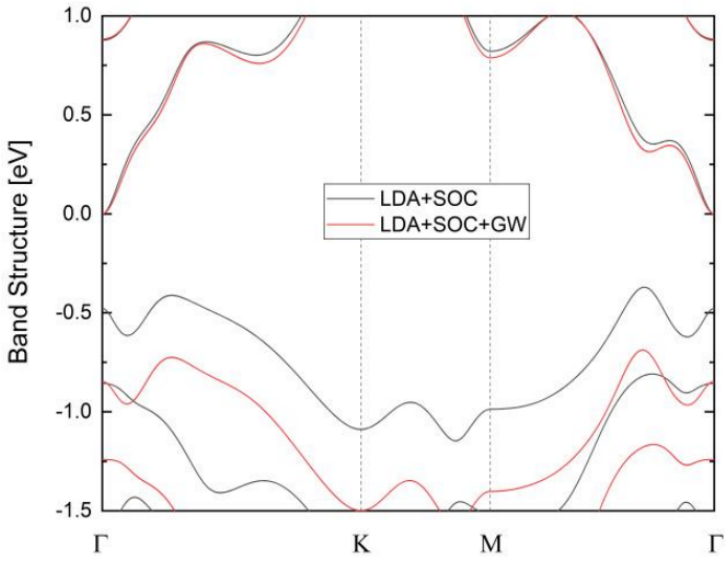

Figure 5.3: Band structures of monolayer α-Te calculated with and without GW correction, where the conduction band minimum is shifted to zero.

energy of 23 meV, smaller than most of the 2D materials [176, 177, 178, 179, 180, 181, 182, 183] due to the heavy atomic mass of Te, but is comparable to other low κ_L systems. [184, 185, 186] The low phonon frequency renders a low Debye temperature for α-Te.

To calculate the carrier mobility, the q grids were interpolated to 120×120×1 for phonons, whereas the k grids were interpolated to 360×360×1 and 120×120×1 for electrons and holes, respectively, which are enough to ensure the convergence [Figure 5.6]. The calculated intrinsic electron and hole mobilities of α-Te at different temperatures are plotted in Figure 5.7(a). Remarkably, the room-temperature electron mobility reaches as high as 2500 $cm^2V^{-1}s^{-1}$, outperforming many other 2D materials such as TMDs [77, 206], InSe [207], black phosphorene [206, 208]and antimony [209]. Meanwhile, this electron mobility is about two orders of magnitude larger than the hole mobility, which is only about 30 $cm^2V^{-1}s^{-1}$ at room temperature. This tallies with the usual situation that materials have high mobility for only one type of car-

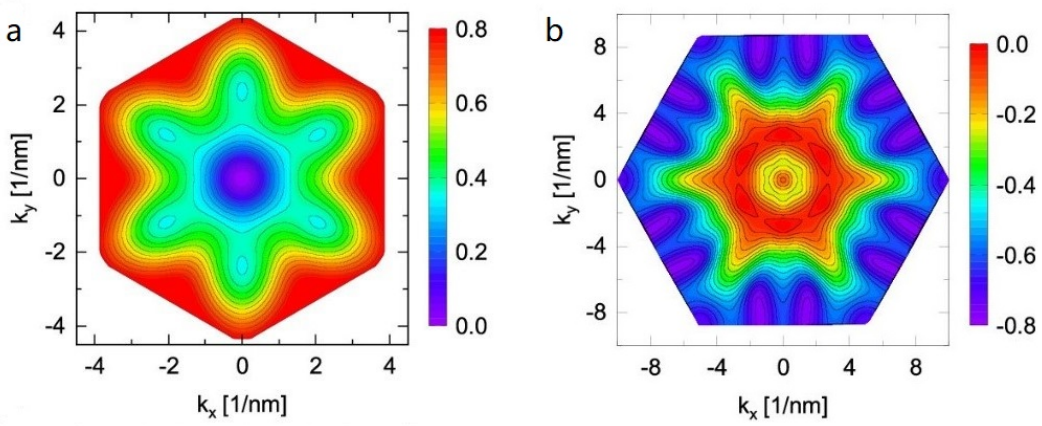

Figure 5.4: The electronic energy versus the wave vector for the (a) conduction band and the (b) valence band around the band edge

rier, such as Si [81, 83], SiC as reported in Chapter 3 [165], GaN [210], InSe [207], and so on. We note that the estimations based on a simplified phenomenological model with isotropic parabolic bands and acoustic deformation potentials correctly give a high electron mobility ($\sim cm^2V^{-1}s^{-1}$). [191, 195] This is expected because the electron transport at low temperatures with a low carrier concentration is mainly governed by the low-energy electrons in the Γ valley, reasonably described by the isotropic parabolic relation. Nonetheless, the deformation potential model is crude, which completely ignores the nonparabolicity of the band structure, the mode- and temperature-dependences of electron-phonon scattering, to name a few. For instance, using the acoustic deformation potential model, the electron mobility of monolayer MoS_2 is either overestimated by twice [211] or underestimated by half [212] as compared to the first-principles calculations [77]. It can be seen that the hole mobility of α-Te is overestimated ($\sim 1700\ cm^2V^{-1}s^{-1}$) [191, 195] by about two orders of magnitude.

The remarkably smaller hole mobility as compared to the electron is due to the heavier effective mass, which results in not only a smaller group velocity but also

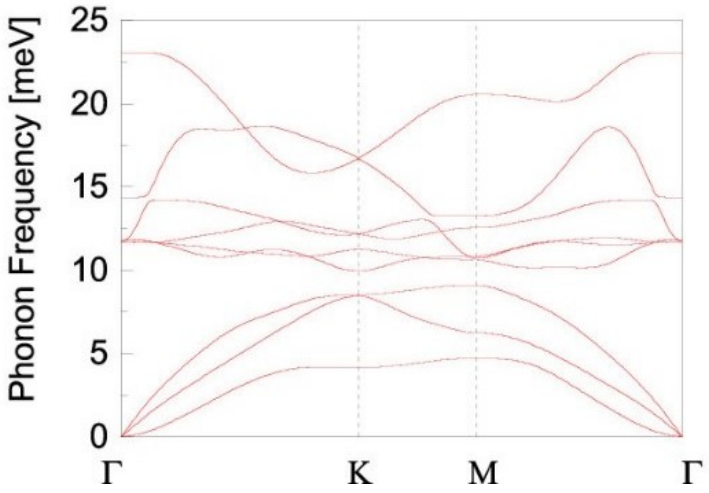

Figure 5.5: Phonon dispersion relation of α-Te.

much stronger scattering rates. As shown in Figure 5.7, the scattering rates of electrons at room temperature are much lower than those of holes, except in a narrow neighborhood of 0.4 eV. The scattering rates of electrons are also lower than that of MoS_2 [77], InSe [207], and black phosphorene [208]. This is a combined consequence of a small effective mass and a low Debye temperature. The electron-phonon scattering process requires energy and momentum conservations between electrons and phonons. Generally, the closer the difference in the energy scale between the electron and the phonon, the more easily the conservation criteria can be satisfied. The characteristic energy scale of electrons (on the Fermi level) is on the order of eV, while the counterpart of phonons varies between 1 and 100 meV. A lower Debye temperature generally corresponds to lower phonon energies, thus a larger energy difference between electrons and phonons and a smaller scattering phase space. In this case, the scattering rates are expected to be small and favor the electrical conductivity. By looking into the decomposed contribution to the scattering rates from out-of-plane acoustic (ZA), transverse acoustic (TA), longitudinal acoustic (LA), and optical (OP) phonons in Figure 5.7(c) and (d), we can see that the ZA and OP phonons contribute

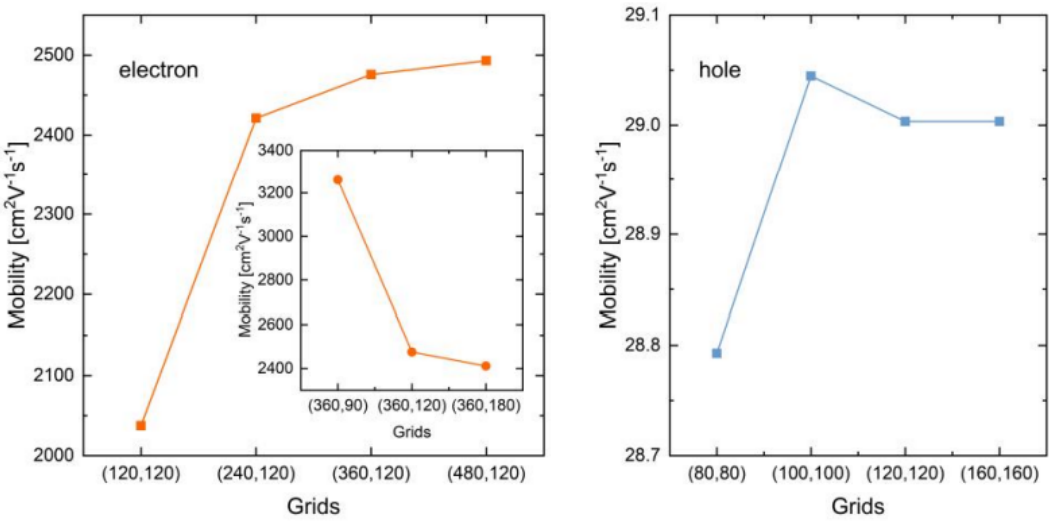

Figure 5.6: Convergence of electron and hole mobilities with respect to **k** and **q** grids at room temperature. The $(N1, N2)$ in the labels of horizontal axis indicates $N1 \times N1 \times 1$ for **k** grids and $N2 \times N2 \times 1$ for **q** grids.

the most at relatively low energies, while the contribution of TA and LA increases as the energy increases. Unlike MoS_2 but as in silicene and stanene, [213, 214, 215] ZA contributes significantly to the scattering, which originates from the broken mirror symmetry of the crystal structure. [216] For 2D systems with mirror symmetry, the ZA phonons have purely out-of-plane polarization vectors and the in-plane Bloch waves are mirror symmetric; therefore, the electrons and ZA phonons are decoupled to the first order and the coupling matrix elements vanish. On the other hand, in buckled 2D systems, where the mirror symmetry is broken, the cancelation no longer applies.

The temperature-dependent κ_L of α-Te was calculated, as shown in Figure 5.8, with a value of 4.2 $Wm^{-1}K^{-1}$ at 300 K and 1.8 $Wm^{-1}K^{-1}$ at 700 K, which are about half smaller than the values reported by Gao *et al* [195]. We have carefully checked the convergence of κ_L (the details are given in Appendix C) and found that the calculated κ_L would be overestimated if the computational parameters especially the scalebroad

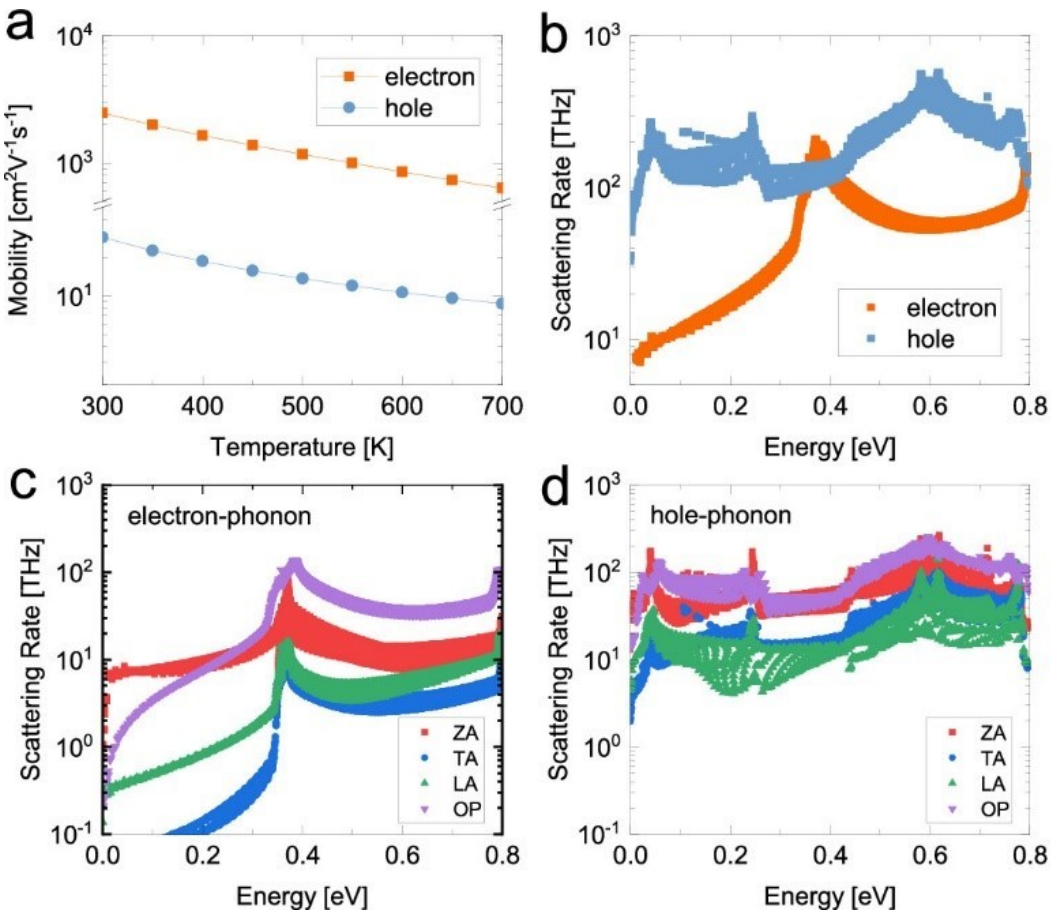

Figure 5.7: (a) Intrinsic electron and hole mobilities of α-Te as a function of temperatures. (b) Electron and hole scattering rates at room temperature and the (c, d) corresponding decoupled scattering contributed from different phonon modes for electrons and holes, respectively.

used in ShengBTE package [58] are insufficient for the convergence. κ_L of monolayer α-Te is much smaller than monolayer TMDs [197, 198], black phoshperene [217], InSe [218], but close to the recently reported thermoelectric monolayer of Bi_2Te_2X (X = S, Se, Te) [186], β-Te [194], and organic $(NiC_4S_4)_n$ [219]. The low κ_L is due to a low Debye temperature, which suggests a small group velocity and small phonon lifetimes. [220, 221] κ_L is mainly contributed by phonons with a relaxation time below 100 ps at room temperature, as shown in the inset of Figure 5.8, which is smaller than the monolayer TMDs [198], InSe [218], and β-Te [194]. The acoustic phonons, of which

the frequency is smaller than 10 meV, contribute more than 70% of κ_L above room temperature.

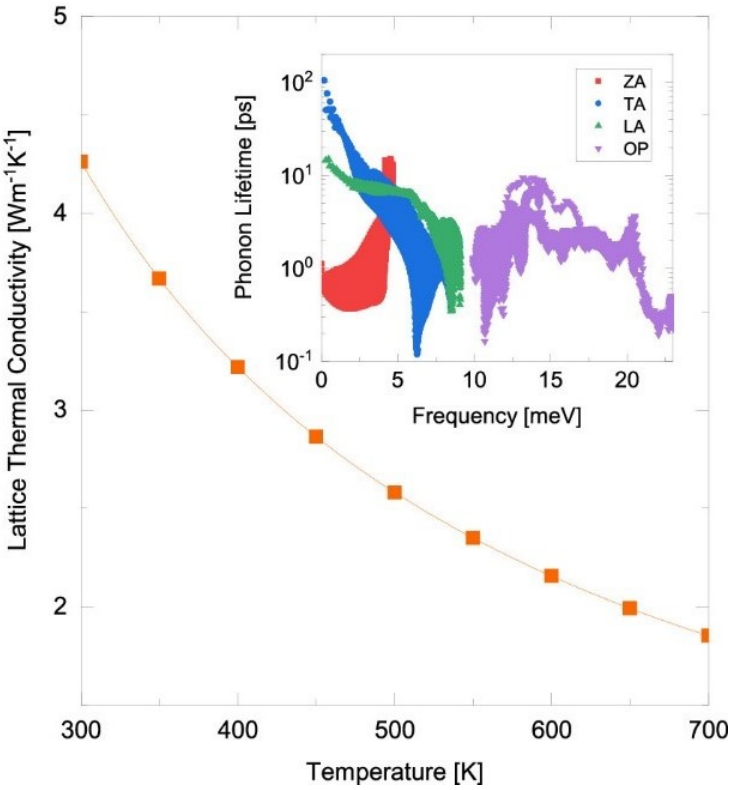

Figure 5.8: Lattice thermal conductivity and room-temperature phonon lifetimes of different modes.

5.3.2 Thermoelectric Figure of Merit

The high electron mobility and low lattice thermal conductivity are key ingredients for high zT. The carrier concentration dependence of zT (Figure 5.9) was calculated at a number of temperatures and is shown $10^{19}cm^{-3}$ in the case of n-type α-Te. As temperature decreases, the maximum zT is reduced. However, at 300 K, it is still as large as 0.55 at an electron concentration of $5 \times 10^{18}cm^{-3}$. The zT of p-type α-Te was also calculated, which is much smaller than the n-type counterpart

at the same carrier concentration because of the much lower hole mobility. Nonetheless, as the hole concentration increases to $5 \times 10^{20} cm^{-3}$, the maximum zT of p-type α-Te can reach 0.86 at 700 K, whereas the highest room-temperature value is about 0.25 at a hole concentration of $2.5 \times 10^{20} cm^{-3}$. It is also found that the optimal carrier concentrations of unstrained α-Te are $(5-10) \times 10^{18} cm^{-3}$ for the n-type and $(2.5-5) \times 10^{20} cm^{-3}$ for the p-type α-Te over the whole temperature range of 300-700 K.

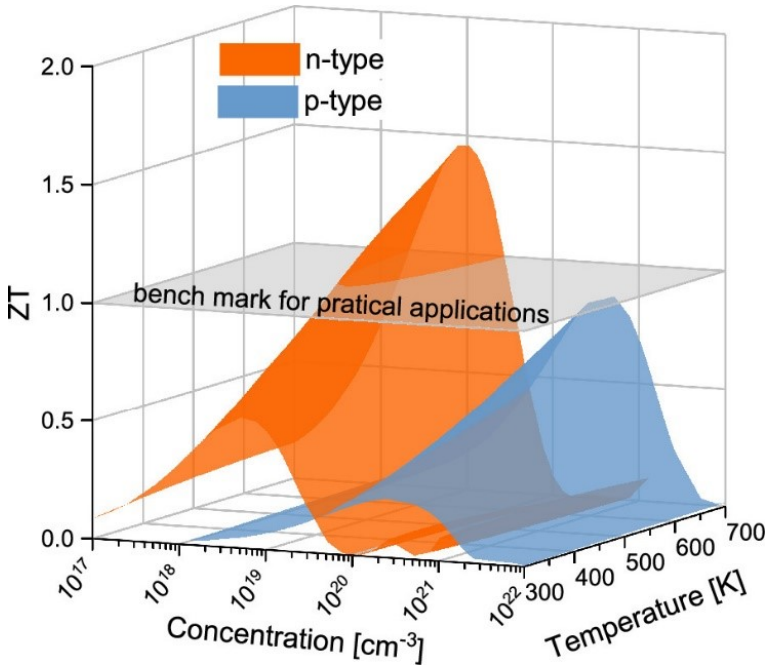

Figure 5.9: Thermoelectric zT of n- and p-type α-Te as a function of carrier concentrations and temperatures.

Figure 5.10 provides the individual thermoelectric properties of n- and p-type α-Te as a function of carrier concentrations at 300 and 700 K. For an n-type system, in 5.10(a) and (b), as electron concentration increases, α decreases while σ and κ_e increase; consequently, the PF and zT have a peak shape as the function of carrier concentrations. At 300 K, α and σ at the optimal concentration of zT are 218 $\mu V K^{-1}$ and 1943 $S cm^{-1}$, respectively, producing remarkably high PF of 92 $\mu W cm^{-1} K^{-2}$. As

temperature increases, α is slightly increased while σ is significantly reduced, and thus the PF is decreased. At 700 K, the PF at the optimal carrier concentration of zT is approximately reduced by half to 50 $\mu W cm^{-1}K^{-2}$. The decrease of PF arises from a slight increase of α to 227 $\mu V K^{-1}$ and a strong decline of σ to 973 Scm^{-1}. The corresponding κ_e is also reduced from 0.8 $Wm^{-1}K^{-1}$ at 300 K to 0.6 $Wm^{-1}K^{-1}$ 700 K; combined with the reduced κ_L, the total thermal conductivity is reduced by half. As shown in Figure 5.10(c) and (d), the thermoelectric properties of p-type α-Te exhibits similar concentration dependence and temperature dependence as their n-type counterparts. Specifically, at the optical carrier concentration of zT, the PF of p-type α-Te are 39 and 30 $\mu W cm^{-1}K^{-2}$ at 300 and 700 K, respectively, which are about half smaller than that of n-type α-Te. Smaller PF of a p-type system leads to lower zT. It is noted that at the optimal carrier concentration the total thermal conductivity is mainly contributed by phonons. For instance, about 85 and 75% thermal conductivity is contributed by κ_L at 300 and 700 K, respectively, for both n- and p-type systems.

5.3.3 Strain Effects

Strain, which cannot be avoided in realistic samples, has important influence on the transport properties. It has been reported that the thermoelectric performance of monolayer ZrS_2, TiS_2, and InSe can be enhanced by tensile strain. [180, 181, 222] Therefore, we also studied the tensile strain effect on the properties of α-Te for 1, 2, 3, and 4% strains. Figure 5.11(a) shows the tensile strain effect on electron and hole mobilities. It can be seen that the electron mobilities increase significantly, which reach up to 8000 $cm^2V^{-1}s^{-1}$ at room temperature above 2% strain. As temperature increases to 700 K, the enhancement of electron mobility by tensile strain is reduced,

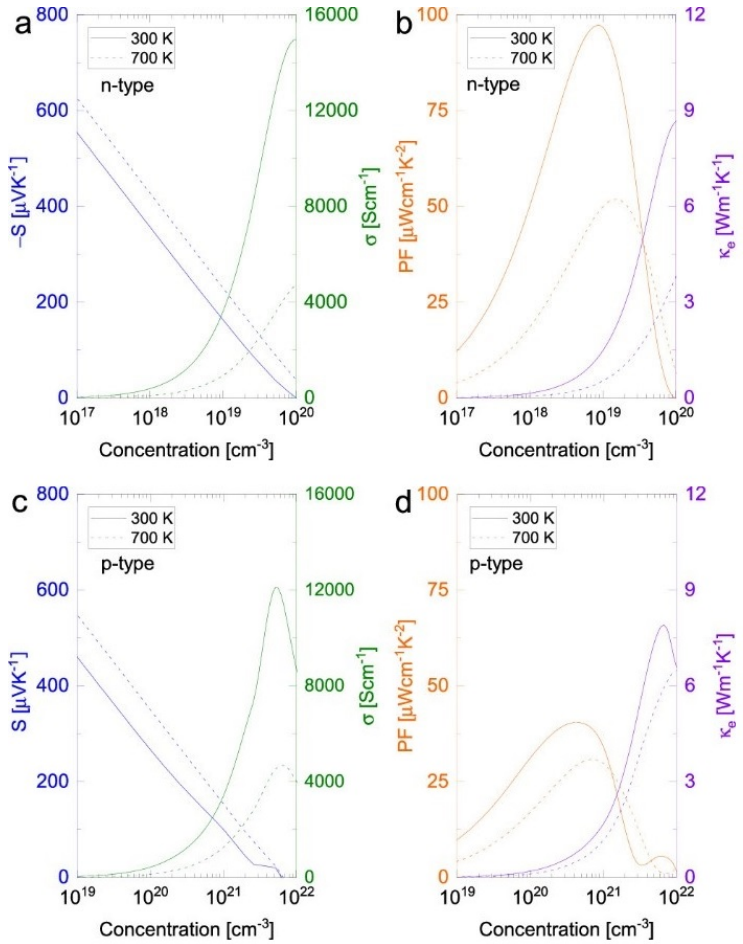

Figure 5.10: Seebeck coefficient (α), electrical conductivity (σ), electronic thermal conductivity (κ_e), and the power factor (PF) of (a, b) n- and (c, d) p-type α-Te as a function of carrier concentrations at 300 and 700 K, respectively.

but still more than doubled as compared to an unstrained system, from 630 to 1515 $cm^2V^{-1}s^{-1}$. It is also found that the electron mobilities under 2, 3, and 4% strains are almost identical, indicating that strain effect gets marginal above 2% strain. The tensile strain effect on mobility can be understood from the scattering rates, as shown in Figure 5.11 (b) and (c), and from the variations of the band structures as in Figure 5.1. Overall, for strain changing from -1% to 4%, the conduction band tends to become steeper, whereas the valence band tends to become flatter. The change of

band structure around CMB and VBM is not significant. To better characterize the small changes of effective mass under stains, we derived the fitting from the constant energy contours as in Figure 5.13. The fitted effective masses are listed in Table 5.1. The valley around CBM is located at *Gamma* point and is isotropic, as shown in Figure 5.13(a). When the strain varies from -1% to 4%, the electron effective mass is slightly reduced. The valley around VBM is not located at Γ point, and thus there are six equivalent valleys originating from the lattice crystal symmetry, as shown in Figure 5.13(a). As the strain varies from -1% to 4%, the hole effective mass along the y-direction is clearly increased, whereas the hole effective mass in the x-direction does not vary monotonically due to the strong nonparabolicity. However, since the change of the constant energy contour in the y-direction is larger than that in the x-direction, as shown in 5.13(b), the enlarged area of constant energy contour implies the equivalent increase for hole effective mass.

For an unstrained system, the ZA phonons dominate the scattering of electrons at low energies as compared to other phonon modes, partially because of the divergent thermal population of the quadratic ZA phonons. [216] Upon strain, the ZA phonons get stiffened, and the dispersion changes from quadratic to linear as in Figure 5.14. Consequently, the thermal population of the quadratic ZA phonons is significantly reduced. Therefore, the scattering rates by ZA phonons decrease by more than one order of magnitude at 2, 3, and 4% strains. For a given electron state, smaller effective mass means fewer electron states available for phonon scattering in the momentum space. The small scattering phase space corresponds to a small scattering rate. The scattering rates by TA, LA, and OP phonons are almost unchanged, implying the weak effect from the change of electron effective mass. Therefore, the significant enhancement of electron mobility stems from the great decrease of electron-ZA phonons scattering. As for holes, we found that the tensile strain also reduces the

Strain	Electron ($m_x^* = m_y^*$)	Hole (m_x^*)	Hole (m_y^*)
-1%	0.100	0.37	0.16
0%	0.097	0.39	0.17
1%	0.094	0.37	0.18
2%	0.092	0.38	0.20
3%	0.090	0.38	0.22
4%	0.099	0.39	0.25

Table 5.1: Effective masses of electron (by fitting the CBM valley at Γ point) and hole (by fitting the VBM valley in Γ-M line) under different strains.

scattering rates by ZA phonons but increases the scattering rates by other phonons (as in Figure 5.15) due to the equivalently increased hole effective mass. Since the ZA phonons scattering is not dominant for holes, the total scattering rates of holes are increased. As a result, the hole mobilities under tensile strains decrease slightly, for instance, from 30 to 23 $cm^2V^{-1}s^{-1}$ by 4% strain at room temperature. Unlike electron mobilities, the change of κ_L caused by tensile strain is also not strong. At room temperature, κ_L first increases from 4.2 to 5.7 $Wm^{-1}K^{-1}$ with 2% strain and decreases again to 4.3 $Wm^{-1}K^{-1}$ at 4% strain, which is a result of the complicated change of mode-dependent phonon group velocity and phonon lifetime.

The effect of compressive strain is also studied. It is found that -1% compressive strain has limited effects on the electronic band structure near the band edges (Figure 5.12) but results in imaginary frequencies of ZA phonons near the Γ point (Figure 5.14). Imaginary frequencies are not allowed in the calculations of electron-phonon coupling; with the imaginary ZA modes manually removed, the resulting electron mobility is significantly enhanced, while the hole mobility is much less affected (Figure 5.16). Although the physical meaning is discounted because imaginary phonon modes do not exist in real life materials, these results attest to the vital role of the coupling between electrons and the ZA modes in relation to the electron mobility

(Figure 5.17). In short, any strain-induced change to the ZA phonon modes would drastically impact the electron mobility. It should be noted that the strain effect on carrier mobility has a different origin in monolayer α-Te and bulk GaN. Poncé *et al.* [210] reported that the hole mobility of bulk GaN can be significantly increased by both tensile and compressive strains due to the upshift of the light split-off hole band. These results showcased the efficacy of strain in tuning the electronic band structure of materials with multiple bands close in energy but differing in the effective mass. By contrast, the electronic bands of α-Te are well separated in energy and the strain effect is limited. Rather, the strain effects of electron mobility in α-Te is governed by the strain effects of the ZA phonon modes and the resulting change of electron-phonon scattering.

The noticeably increased electron mobility portends significant increase of σ and κ_e in a n-type system, whereas α is only weakly affected since it is mainly determined by the band structure [111]; as a consequence, loosely speaking, the overall trend of PF is increased (Figure D.1 in Appendix D). As discussed above, κ is dominated by κ_L that is less changed upon strain. The zT of n-type α-Te is generally enhanced by the tensile strain, as shown in Figure 5.18(a). The optimal concentration of n-type α-Te varies only slightly with 1-4% tensile strain in the range of $(2.5 - 7.5) \times 10^{18} cm^{-3}$ over the temperature range of 300-700 K. By contrast, σ and PF of p-type *alpha*-Te are decreased by tensile strain (Figure D.2 in Appendix D) in consistence with the reduced hole mobility, and the zT becomes worse, as shown in Figure 5.18(b).

The optimal concentration of p-type α-Te is also weakly affected by the tensile strain in the range of $(2.5 - 5) \times 10^{20} cm^{-3}$ over the temperature range of 300-700 K. Figure 5.19 shows the maximum zT under different strains and temperatures for n- and p-type *alpha*-Te. The maximum zT of the n-type system increases first at

1% strain due to the increase of σ but decreases at 2 and 3% strains due to the increase of κ_L. When the strain increases up to 4%, the zT increases again because κ_L reduces to the level of no strain. At room temperature, the enhanced zT is 0.94. When temperature increases to 700 K, the optimal zT can be as high as 2.03, which is comparable with the famous bulk thermoelectric SnSe at close temperatures. [141, 223] In contrast, it is found that the zT of a p-type system is decreased by tensile strain due to its deteriorated hole transport properties. From the concentration and temperature dependences of the calculated zT of 4% strained n-type *alpha*-Te, it is found that the zT can be larger than unity over a wide electron concentration and temperature ranges, promising realistic applications. The thermoelectric zT of ntype *alpha*-Te is much better than previously estimated β-Te [196] due to its much smaller effective mass and the promising strain effect.

5.4 Summary

In summary, the intrinsic electrical and thermal transport properties of monolayer α-Te were studied based on parameter-free first-principles calculations and the solution of the electron phonon interaction limited Boltzmann transport equation as developed in Chapter 2. It is found that α-Te has ultrahigh electron mobility despite hole mobility is two orders of magnitude lower. The room temperature electron and hole mobilities are 2500 and 30 $cm^2V^{-1}s^{-1}$, respectively. Because of the absence of mirror symmetry in the crystal structure, the heavily populated out of-plane acoustic (ZA) phonons play a key role in the scattering of a charge carrier. Meanwhile, the lattice thermal conductivity of α-Te is lower than many previously reported monolayer materials due to its low phonon frequency and short phonon lifetime. Above room temperature, the lattice thermal conductivity is lower than 4.2 $Wm^{-1}K^{-1}$.

As a result, monolayer α-Te displays good thermoelectric performance; the zT value reaches 1.46 and 0.86 at 700 K for pristine n- and p-type systems, respectively, while the room-temperature counterparts are 0.55 and 0.25. Notably, the tensile strain significantly enhances the zT of an n-type system mainly due to strain-induced linear dispersion of ZA modes and the resulting suppressed carrier scattering by ZA modes. The peak zT values are enhanced to 0.94 and 2.03 by a 4% tensile strain at 300 and 700 K, respectively. By contrast, strain degrades the thermoelectric performance of p-type monolayer α-Te. These results are expected to promote the experimental study of monolayer α-Te *via* doping, alloying, and compositing.

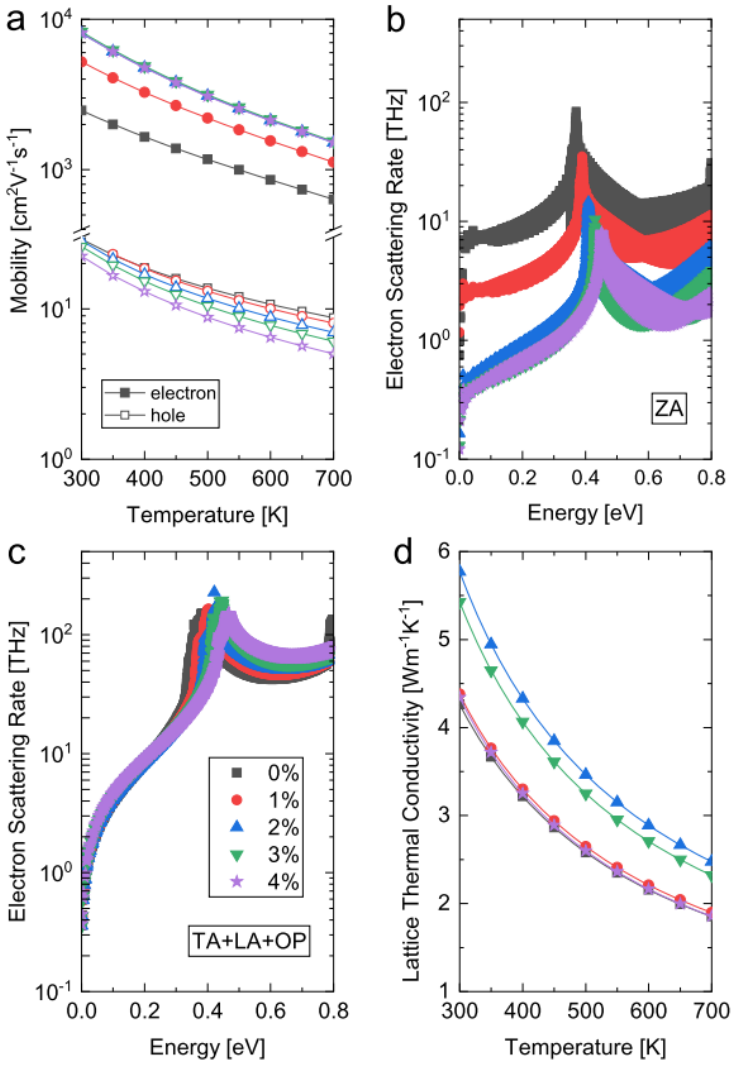

Figure 5.11: Tensile strain effect on (a) electron and hole mobilities, (b) electron scattering contributed by ZA phonons, (c) electron scattering contributed by TA, LA, and OP phonons, and (d) lattice thermal conductivity, respectively.

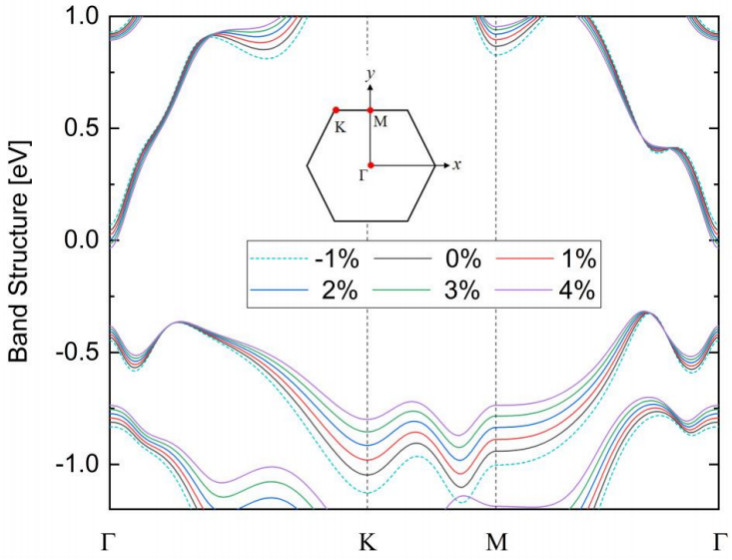

Figure 5.12: Band structures of monolayer α-Te (*aka* 0%) and the effects of compressive and tensile strains.

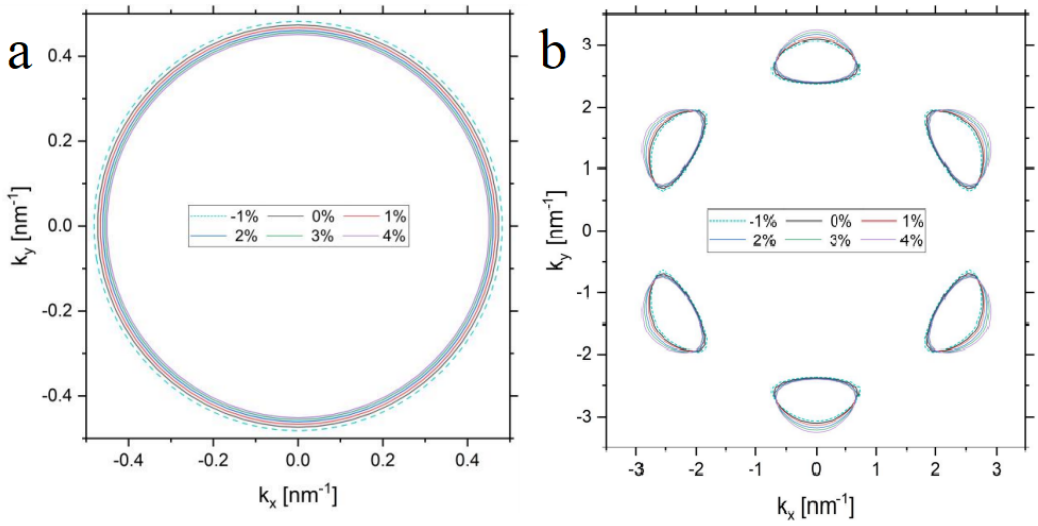

Figure 5.13: Constant energy contour of (a) conduction band (at 0.1 eV with respect to CBM)and (b) valence band (at -0.03 eV with respect to VBM) as a function of wavevector under different strains.

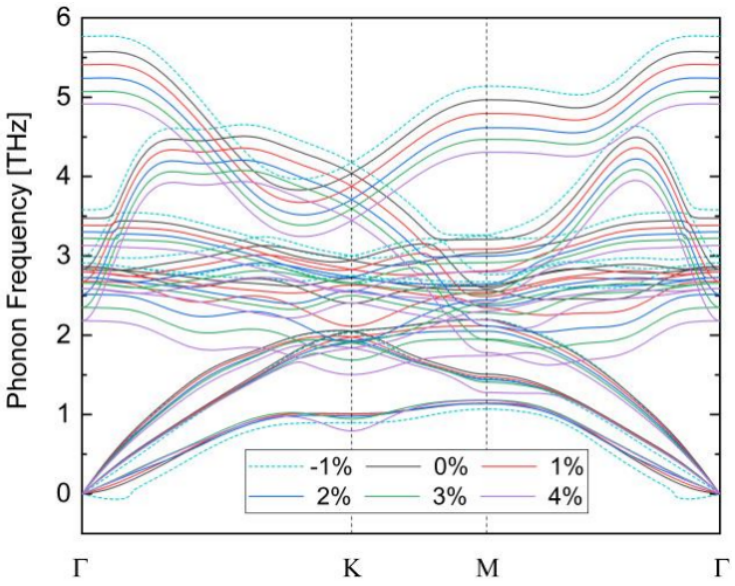

Figure 5.14: Phonon dispersions of monolayer α-Te (*aka* 0%) and the effects of compressive and tensile strains.

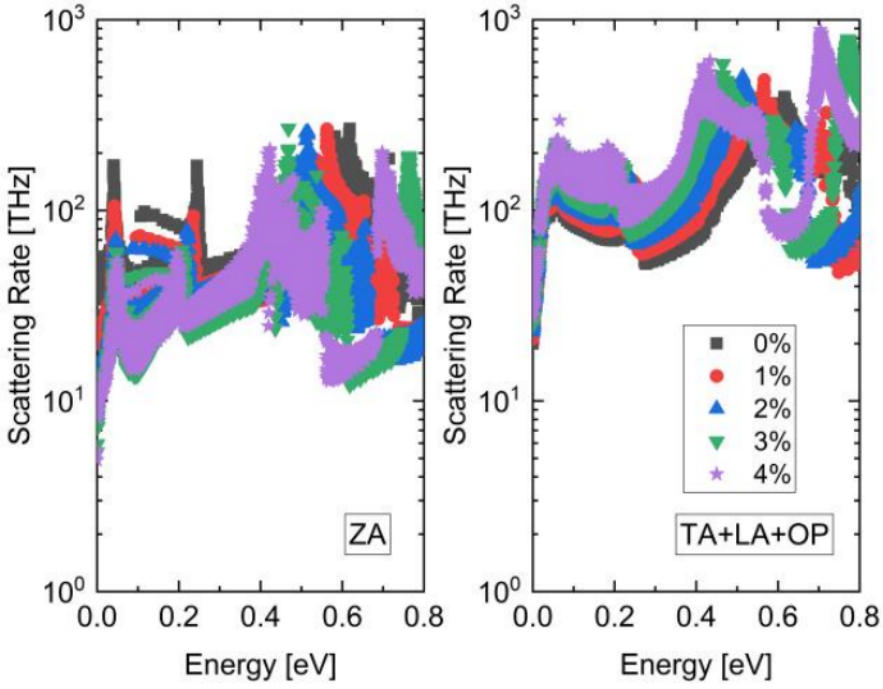

Figure 5.15: Scattering rates of holes contributed by ZA phonons and other phonon modes under different tensile strains at room temperature.

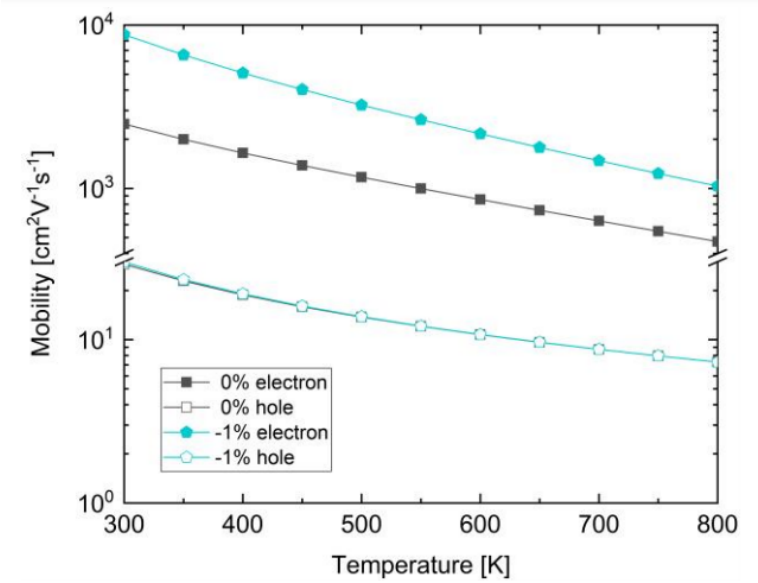

Figure 5.16: Effects of compressive strain on the electron and hole mobilities of monolayer α-Te at different temperatures.

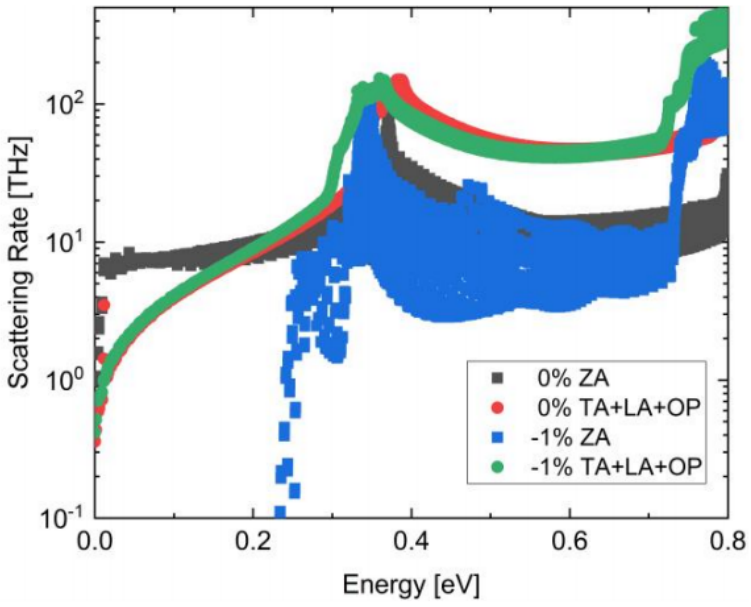

Figure 5.17: Effects of compressive strain on the scattering rates of electrons contributed by ZA phonons and other phonon modes at room temperature.

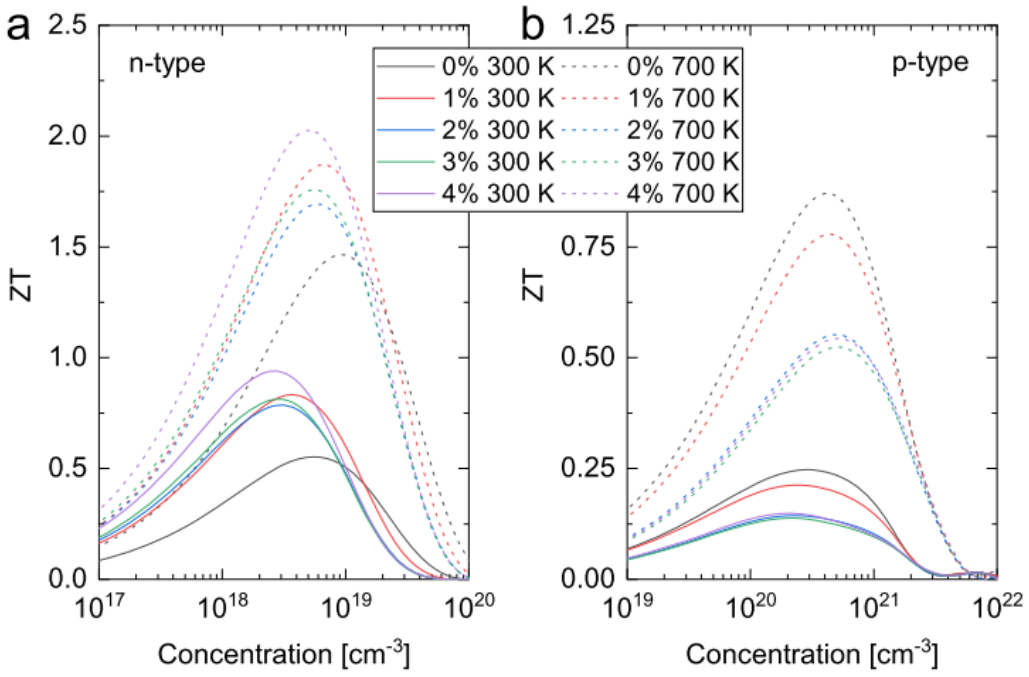

Figure 5.18: Concentration dependence of the zT for (a) n- and (b) p-type α-Te under different tensile strains at 300 and 700 K, respectively.

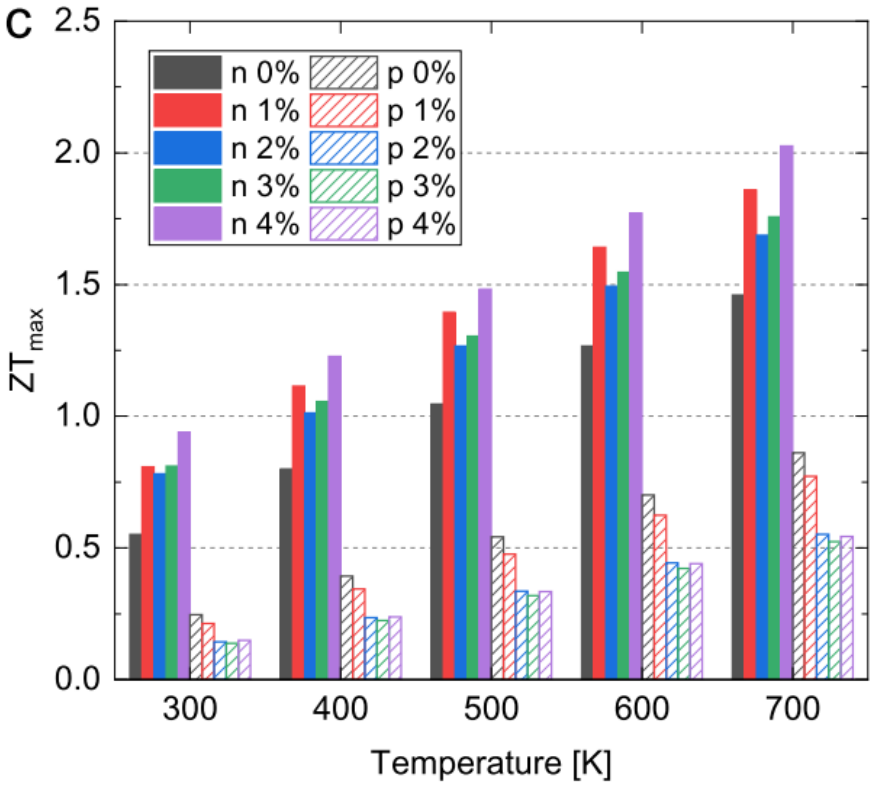

Figure 5.19: Maximum zT under different tensile strains for n- and p-type *alpha*-Te at different temperatures.

Chapter 6

Conclusions and Future Work

In this dissertation, we presented our home-developed algorithms based on Boltzmann transport equation in conjunction with electron-phonon interactions for calculating the electrical transport properties, such as electrical conductivity, electrical thermal conductivity, Seebeck coefficient. Our scheme combined with the available methods for phonon transport properties (*aka* lattice thermal conductivity) can provide a complete description of the thermoelectric figure of merit.

When examining the correctness of our methodology, the calculated mobilities for both n-type and p-type 3C-SiC are consistent with the experimental data. In addition, it is interesting to find a temperature scattering mechanism for both types of charge carriers. At room temperature, the scattering is dominated by the longitudinal acoustic (LA) phonons. However, at elevated temperature, the polar longitudinal optical (LO) phonons become dominant. This is because of the high frequency of the LO phonons, which are less populated at room temperature.

We found that the anisotropy of the effective mass is greatly related to the anisotropic electrical conductivity and electrical thermal conductivity in the study of Mg_3Sb_2 in Chapter 4. Strong anisotropic electrical conductivity and electrical thermal

conductivity were observed in p-type Mg_3Sb_2, whereas they are nearly isotropic in the n-type counterpart. Seebeck coefficient and lattice thermal conductivity tend to be nearly isotropic in both types. Therefore, strong anisotropic thermoelectric properties were found for p-type Mg_3Sb_2. And it is interesting to note the thermoelectric figure of merit along the out-of-plane direction is above unity, indicating that the p-type performance might be improved experimentally.

Our methodology can also be used for calculating the thermoelectric properties of two-dimensional materials. In Chapter 5, ultrahigh electron mobility is obtained for α-Te. However, the hole mobility is two orders of magnitude smaller. In addition, it is noticeable that the lattice thermal conductivity of α-Te is lower than many previously reported two-dimensional materials due to its low phonon frequency and short phonon lifetime. Above room temperature, the lattice thermal conductivity is lower than 4.2 $Wm^{-1}K^{-1}$. As a result, two-dimensional α-Te exhibits excellent thermoelectric performance; the zT value reaches 1.46 and 0.86 at 700 K for pristine n- and p-type systems, respectively. Besides, even small tensile strain (up to 4%) can significantly enhance the zT of an n-type system mainly due to strain-induced linear dispersion of ZA modes and the resulting suppressed carrier scattering by ZA modes. The peak zT values are enhanced to 0.94 and 2.03 by a 4% tensile strain at 300 and 700 K, respectively. By contrast, strain degrades the thermoelectric performance of p-type monolayer α-Te.

The recent development on the thermoelectric properties of Dirac/Weyl nodal semimetal brings in a new viewpoint for the thermoelectric materials. [224, 225, 226, 227, 228, 228] For example, the maximum zT of Cd_3As_2 could achieve 1.24 at 450 K under magnetic field of 9 T, which is order of magnitude higher than the data obtained with the absence of magnetic field. [225] However, compared to the fast development of the experimental techniques, the theoretical approaches are being developed at a

slower pace. [229, 230] Most importantly, all the theoretical/computational research did not consider the electron-phonon interaction, which is the main source of scattering especially at temperature well above the Debye temperature of the material. Therefore, the thermoelectric transport properties of Dirac/Weyl nodal semimetal still warrant further studies from the theoretical/computational viewpoint. In future work, the effects from magnetic field need to be considered in the algorithms, in which the magnetic field would be an adjustable parameter so that we would be able to calculate the thermoelectric properties under magnetic field directly from first principles, which can provide fruitful physical insights of the detailed thermoelectric transport mechanism under magnetic field.

Appendices

Appendix A Phonon-Isotope Scattering

In single crystals, besides from phonon-phonon interactions, phonons can also be scattered by isotopes. [57] The phonon-isotope scattering rate can be calculated with [231, 232]

$$\Gamma_{\lambda\lambda'} = \frac{\pi\omega^2}{2} \sum_{i \in u.c.} g(i) |\mathbf{e}_{\lambda}^{*}(i) \mathbf{e}_{\lambda'}(i)|^2 \delta(\omega_{\lambda} - \omega_{\lambda'}) \tag{A.1}$$

where λ denote the phonon index with q point and p branch. In Equation A.1, the $g(i)$ is the Pearson deviation coefficient for each atom in the primitive unit cell, and can be obtained as:

$$g(i) = \sum_{s} f_s(i)[1 - M_s(i)/\bar{M}(i)]^2 \tag{A.2}$$

where f_s is the relative frequency with $0 < f_x \leq 1$, $M_s(i)$ represent the mass of isotope s for the element corresponding to atom i and their average $\bar{M}(i)$ is given by:

$$\bar{M}(i) = \sum_{s} f_s M_s(i). \tag{A.3}$$

Appendix B Charged Impurity Scattering in Magnesium Antimonide

Mg_3Sb_2 is known to have native defects, including Mg vacancies [146]. Meanwhile, in order to tune the carrier concentration, defects are introduced externally. We used the Brooks-Herring model [169, 170] to simulate the influence of the charged impurity on the electronically related transport properties, such as the electrical conductivity, the electrical thermal conductivity and the Seebeck coefficient.

According to the Brooks-Herring model, the scattering rate from charged impurity is given by:

$$\tau_{m\mathbf{k}\to m'\mathbf{k}+\mathbf{q}} = \frac{2\pi Z^2 n_i e^4}{\hbar V \left(\epsilon_r \epsilon_0\right)^2} \frac{\delta\left(\epsilon_{m'\mathbf{k}+\mathbf{q}} - \epsilon_{m\mathbf{k}}\right)}{\left(q_{scr}^2 + |\mathbf{q}|^2\right)^2} \tag{B.1}$$

where V is the unit cell volume, q_{scr} is the screening wave vector, ϵ_r and ϵ_0 are the relative and the vacuum permittivity. Ze is the charge of the impurity, where Z is taken to be unity in the calculations; n_i is the impurity density, which is set equal to the carrier concentration, thus assuming full ionization.

As shown in Figure B.1 and B.2, both electrical conductivity and electrical thermal conductivity decrease slightly, but the anisotropy is almost unaffected in the presence of such defects. Meanwhile, the impacts of the point defects on the Seebeck coefficient and the anisotropy of the Seebeck coefficient are trivial according to our calculations (Figure B.3). Finally, the zT value is slightly influenced by the defects (Figure B.4). For n-type Mg_3Sb_2, the highest calculated zT including defect scattering is around 2.0 at 750 K. For p-type Mg3Sb2, the highest calculated zT including defect scattering is 0.57 along a(b)-axis and 1.42 along c-axis at 750 K, respectively.

To understand why the charged impurity contributes negligibly to the elec-

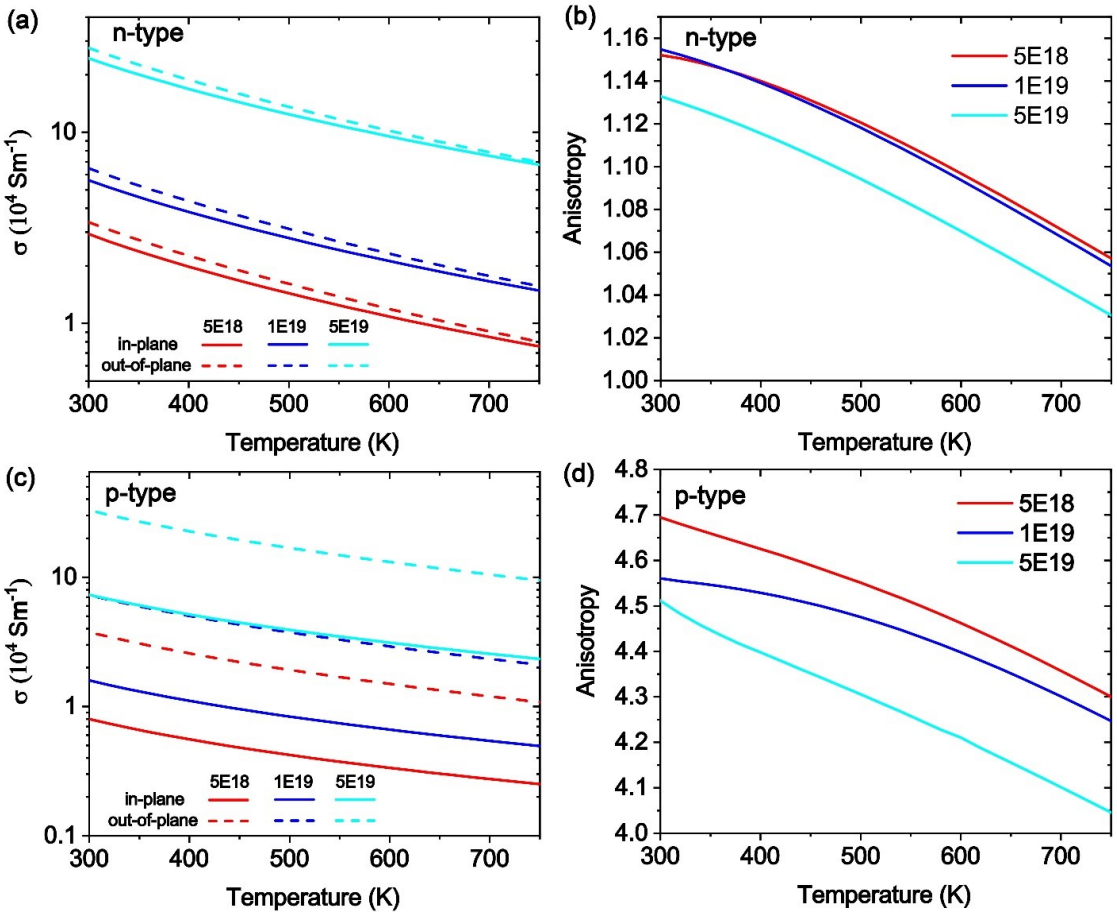

Figure B.1: Temperature dependent (a) n-type and (c) p-type electrical conductivity obtained with point-defect scattering included. Corresponding temperature dependent anisotropy (σ^c/σ^a) for (b) n-type and (d) p-type Mg_3Sb_2.

tronically related transport properties, especially the electrical conductivity and the electrical thermal conductivity, the scattering rates of electron-phonon interactions and impurity scattering are compared in Figure B.5 for both conduction types. As can be seen, the scattering rates of electron-phonon interactions are much larger than those arising from charged impurity scattering processes; meanwhile, in some other semiconductors, taking silicon for an example, the scattering rates from a charged impurity are comparable, or even higher, than the scattering rates due to electron-phonon interactions. [77, 199]

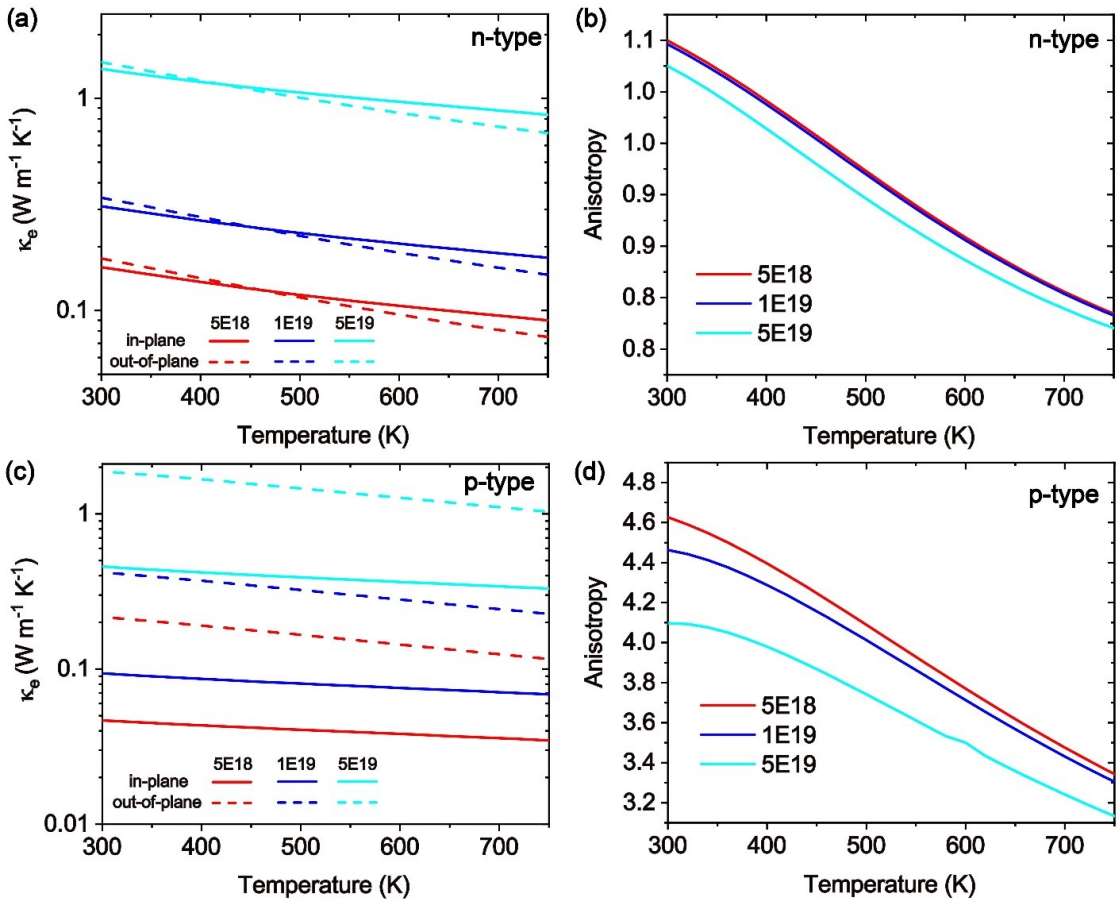

Figure B.2: Temperature dependent (a) n-type and (c) p-type electrical thermal conductivity obtained with point-defect scattering included. Corresponding temperature dependent anisotropy (κ_e^c/κ_e^a) for (b) n-type and (d) p-type Mg_3Sb_2.

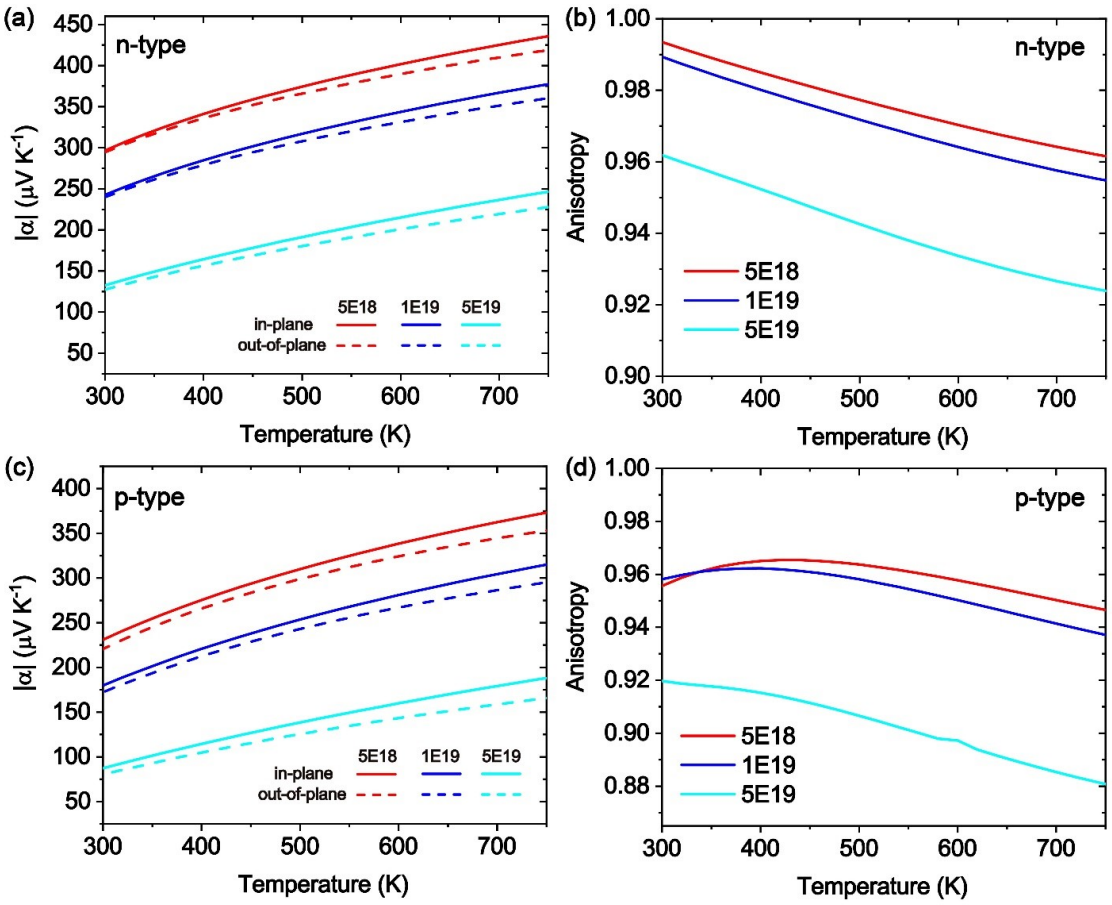

Figure B.3: Temperature dependent (a) n-type and (c) p-type Seebeck coefficient obtained with point-defect scattering included. Corresponding temperature dependent anisotropy (α^c/α^a) for (b) n-type and (d) p-type Mg_3Sb_2.

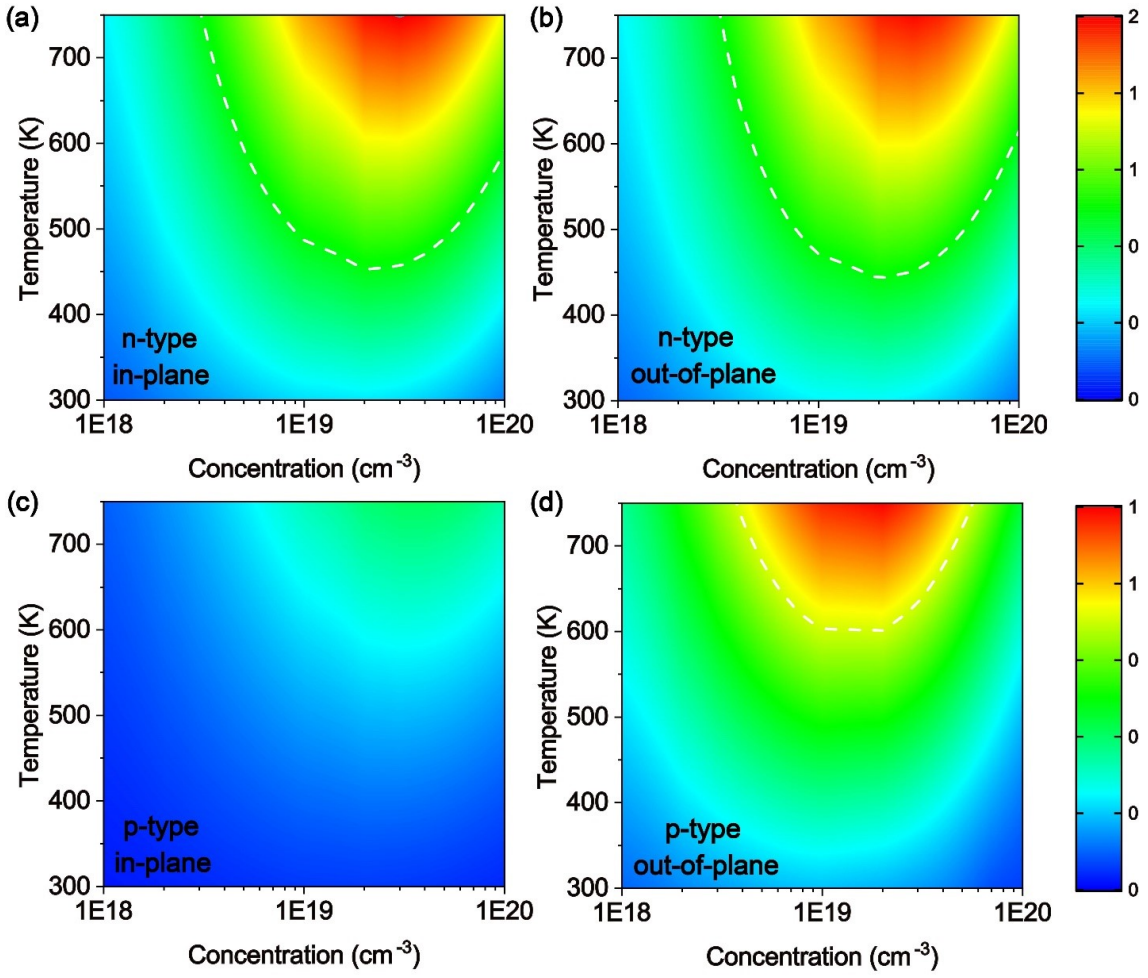

Figure B.4: Contour map of zT with point defect scattering included as a function of both temperature and carrier concentration for Mg_3Sb_2: (a) n-type along the in-plane direction, (b) n-type along the out-of-plane direction, (c) p-type along the in-plane direction and (d) p-type along the out-of-plane direction. (a) and (b) share the same color bar, while (c) and (d) share the same color bar. The white dashed line corresponds to zT equaling to 1.0.

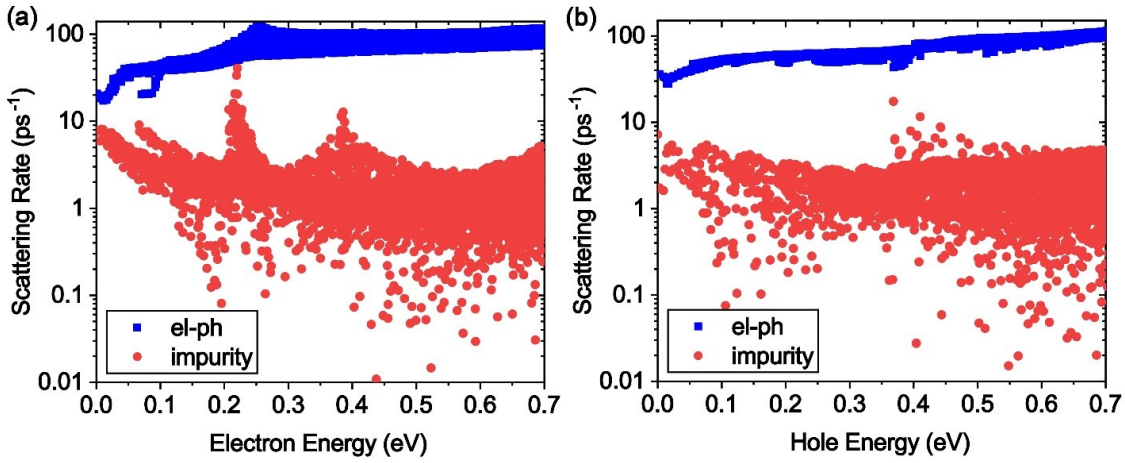

Figure B.5: Comparison between room temperature electron-phonon interaction scattering rates and electron-impurity interaction scattering rates in (a) n-type and (b) p-type Mg_3Sb_2 at carrier concentration 10^{19} cm^{-3}.

Appendix C Convergence Check for Lattice Thermal Conductivity for Two Dimensional alpha-Tellurium

The first principles calculation of lattice thermal conductivity using ShengBTE package [58] requires several convergence checks. In convention, a truncating cutoff is implemented in the calculations of third-order anharmonic interatomic force constants (IFCs). We have checked that a cutoff distance of 0.6 nm, used in our work, can achieve reasonable convergence. As shown in Figure C.1(a), if the cutoff is not large enough, the lattice thermal conductivity would be overestimated.

When applying ShengBTE package to solve BTE, there are two more parameters affecting the convergence, namely, *ngrids* and *scalebroad*. The ngrids denotes the q meshes of Brillouin zone, whereas the scalebroad controls the energy conservation process. We first used a safely large $scalebroad = 1$ to check the convergence with respect to q grids, and found that the lattice thermal conductivity is easily converged, as shown in Figure C.1(b). Then, using large q grids, we checked the convergence with respect to the *scalebroad*. As a routine, one uses a small *scalebroad* to reduce the processes that need to be considered to save the computational cost. However, we found that the *scalebroad* should be larger than 0.1, otherwise small *scalebroad* would overestimate the lattice thermal conductivity, as shown in Figure C.1(c).

To have a deeper understanding of the overestimation caused by a small *scalebroad* value, here we calculated the frequency-dependent contribution to the lattice thermal conductivity, as what was done in the work of Gao *et al.* [195]. As shown in Figure S4, it is found that the overestimation mainly comes from the non-convergent low-frequency phonons. With a small scalebroad, we reproduced the low-frequency

peak reported in the work of Gao *et al.* [195] However, using convergent scalebroad, the peak is gone, and the distribution lines converge very well.

Therefore, in this work, we use a cutoff of 0.6 nm for the calculation of third order IFCs, and in solving BTE, we use 200×200×1 q grids with *scalebroad*=1.

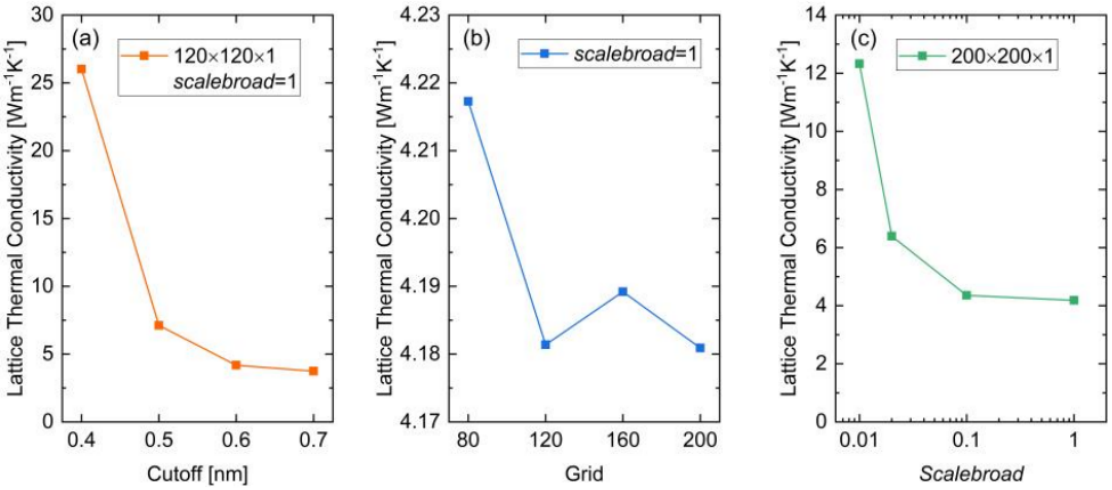

Figure C.1: Convergence of lattice thermal conductivity with respect to (a) the cutoff distance for third-order IFCs, (b) the q grids, and (c) the *scalebroad*, at room temperature.

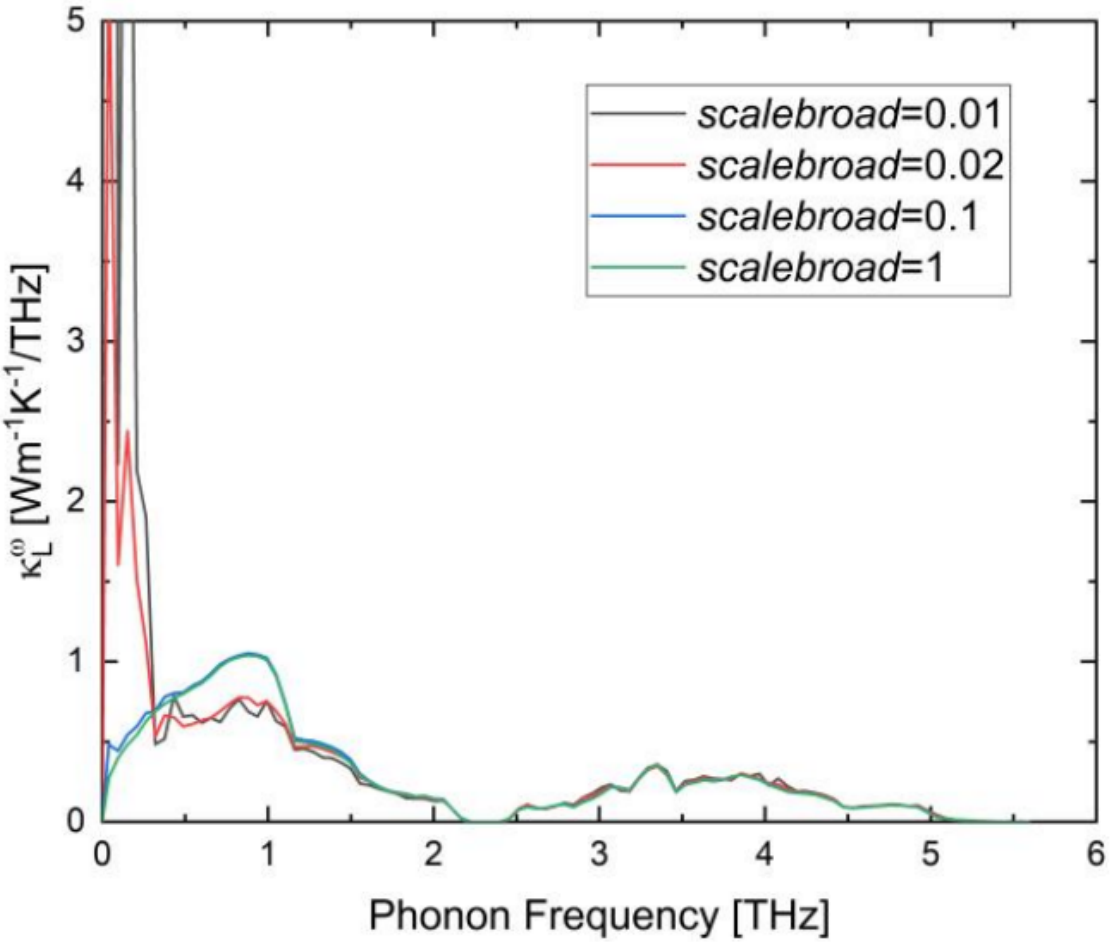

Figure C.2: Contribution to the lattice thermal conductivity from different frequencies at room temperature with different *scalebroad* parameters.

Appendix D Tensile Strain Effect on Thermoelectric Properties Two Dimensional alpha-Tellurium

The tensile strain effect on Seebeck coefficient, electrical conductivity, electronic thermal conductivity, and power factor for n- and p-type α-Te are given in Figures D.1 and D.2, respectively. Overall, the Seebeck coefficient is weakly affected by tensile strain in both n-type and p-type systems. The electrical conductivity, electronic thermal conductivity, and power factor in n-type system first increase obviously when the strain changes from 0 to 2% and then remain almost unchanged as strain increases from 2% to 4%, whereas these properties are decreased in p-type system with strain changing from 0 to 4%, which is consistent with the changing trends of mobilities.

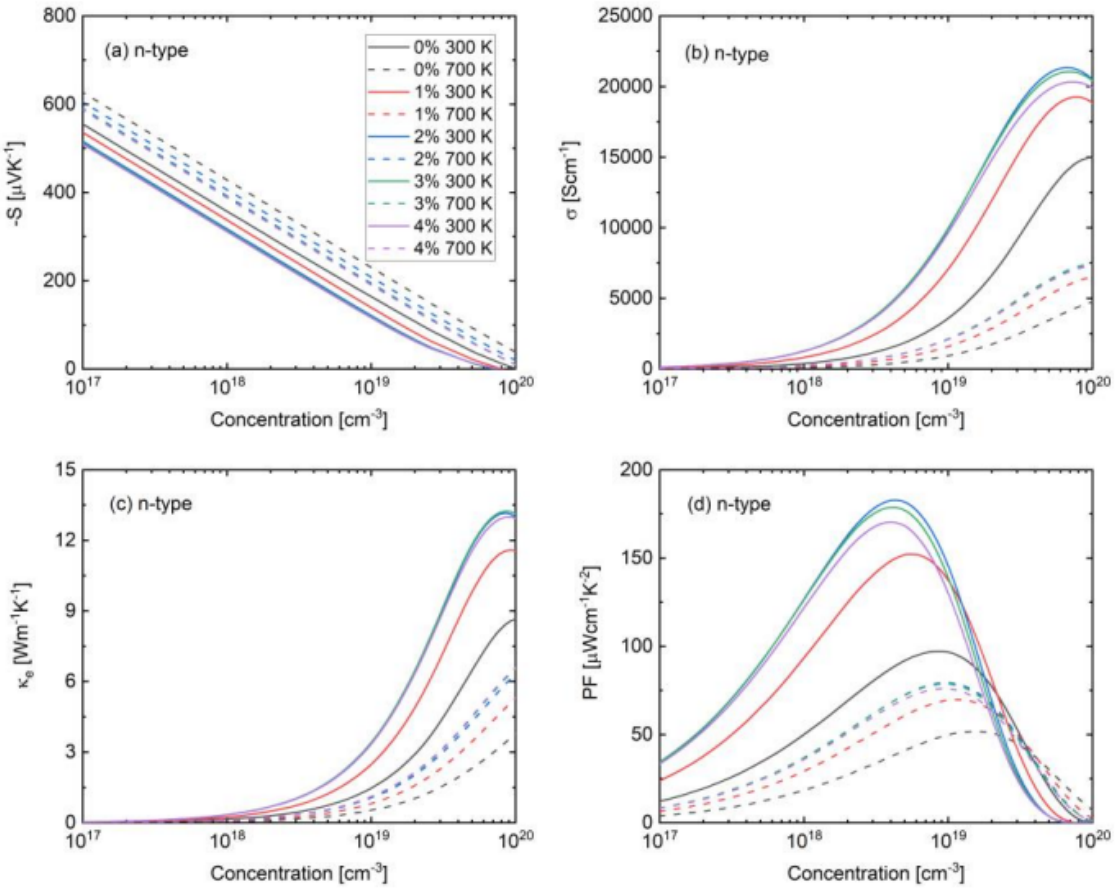

Figure D.1: (a) Seebeck coefficient, (b) electrical conductivity, (c) electronic thermal conductivity, and (d) power factor of n-type α-Te under different tensile strains at 300 K and 700 K.

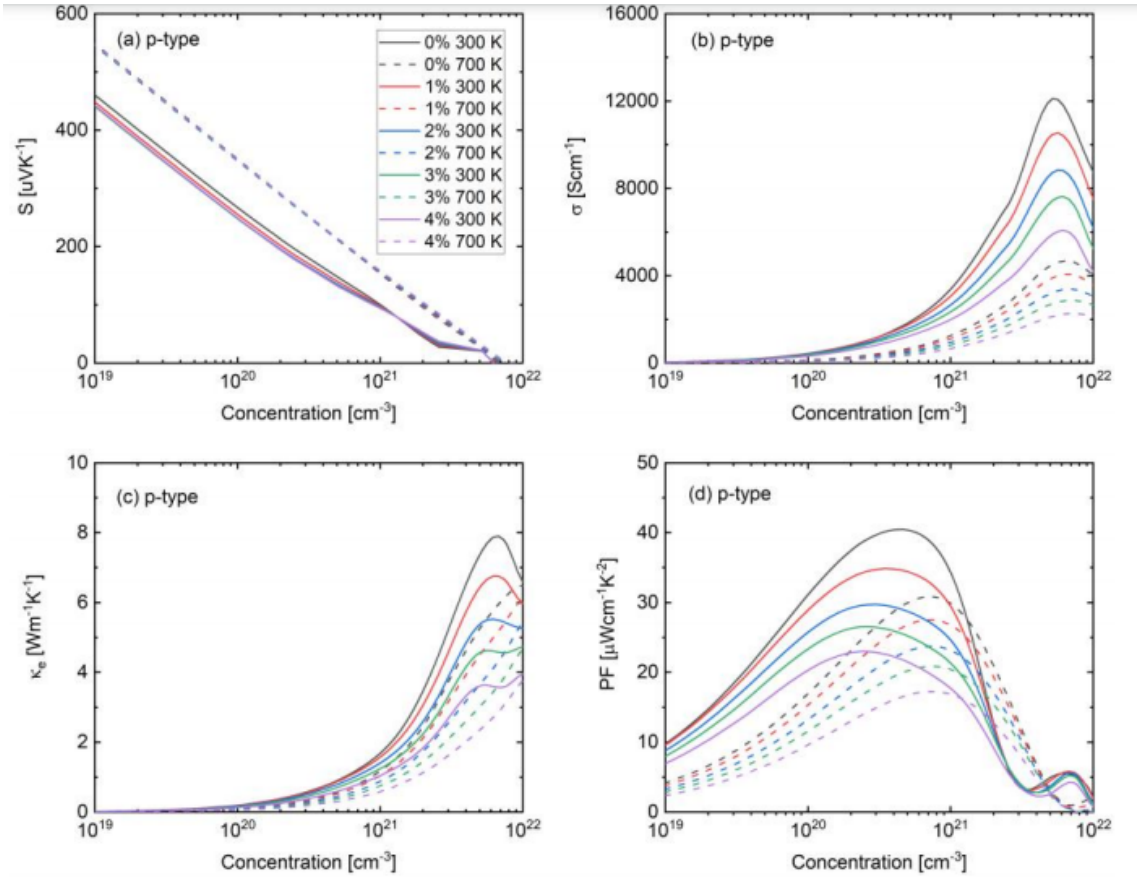

Figure D.2: (a) Seebeck coefficient, (b) electrical conductivity, (c) electronic thermal conductivity, and (d) power factor of p-type α-Te under different tensile strains at 300 K and 700 K.

Appendix E Thermoelectric ZT with Closed-circuit Electrical Thermal Conductivity of Two Dimensional alpha-Tellurium

The main difference for electrical thermal conductivity in the open circuit and the closed circuit is: electrons are driven by both electrochemical potential gradient and temperature gradient in a closed circuit, whereas electrons are driven by temperature gradient in an open circuit. In this thesis, the electronic thermal conductivity is calculated in the open-circuit case, expressed as [233]:

$$\kappa_e = \frac{s}{TVN_k} \sum_{n\mathbf{k}} \left(\varepsilon_{n\mathbf{k}} - \varepsilon_f\right)^2 \mathbf{v}_{n\mathbf{k}} \mathbf{F}_{n\mathbf{k}} \left(-\frac{\partial f^0_{n\mathbf{k}}}{\partial \varepsilon_{n\mathbf{k}}}\right) - T\sigma\mathbf{S}^2 \tag{E.1}$$

The second term $T\sigma\mathbf{S}^2$ on the right-hand side, with a minus sign, is the electrochemical potential gradient contribution. Removing the $T\sigma\mathbf{S}^2$ term, the formula is reduced to the closed-circuit case [233]. Therefore, the electronic thermal conductivity in open-circuit case is smaller than that of closed-circuit case, leading to higher calculated ZT. From Figure E.1, it is found that the ZT calculated with closed-circuit electronic thermal conductivity is indeed smaller than that of open-circuit case.

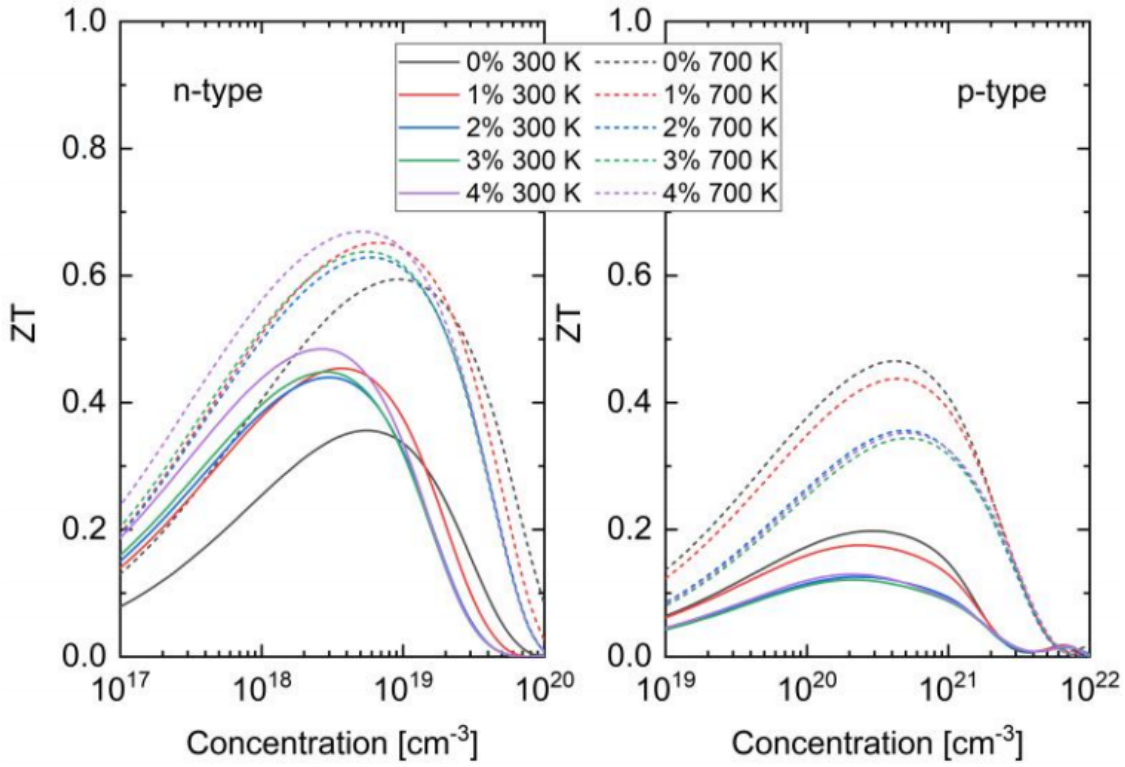

Figure E.1: Calculated ZT with closed-circuit electronic thermal conductivity for (a) and (b) p-type α-Te under different strains at 300 K and 700 K.

Bibliography

[1] Timothy D. Sands. Designing nanocomposite thermoelectric materials, https://nanohub.org/resources/383, Nov 2005.

[2] Safa O Kasap. *Principles of electronic materials and devices*. McGraw-Hill, 2006.

[3] Jing-Feng Li, Wei-Shu Liu, Li-Dong Zhao, and Min Zhou. High-performance nanostructured thermoelectric materials. *NPG Asia Materials*, 2(4):152–158, 2010.

[4] Cheryl Sturm, Parisa Jafarzadeh, and Holger Kleinke. 1.17 thermoelectric nanomaterials. *Comprehensive Nanoscience and Nanotechnology*, page 349, 2019.

[5] http://thermoelectrics.matsci.northwestern.edu/thermoelectrics/.

[6] Yanzhong Pei, Xiaoya Shi, Aaron LaLonde, Heng Wang, Lidong Chen, and G Jeffrey Snyder. Convergence of electronic bands for high performance bulk thermoelectrics. *Nature*, 473(7345):66–69, 2011.

[7] J Serrano, J Strempfer, M Cardona, M Schwoerer-Böhning, H Requardt, M Lorenzen, B Stojetz, P Pavone, and WJ Choyke. Determination of the phonon dispersion of zinc blende (3C) silicon carbide by inelastic x-ray scattering. *Applied physics letters*, 80(23):4360–4362, 2002.

[8] F Widulle, T Ruf, O Buresch, A Debernardi, and M Cardona. Raman study of isotope effects and phonon eigenvectors in SiC. *Physical review letters*, 82(15):3089, 1999.

[9] WE Nelson, FA Halden, and A Rosengreen. Growth and properties of β-sic single crystals. *Journal of Applied Physics*, 37(1):333–336, 1966.

[10] Mikiya Shinohara, Mitsugu Yamanaka, Hiroshi Daimon, Eiichiro Sakuma, Hajime Okumura, Shunji Misawa, Kazuhiro Endo, and Sadafumi Yoshida. Growth of high-mobility 3C-SiC epilayers by chemical vapor deposition. *Japanese journal of applied physics*, 27(3A):L434, 1988.

[11] AA Lebedev, PL Abramov, EV Bogdanova, SP Lebedev, DK Nel'son, GA Oganesyan, AS Tregubova, and Rositsa Yakimova. Highly doped p-type 3C-SiC on 6H-SiC substrates. *Semiconductor Science and Technology*, 23(7):075004, 2008.

[12] Soohyun Kim, Chungman Kim, Yang-Ki Hong, Takahiro Onimaru, Koichiro Suekuni, Toshiro Takabatake, and Myung-Hwa Jung. Thermoelectric properties of Mn-doped Mg-Sb single crystals. *Journal of Materials Chemistry A*, 2(31):12311–12316, 2014.

[13] Soo Hyun Kim, Chung Man Kim, Yang-Ki Hong, Kyung Ik Sim, Jae Hoon Kim, Takahiro Onimaru, Toshiro Takabatake, and Myung-Hwa Jung. Thermoelectric properties of $Mg_3Sb_{2-x}Bi_x$ single crystals grown by Bridgman method. *Materials Research Express*, 2(5):055903, 2015.

[14] Jiazhan Xin, Guowei Li, Gudrun Auffermann, Horst Borrmann, Walter Schnelle, Johannes Gooth, Xinbing Zhao, Tiejun Zhu, Claudia Felser, and Chenguang Fu. Growth and transport properties of Mg_3X_2 (X= Sb, Bi) single crystals. *Materials Today Physics*, 7:61–68, 2018.

[15] Lirong Song, Jiawei Zhang, and Bo B Iversen. Simultaneous improvement of power factor and thermal conductivity via Ag doping in p-type Mg_3Sb_2 thermoelectric materials. *Journal of Materials Chemistry a*, 5(10):4932–4939, 2017.

[16] A Bhardwaj, NS Chauhan, and DK Misra. Significantly enhanced thermoelectric figure of merit of p-type Mg_3Sb_2-based Zintl phase compounds via nanostructuring and employing high energy mechanical milling coupled with spark plasma sintering. *Journal of Materials Chemistry A*, 3(20):10777–10786, 2015.

[17] Shan Huang, Ziyu Wang, Rui Xiong, Hongyu Yu, and Jing Shi. Significant enhancement in thermoelectric performance of Mg_3Sb_2 from bulk to two-dimensional mono layer. *Nano Energy*, 62:212–219, 2019.

[18] Jiawei Zhang, Lirong Song, Mattia Sist, Kasper Tolborg, and Bo Brummerstedt Iversen. Chemical bonding origin of the unexpected isotropic physical properties in thermoelectric Mg_3Sb_2 and related materials. *Nature communications*, 9(1):1–10, 2018.

[19] Jiawei Zhang, Lirong Song, Steffen Hindborg Pedersen, Hao Yin, Bo Brummerstedt Iversen, et al. Discovery of high-performance low-cost n-type Mg_3Sb_2-based thermoelectric materials with multi-valley conduction bands. *Nature communications*, 8(1):1–8, 2017.

[20] Jiawei Zhang, Lirong Song, Aref Mamakhel, Mads Ry Vogel Jørgensen, and Bo Brummerstedt Iversen. High-performance low-cost n-type Se-doped Mg_3Sb_2-based Zintl compounds for thermoelectric application. *Chemistry of Materials*, 29(12):5371–5383, 2017.

[21] Hiromasa Tamaki, Hiroki K Sato, and Tsutomu Kanno. Isotropic conduction network and defect chemistry in $Mg_{3+\delta}Sb_2$-based layered Zintl compounds with high thermoelectric performance. *Advanced Materials*, 28(46):10182–10187, 2016.

[22] Jun Mao, Yixuan Wu, Shaowei Song, Qing Zhu, Jing Shuai, Zihang Liu, Yanzhong Pei, and Zhifeng Ren. Defect engineering for realizing high thermoelectric performance in n-type Mg_3Sb_2-based materials. *ACS Energy Letters*, 2(10):2245–2250, 2017.

[23] Jing Shuai, Yumei Wang, Hee Seok Kim, Zihang Liu, Jingying Sun, Shuo Chen, Jiehe Sui, and Zhifeng Ren. Thermoelectric properties of Na-doped Zintl compound: $Mg_{3-x}Na_xSb_2$. *Acta Materialia*, 93:187–193, 2015.

[24] Chen Chen, Xiaofang Li, Shan Li, Xinyu Wang, Zongwei Zhang, Jiehe Sui, Feng Cao, Xingjun Liu, and Qian Zhang. Enhanced thermoelectric performance of p-type Mg_3Sb_2 by lithium doping and its tunability in an anionic framework. *Journal of Materials Science*, 53(23):16001–16009, 2018.

[25] Hao Wang, Jin Chen, Tianqi Lu, Kunjie Zhu, Shan Li, Jun Liu, and Huaizhou Zhao. Enhanced thermoelectric performance in p-type Mg_3Sb_2 via lithium doping. *Chinese Physics B*, 27(4):047212, 2018.

[26] Xiaodan Tang, Bin Zhang, Xiao Zhang, Shuxia Wang, Xu Lu, Guang Han, Guoyu Wang, and Xiaoyuan Zhou. Enhancing the thermoelectric performance of p-type Mg_3Sb_2 via codoping of Li and Cd. *ACS Applied Materials & Interfaces*, 12(7):8359–8365, 2020.

[27] Jun Mao, Jing Shuai, Shaowei Song, Yixuan Wu, Rebecca Dally, Jiawei Zhou, Zihang Liu, Jifeng Sun, Qinyong Zhang, Clarina Dela Cruz, et al. Manipulation of ionized impurity scattering for achieving high thermoelectric performance in n-type Mg_3Sb_2-based materials. *Proceedings of the National Academy of Sciences*, 114(40):10548–10553, 2017.

[28] Kazuki Imasato, Max Wood, Jimmy Jiahong Kuo, and G Jeffrey Snyder. Improved stability and high thermoelectric performance through cation site doping in n-type La-doped $Mg_3Sb_{1.5}Bi_{0.5}$. *Journal of Materials Chemistry A*, 6(41):19941–19946, 2018.

[29] Xuemin Shi, Tingting Zhao, Xinyue Zhang, Cheng Sun, Zhiwei Chen, Siqi Lin, Wen Li, Hui Gu, and Yanzhong Pei. Extraordinary n-type Mg_3SbBi thermoelectrics enabled by yttrium doping. *Advanced Materials*, 31(36):1903387, 2019.

[30] Tsutomu Kanno, Hiromasa Tamaki, Hiroki K Sato, Stephen Dongmin Kang, Saneyuki Ohno, Kazuki Imasato, Jimmy Jiahong Kuo, G Jeffrey Snyder, and Yuzuru Miyazaki. Enhancement of average thermoelectric figure of merit by increasing the grain-size of $Mg_{3.2}Sb_{1.5}Bi_{0.49}Te_{0.01}$. *Applied Physics Letters*, 112(3):033903, 2018.

[31] TJ Seebeck. The magnetic polarization of metals and ores produced by temperature difference. *Proceedings. of Prussian Academy of Sciences*, pages 265–373, 1822.

[32] JCA Peltier. New experiments on the heat effects of electric currents (in French). *Ann. Chim. Phys*, 56:371–386, 1834.

[33] H Julian Goldsmid. The Seebeck and Peltier effects. *The Physics of Thermoelectric Energy Conversion*, pages 2053–2571, 2017.

[34] Jae Sung Lee and Hyunggyu Park. Carnot efficiency is reachable in an irreversible process. *Scientific reports*, 7(1):1–9, 2017.

[35] G Jeffrey Snyder and Eric S Toberer. Complex thermoelectric materials. In *Materials for sustainable energy: a collection of peer-reviewed research and review articles from Nature Publishing Group*, pages 101–110. World Scientific, 2011.

[36] Tiejun Zhu, Lipeng Hu, Xinbing Zhao, and Jian He. New insights into intrinsic point defects in V_2VI_3 thermoelectric materials. *Advanced Science*, 3(7):1600004, 2016.

[37] Lei Yang, Zhi-Gang Chen, Matthew S Dargusch, and Jin Zou. High performance thermoelectric materials: progress and their applications. *Advanced Energy Materials*, 8(6):1701797, 2018.

[38] Tiejun Zhu, Yintu Liu, Chenguang Fu, Joseph P Heremans, Jeffrey G Snyder, and Xinbing Zhao. Compromise and synergy in high-efficiency thermoelectric materials. *Advanced materials*, 29(14):1605884, 2017.

[39] Min Hong, Wanyu Lyv, Meng Li, Shengduo Xu, Qiang Sun, Jin Zou, and Zhi-Gang Chen. Rashba effect maximizes thermoelectric performance of GeTe derivatives. *Joule*, 4(9):2030–2043, 2020.

[40] Min Hong, Zhi-Gang Chen, Lei Yang, Yi-Chao Zou, Matthew S Dargusch, Hao Wang, and Jin Zou. Realizing zT of 2.3 in $Ge_{1-x-y}Sb_xIn_yTe$ via reducing the phase-transition temperature and introducing resonant energy doping. *Advanced materials*, 30(11):1705942, 2018.

[41] Joseph P Heremans, Bartlomiej Wiendlocha, and Audrey M Chamoire. Resonant levels in bulk thermoelectric semiconductors. *Energy & Environmental Science*, 5(2):5510–5530, 2012.

[42] Joseph P Heremans, Vladimir Jovovic, Eric S Toberer, Ali Saramat, Ken Kurosaki, Anek Charoenphakdee, Shinsuke Yamanaka, and G Jeffrey Snyder. Enhancement of thermoelectric efficiency in PbTe by distortion of the electronic density of states. *Science*, 321(5888):554–557, 2008.

[43] Qinyong Zhang, Hui Wang, Weishu Liu, Hengzhi Wang, Bo Yu, Qian Zhang, Zhiting Tian, George Ni, Sangyeop Lee, Keivan Esfarjani, et al. Enhancement of thermoelectric figure-of-merit by resonant states of aluminium doping in lead selenide. *Energy & Environmental Science*, 5(1):5246–5251, 2012.

[44] Qian Zhang, Bolin Liao, Yucheng Lan, Kevin Lukas, Weishu Liu, Keivan Esfarjani, Cyril Opeil, David Broido, Gang Chen, and Zhifeng Ren. High thermoelectric performance by resonant dopant indium in nanostructured SnTe. *Proceedings of the National Academy of Sciences*, 110(33):13261–13266, 2013.

[45] Gangjian Tan, Li-Dong Zhao, and Mercouri G Kanatzidis. Rationally designing high-performance bulk thermoelectric materials. *Chemical reviews*, 116(19):12123–12149, 2016.

[46] Yufei Liu, Menghan Zhou, and Jian He. Towards higher thermoelectric performance of Bi_2Te_3 via defect engineering. *Scripta Materialia*, 111:39–43, 2016.

[47] Wei Wei, Cheng Chang, Teng Yang, Jizi Liu, Huaichao Tang, Jian Zhang, Yusheng Li, Feng Xu, Zhidong Zhang, Jing-Feng Li, et al. Achieving high thermoelectric figure of merit in polycrystalline SnSe via introducing Sn vacancies. *Journal of the American Chemical Society*, 140(1):499–505, 2018.

[48] Wen Li, Siqi Lin, Xinyue Zhang, Zhiwei Chen, Xiangfan Xu, and Yanzhong Pei. Thermoelectric properties of Cu_2SnSe_4 with intrinsic vacancy. *Chemistry of Materials*, 28(17):6227–6232, 2016.

[49] Juan Li, Xinyue Zhang, Siqi Lin, Zhiwei Chen, and Yanzhong Pei. Realizing the high thermoelectric performance of GeTe by Sb-doping and Se-alloying. *Chemistry of Materials*, 29(2):605–611, 2017.

[50] Jing Tang, Bo Gao, Siqi Lin, Xiao Wang, Xinyue Zhang, Fen Xiong, Wen Li, Yue Chen, and Yanzhong Pei. Manipulation of solubility and interstitial defects for improving thermoelectric SnTe alloys. *ACS Energy Letters*, 3(8):1969–1974, 2018.

[51] Kanishka Biswas, Jiaqing He, Ivan D Blum, Chun-I Wu, Timothy P Hogan, David N Seidman, Vinayak P Dravid, and Mercouri G Kanatzidis. High-performance bulk thermoelectrics with all-scale hierarchical architectures. *Nature*, 489(7416):414–418, 2012.

[52] Li-Dong Zhao, Shih-Han Lo, Yongsheng Zhang, Hui Sun, Gangjian Tan, Ctirad Uher, Christopher Wolverton, Vinayak P Dravid, and Mercouri G Kanatzidis. Ultralow thermal conductivity and high thermoelectric figure of merit in SnSe crystals. *Nature*, 508(7496):373–377, 2014.

[53] Wen Li, Siqi Lin, Manuel Weiss, Zhiwei Chen, Juan Li, Yidong Xu, Wolfgang G Zeier, and Yanzhong Pei. Crystal structure induced ultralow lattice thermal conductivity in thermoelectric Ag_9AlSe_6. *Advanced Energy Materials*, 8(18):1800030, 2018.

[54] Xiaolei Shi, Angyin Wu, Weidi Liu, Raza Moshwan, Yuan Wang, Zhi-Gang Chen, and Jin Zou. Polycrystalline SnSe with extraordinary thermoelectric property via nanoporous design. *ACS nano*, 12(11):11417–11425, 2018.

[55] Weidi Liu, Xiaolei Shi, Raza Moshwan, Min Hong, Lei Yang, Zhi-Gang Chen, and Jin Zou. Enhancing thermoelectric performance of $(Cu_{1-x}Ag_x)_2Se$ via CuAgSe secondary phase and porous design. *Sustainable Materials and Technologies*, 17:e00076, 2018.

[56] Siqi Lin, Wen Li, Shasha Li, Xinyue Zhang, Zhiwei Chen, Yidong Xu, Yue Chen, and Yanzhong Pei. High thermoelectric performance of Ag_9GaSe_6 enabled by low cutoff frequency of acoustic phonons. *Joule*, 1(4):816–830, 2017.

[57] John M Ziman. *Electrons and phonons: the theory of transport phenomena in solids*. Oxford university press, 2001.

[58] Wu Li, Jesús Carrete, Nebil A Katcho, and Natalio Mingo. ShengBTE: A solver of the Boltzmann transport equation for phonons. *Computer Physics Communications*, 185(6):1747–1758, 2014.

[59] DA Broido, A Ward, and N Mingo. Lattice thermal conductivity of silicon from empirical interatomic potentials. *Physical Review B*, 72(1):014308, 2005.

[60] Aleksandr Chernatynskiy and Simon R Phillpot. Evaluation of computational techniques for solving the boltzmann transport equation for lattice thermal conductivity calculations. *Physical Review B*, 82(13):134301, 2010.

[61] David A Broido, Michael Malorny, Gerd Birner, Natalio Mingo, and DA Stewart. Intrinsic lattice thermal conductivity of semiconductors from first principles. *Applied Physics Letters*, 91(23):231922, 2007.

[62] Alistair Ward, DA Broido, Derek A Stewart, and Gernot Deinzer. Ab initio theory of the lattice thermal conductivity in diamond. *Physical Review B*, 80(12):125203, 2009.

[63] DA Broido, L Lindsay, and A Ward. Thermal conductivity of diamond under extreme pressure: A first-principles study. *Physical Review B*, 86(11):115203, 2012.

[64] L Lindsay, DA Broido, and TL Reinecke. Thermal conductivity and large isotope effect in GaN from first principles. *Physical review letters*, 109(9):095901, 2012.

[65] Wu Li, Lucas Lindsay, David A Broido, Derek A Stewart, and Natalio Mingo. Thermal conductivity of bulk and nanowire $Mg_2Si_xSn_{1-x}$ alloys from first principles. *Physical Review B*, 86(17):174307, 2012.

[66] John Bardeen, Leon N Cooper, and John Robert Schrieffer. Theory of superconductivity. *Physical review*, 108(5):1175, 1957.

[67] W Kohn. Image of the Fermi surface in the vibration spectrum of a metal. *Physical Review Letters*, 2(9):393, 1959.

[68] Rudolf Ernst Peierls. *Quantum theory of solids*. Clarendon Press, 1996.

[69] Andrea Damascelli, Zahid Hussain, and Zhi-Xun Shen. Angle-resolved photoemission studies of the cuprate superconductors. *Reviews of modern physics*, 75(2):473, 2003.

[70] L Pintschovius. Electron-phonon coupling effects explored by inelastic neutron scattering. *physica status solidi (b)*, 242(1):30–50, 2005.

[71] Emmanouil Kioupakis, Patrick Rinke, André Schleife, Friedhelm Bechstedt, and Chris G Van de Walle. Free-carrier absorption in nitrides from first principles. *Physical Review B*, 81(24):241201, 2010.

[72] Jesse Noffsinger, Emmanouil Kioupakis, Chris G Van de Walle, Steven G Louie, and Marvin L Cohen. Phonon-assisted optical absorption in silicon from first principles. *Physical review letters*, 108(16):167402, 2012.

[73] Marios Zacharias, Christopher E Patrick, and Feliciano Giustino. Stochastic approach to phonon-assisted optical absorption. *Physical review letters*, 115(17):177401, 2015.

[74] Manuel Cardona and Mike LW Thewalt. Isotope effects on the optical spectra of semiconductors. *Reviews of modern physics*, 77(4):1173, 2005.

[75] NF Mott. The conductivity of metals. *Proceedings of the Physical Society*, 46(5):680, 1934.

[76] David Keith Chalmers MacDonald. *Thermoelectricity: an introduction to the principles*. Courier Corporation, 2006.

[77] Wu Li. Electrical transport limited by electron-phonon coupling from boltzmann transport equation: An ab initio study of Si, Al, and MoS_2. *Physical Review B*, 92(7):075405, 2015.

[78] M Omini and A Sparavigna. An iterative approach to the phonon Boltzmann equation in the theory of thermal conductivity. *Physica B: Condensed Matter*, 212(2):101–112, 1995.

[79] L Lindsay, DA Broido, and TL Reinecke. Ab initio thermal transport in compound semiconductors. *Physical Review B*, 87(16):165201, 2013.

[80] Te-Huan Liu, Jiawei Zhou, Bolin Liao, David J Singh, and Gang Chen. First-principles mode-by-mode analysis for electron-phonon scattering channels and mean free path spectra in GaAs. *Physical Review B*, 95(7):075206, 2017.

[81] Jinlong Ma, Arun S Nissimagoudar, and Wu Li. First-principles study of electron and hole mobilities of Si and GaAs. *Physical Review B*, 97(4):045201, 2018.

[82] Te-Huan Liu, Bai Song, Laureen Meroueh, Zhiwei Ding, Qichen Song, Jiawei Zhou, Mingda Li, and Gang Chen. Simultaneously high electron and hole mobilities in cubic boron-V compounds: BP, BAs, and BSb. *Physical Review B*, 98(8):081203, 2018.

[83] Samuel Poncé, Elena R Margine, and Feliciano Giustino. Towards predictive many-body calculations of phonon-limited carrier mobilities in semiconductors. *Physical Review B*, 97(12):121201, 2018.

[84] Jesse Noffsinger, Feliciano Giustino, Brad D Malone, Cheol-Hwan Park, Steven G Louie, and Marvin L Cohen. EPW: A program for calculating the electron-phonon coupling using maximally localized Wannier functions. *Computer Physics Communications*, 181(12):2140–2148, 2010.

[85] Samuel Poncé, Elena R Margine, Carla Verdi, and Feliciano Giustino. EPW: Electron-phonon coupling, transport and superconducting properties using maximally localized Wannier functions. *Computer Physics Communications*, 209:116–133, 2016.

[86] Philip B Allen. Improved callaway model for lattice thermal conductivity. *Physical Review B*, 88(14):144302, 2013.

[87] WJ Choyke and G Pensl. Physical properties of SiC. *Mrs Bulletin*, 22(3):25–29, 1997.

[88] Lyle Patrick, DR Hamilton, and WJ Choyke. Growth, luminescence, selection rules, and lattice sums of SiC with wurtzite structure. *Physical Review*, 143(2):526, 1966.

[89] Philip G Neudeck. Progress in silicon carbide semiconductor electronics technology. *Journal of Electronic Materials*, 24(4):283–288, 1995.

[90] Tianshi Wang, Zhigang Gui, Anderson Janotti, Chaoying Ni, and Prashant Karandikar. Strong effect of electron-phonon interaction on the lattice thermal conductivity in 3C-SiC. *Physical Review Materials*, 1(3):034601, 2017.

[91] Feng Yan, Jian H Zhao, and Gregory H Olsen. Demonstration of the first 4H-SiC avalanche photodiodes. *Solid-State Electronics*, 44(2):341–346, 2000.

[92] YH Zhu, JC Zhang, ZT Chen, and T Egawa. Demonstration on GaN-based light-emitting diodes grown on 3C-SiC/Si (111). *Journal of Applied Physics*, 106(12):124506, 2009.

[93] KP Schoen, Jerry M Woodall, James A Cooper, and Michael R Melloch. Design considerations and experimental analysis of high-voltage SiC Schottky barrier rectifiers. *IEEE Transactions on electron devices*, 45(7):1595–1604, 1998.

[94] P Alexandrov, JH Zhao, W Wright, M Pan, and M Weiner. Demonstration of 140 A, 800 V 4H-SiC pin/Schottky barrier diodes with multi-step junction termination extension structures. *Electronics Letters*, 37(18):1139–1140, 2001.

[95] PA Ivanov, ME Levinshtein, AK Agarwal, and JW Palmour. Transient characteristics of a 1.8 kV, 3.8 a 4H-SiC bipolar junction transistor. *Semiconductor science and technology*, 16(6):521, 2001.

[96] Anant K Agarwal, Pavel A Ivanov, Michael E Levinshtein, John W Palmour, Sergey L Rumyantsev, and Sei-Hyung Ryu. Turn-off performance of 2.6 kV 4H-SiC asymmetrical GTO thyristor. *Semiconductor science and technology*, 16(4):260, 2001.

[97] Michael E Levinshtein, Tigran T Mnatsakanov, Pavel A Ivanov, Anant K Agarwal, John W Palmour, Sergey L Rumyantsev, Aleksey G Tandoev, and Sergey N Yurkov. Temperature dependence of turn-on processes in 4H-SiC thyristors. *Solid-State Electronics*, 45(3):453–459, 2001.

[98] Mohit Bhatnagar and B Jayant Baliga. Comparison of 6H-SiC, 3C-SiC, and Si for power devices. *IEEE Transactions on electron devices*, 40(3):645–655, 1993.

[99] M Yamanaka, H Daimon, E Sakuma, S Misawa, and S Yoshida. Temperature dependence of electrical properties of n-and p-type 3C-SiC. *Journal of applied physics*, 61(2):599–603, 1987.

[100] T Tachibana, HS Kong, YC Wang, and RF Davis. Hall measurements as a function of temperature on monocrystalline SiC thin films. *Journal of applied physics*, 67(10):6375–6381, 1990.

[101] Matthias Roschke and Frank Schwierz. Electron mobility models for 4H, 6H, and 3C SiC [MESFETs]. *IEEE Transactions on Electron Devices*, 48(7):1442–1447, 2001.

[102] H-E Nilsson, U Englund, Mats Hjelm, E Bellotti, and K Brennan. Full band Monte Carlo study of high field transport in cubic phase silicon carbide. *Journal of applied physics*, 93(6):3389–3394, 2003.

[103] TT Mnatsakanov, LI Pomortseva, and SN Yurkov. Semiempirical model of carrier mobility in silicon carbide for analyzing its dependence on temperature and doping level. *Semiconductors*, 35(4):394–397, 2001.

[104] Enrico Bellotti, Hans-Erik Nilsson, Kevin F Brennan, and P Paul Ruden. Ensemble monte carlo calculation of hole transport in bulk 3C-SiC. *Journal of applied physics*, 85(6):3211–3217, 1999.

[105] Rimvydas Mickevičius and Jian H Zhao. Monte carlo study of electron transport in SiC. *Journal of applied physics*, 83(6):3161–3167, 1998.

[106] RP Joshi and DK Ferry. Calculations of the temperature and field dependent electronic mobility in β-SiC. *Solid-State Electronics*, 38(11):1911–1916, 1995.

[107] K Tsukioka, D Vasileska, and DK Ferry. An ensemble monte carlo study of high-field transport in β-SiC. *Physica B: Condensed Matter*, 185(1-4):466–470, 1993.

[108] Hubert Jan Van Daal. *Mobility of charge carriers in silicon carbide*. Philips Research Laboratories, 1965.

[109] Carla Verdi and Feliciano Giustino. Fröhlich electron-phonon vertex from first principles. *Physical review letters*, 115(17):176401, 2015.

[110] Jin-Jian Zhou and Marco Bernardi. Ab initio electron mobility and polar phonon scattering in GaAs. *Physical Review B*, 94(20):201201, 2016.

[111] Jinlong Ma, Yani Chen, and Wu Li. Intrinsic phonon-limited charge carrier mobilities in thermoelectric SnSe. *Physical Review B*, 97(20):205207, 2018.

[112] Te-Huan Liu, Jiawei Zhou, Mingda Li, Zhiwei Ding, Qichen Song, Bolin Liao, Liang Fu, and Gang Chen. Electron mean-free-path filtering in dirac material for improved thermoelectric performance. *Proceedings of the National Academy of Sciences*, 115(5):879–884, 2018.

[113] J Sjakste, N Vast, M Calandra, and F Mauri. Wannier interpolation of the electron-phonon matrix elements in polar semiconductors: Polar-optical coupling in GaAs. *Physical Review B*, 92(5):054307, 2015.

[114] Paolo Giannozzi, Stefano Baroni, Nicola Bonini, Matteo Calandra, Roberto Car, Carlo Cavazzoni, Davide Ceresoli, Guido L Chiarotti, Matteo Cococcioni, Ismaila Dabo, et al. QUANTUM ESPRESSO: a modular and open-source software project for quantum simulations of materials. *Journal of physics: Condensed matter*, 21(39):395502, 2009.

[115] John P Perdew and Alex Zunger. Self-interaction correction to density-functional approximations for many-electron systems. *Physical Review B*, 23(10):5048, 1981.

[116] A Taylor and RM Jones. The crystal structure and thermal expansion of cubic and hexagonal silicon carbide. *Silicon Carbide*, pages 147–161, 1960.

[117] D Bimberg, M Altarelli, and NO Lipari. A calculation of valence band masses, exciton and acceptor energies and the ground state properties of the electron-hole liquid in cubic SiC. *Solid State Communications*, 40(4):437–440, 1981.

[118] Michael E Levinshtein, Sergey L Rumyantsev, and Michael S Shur. *Properties of Advanced Semiconductor Materials: GaN, AIN, InN, BN, SiC, SiGe*. John Wiley & Sons, 2001.

[119] Brad D Malone and Marvin L Cohen. Quasiparticle semiconductor band structures including spin–orbit interactions. *Journal of Physics: Condensed Matter*, 25(10):105503, 2013.

[120] Martin Gmitra and Jaroslav Fabian. First-principles studies of orbital and spin-orbit properties of GaAs, GaSb, InAs, and InSb zinc-blende and wurtzite semiconductors. *Physical Review B*, 94(16):165202, 2016.

[121] J Kono, S Takeyama, H Yokoi, N Miura, M Yamanaka, M Shinohara, and K Ikoma. High-field cyclotron resonance and impurity transition in n-type and p-type 3C-SiC at magnetic fields up to 175 T. *Physical Review B*, 48(15):10909, 1993.

[122] Qichen Song, Te-Huan Liu, Jiawei Zhou, Zhiwei Ding, and Gang Chen. Ab initio study of electron mean free paths and thermoelectric properties of lead telluride. *Materials Today Physics*, 2:69–77, 2017.

[123] Jiawei Zhou, Hangtian Zhu, Te-Huan Liu, Qichen Song, Ran He, Jun Mao, Zihang Liu, Wuyang Ren, Bolin Liao, David J Singh, et al. Large thermoelectric power factor from crystal symmetry-protected non-bonding orbital in half-Heuslers. *Nature communications*, 9(1):1–9, 2018.

[124] Francis J DiSalvo. Thermoelectric cooling and power generation. *Science*, 285(5428):703–706, 1999.

[125] Yanzhong Pei, Aaron LaLonde, Shiho Iwanaga, and G Jeffrey Snyder. High thermoelectric figure of merit in heavy hole dominated PbTe. *Energy & Environmental Science*, 4(6):2085–2089, 2011.

[126] Wen Li, Linglang Zheng, Binghui Ge, Siqi Lin, Xinyue Zhang, Zhiwei Chen, Yunjie Chang, and Yanzhong Pei. Promoting SnTe as an eco-friendly solution for p-PbTe thermoelectric via band convergence and interstitial defects. *Advanced Materials*, 29(17):1605887, 2017.

[127] Raza Moshwan, Lei Yang, Jin Zou, and Zhi-Gang Chen. Eco-friendly SnTe thermoelectric materials: Progress and future challenges. *Advanced Functional Materials*, 27(43):1703278, 2017.

[128] Gangjian Tan, Fengyuan Shi, Jeff W Doak, Hui Sun, Li-Dong Zhao, Pengli Wang, Ctirad Uher, Chris Wolverton, Vinayak P Dravid, and Mercouri G Kanatzidis. Extraordinary role of Hg in enhancing the thermoelectric performance of p-type SnTe. *Energy & Environmental Science*, 8(1):267–277, 2015.

[129] Wei Liu, Xiaojian Tan, Kang Yin, Huijun Liu, Xinfeng Tang, Jing Shi, Qingjie Zhang, and Ctirad Uher. Convergence of conduction bands as a means of enhancing thermoelectric performance of n-type $Mg_2Si_{1-x}Sn_x$ solid solutions. *Physical review letters*, 108(16):166601, 2012.

[130] Jun Mao, Hee Seok Kim, Jing Shuai, Zihang Liu, Ran He, Udara Saparamadu, Fei Tian, Weishu Liu, and Zhifeng Ren. Thermoelectric properties of materials near the band crossing line in Mg_2Sn-Mg_2Ge-Mg_2Si system. *Acta Materialia*, 103:633–642, 2016.

[131] Yinglu Tang, Zachary M Gibbs, Luis A Agapito, Guodong Li, Hyun-Sik Kim, Marco Buongiorno Nardelli, Stefano Curtarolo, and G Jeffrey Snyder. Convergence of multi-valley bands as the electronic origin of high thermoelectric performance in $CoSb_3$ skutterudites. *Nature materials*, 14(12):1223–1228, 2015.

[132] Degang Zhao, Changwen Tian, Yunteng Liu, Chengwei Zhan, and Lidong Chen. High temperature sublimation behavior of antimony in $CoSb_3$ thermoelectric material during thermal duration test. *Journal of Alloys and Compounds*, 509(6):3166–3171, 2011.

[133] Chenguang Fu, Shengqiang Bai, Yintu Liu, Yunshan Tang, Lidong Chen, Xinbing Zhao, and Tiejun Zhu. Realizing high figure of merit in heavy-band p-type half-Heusler thermoelectric materials. *Nature communications*, 6(1):1–7, 2015.

[134] Kaiyang Xia, Pengfei Nan, Shihua Tan, Yumei Wang, Binghui Ge, Wenqing Zhang, Shashwat Anand, Xinbing Zhao, G Jeffrey Snyder, and Tiejun Zhu. Short-range order in defective half-Heusler thermoelectric crystals. *Energy & Environmental Science*, 12(5):1568–1574, 2019.

[135] Qinyi Qiu, Yintu Liu, Kaiyang Xia, Teng Fang, Junjie Yu, Xinbing Zhao, and Tiejun Zhu. Grain boundary scattering of charge transport in n-type (Hf, Zr) CoSb half-Heusler thermoelectric materials. *Advanced Energy Materials*, 9(11):1803447, 2019.

[136] MN Tripathi and CM Bhandari. High-temperature thermoelectric performance of Si-Ge alloys. *Journal of Physics: Condensed Matter*, 15(31):5359, 2003.

[137] Sang Il Kim, Kyu Hyoung Lee, Hyeon A Mun, Hyun Sik Kim, Sung Woo Hwang, Jong Wook Roh, Dae Jin Yang, Weon Ho Shin, Xiang Shu Li, Young Hee Lee, et al. Dense dislocation arrays embedded in grain boundaries for high-performance bulk thermoelectrics. *Science*, 348(6230):109–114, 2015.

[138] Lipeng Hu, Yang Zhang, Haijun Wu, Yamei Liu, Junqin Li, Jian He, Weiqin Ao, Fusheng Liu, Stephen John Pennycook, and Xierong Zeng. Synergistic compositional–mechanical–thermal effects leading to a record high zT in n-type V_2VI_3 alloys through progressive hot deformation. *Advanced Functional Materials*, 28(35):1803617, 2018.

[139] Hyun-Sik Kim, Nicholas A Heinz, Zachary M Gibbs, Yinglu Tang, Stephen D Kang, and G Jeffrey Snyder. High thermoelectric performance in $(Bi_{0.25}Sb_{0.75})_2Te_3$ due to band convergence and improved by carrier concentration control. *Materials Today*, 20(8):452–459, 2017.

[140] Juan Li, Xinyue Zhang, Zhiwei Chen, Siqi Lin, Wen Li, Jiahong Shen, Ian T Witting, Alireza Faghaninia, Yue Chen, Anubhav Jain, et al. Low-symmetry rhombohedral GeTe thermoelectrics. *Joule*, 2(5):976–987, 2018.

[141] Li-Dong Zhao, Gangjian Tan, Shiqiang Hao, Jiaqing He, Yanling Pei, Hang Chi, Heng Wang, Shengkai Gong, Huibin Xu, Vinayak P Dravid, et al. Ultrahigh power factor and thermoelectric performance in hole-doped single-crystal SnSe. *Science*, 351(6269):141–144, 2016.

[142] Pai-Chun Wei, Sriparna Bhattacharya, Yu-Fei Liu, Fengjiao Liu, Jian He, Yung-Hsiang Tung, Chun-Chuen Yang, Cheng-Rong Hsing, Duc-Long Nguyen, Ching-Ming Wei, et al. Thermoelectric figure-of-merit of fully dense single-crystalline SnSe. *ACS omega*, 4(3):5442–5450, 2019.

[143] BC Sales, D Mandrus, BC Chakoumakos, V Keppens, and JR Thompson. Filled skutterudite antimonides: Electron crystals and phonon glasses. *Physical Review B*, 56(23):15081, 1997.

[144] Holger Kleinke. New bulk materials for thermoelectric power generation: clathrates and complex antimonides. *Chemistry of materials*, 22(3):604–611, 2010.

[145] S Ishiwata, Y Shiomi, JS Lee, MS Bahramy, T Suzuki, M Uchida, R Arita, Y Taguchi, and Y Tokura. Extremely high electron mobility in a phonon-glass semimetal. *Nature materials*, 12(6):512–517, 2013.

[146] Jiawei Zhang, Lirong Song, and Bo Brummerstedt Iversen. Insights into the design of thermoelectric Mg_3Sb_2 and its analogs by combining theory and experiment. *NPJ Computational Materials*, 5(1):76, 2019.

[147] Xiaoxi Chen, Haijun Wu, Juan Cui, Yu Xiao, Yang Zhang, Jiaqing He, Yue Chen, Jian Cao, Wei Cai, Stephen J Pennycook, et al. Extraordinary thermoelectric performance in n-type manganese doped Mg_3Sb_2 Zintl: High band degeneracy, tuned carrier scattering mechanism and hierarchical microstructure. *Nano Energy*, 52:246–255, 2018.

[148] Jun Mao, Hangtian Zhu, Zhiwei Ding, Zihang Liu, Geethal Amila Gamage, Gang Chen, and Zhifeng Ren. High thermoelectric cooling performance of n-type Mg_3Bi_2-based materials. *Science*, 365(6452):495–498, 2019.

[149] Jiawei Zhang, Lirong Song, Georg KH Madsen, Karl FF Fischer, Wenqing Zhang, Xun Shi, and Bo B Iversen. Designing high-performance layered thermoelectric materials through orbital engineering. *Nature communications*, 7(1):1–7, 2016.

[150] A Bhardwaj and DK Misra. Enhancing thermoelectric properties of a p-type Mg_3Sb_2-based Zintl phase compound by Pb substitution in the anionic framework. *Rsc Advances*, 4(65):34552–34560, 2014.

[151] H Kaibe, Y Tanaka, M Sakata, and I Nishida. Anisotropic galvanomagnetic and thermoelectric properties of n-type Bi_2Te_3 single crystal with the composition of a useful thermoelectric cooling material. *Journal of Physics and Chemistry of Solids*, 50(9):945–950, 1989.

[152] Atsushi Togo, Laurent Chaput, and Isao Tanaka. Distributions of phonon lifetimes in Brillouin zones. *Phys. Rev. B*, 91:094306, Mar 2015.

[153] Juan Li, Shuqi Zheng, Teng Fang, Luo Yue, Shuai Zhang, and Guiwu Lu. Computational prediction of a high ZT of n-type Mg_3Sb_2-based compounds with isotropic thermoelectric conduction performance. *Physical Chemistry Chemical Physics*, 20(11):7686–7693, 2018.

[154] Kazuki Imasato, Stephen Dongmin Kang, and G Jeffrey Snyder. Exceptional thermoelectric performance in $Mg_3Sb_{0.6}Bi_{1.4}$ for low-grade waste heat recovery. *Energy & Environmental Science*, 12(3):965–971, 2019.

[155] Vijay Ponnambalam and Donald T Morelli. On the thermoelectric properties of Zintl compounds $Mg_3Bi_{2-x}Pn_x$ (Pn= P and Sb). *Journal of electronic materials*, 42(7):1307–1312, 2013.

[156] Matthias T Agne, Kazuki Imasato, Shashwat Anand, Kathleen Lee, Sabah K Bux, Alex Zevalkink, Alexander JE Rettie, Duck Young Chung, Mercouri G Kanatzidis, and G Jeffrey Snyder. Heat capacity of Mg_3Sb_2, Mg_3Bi_2, and their alloys at high temperature. *Materials Today Physics*, 6:83–88, 2018.

[157] GD Mahan. Figure of merit for thermoelectrics. *Journal of applied physics*, 65(4):1578–1583, 1989.

[158] Jun-ichi Tani, Masanari Takahashi, and Hiroyasu Kido. Lattice dynamics and elastic properties of Mg_3As_2 and Mg_3Sb_2 compounds from first-principles calculations. *Physica B: Condensed Matter*, 405(19):4219–4225, 2010.

[159] Wanyue Peng, Guido Petretto, Gian-Marco Rignanese, Geoffroy Hautier, and Alexandra Zevalkink. An unlikely route to low lattice thermal conductivity: Small atoms in a simple layered structure. *Joule*, 2(9):1879–1893, 2018.

[160] Jochen Heyd, Gustavo E Scuseria, and Matthias Ernzerhof. Hybrid functionals based on a screened Coulomb potential. *The Journal of chemical physics*, 118(18):8207–8215, 2003.

[161] Jochen Heyd and Gustavo E Scuseria. Efficient hybrid density functional calculations in solids: Assessment of the Heyd-Scuseria-Ernzerhof screened Coulomb hybrid functional. *The Journal of chemical physics*, 121(3):1187–1192, 2004.

[162] Juan E Peralta, Jochen Heyd, Gustavo E Scuseria, and Richard L Martin. Spin-orbit splittings and energy band gaps calculated with the Heyd-Scuseria-Ernzerhof screened hybrid functional. *Physical Review B*, 74(7):073101, 2006.

[163] Fabien Tran and Peter Blaha. Accurate band gaps of semiconductors and insulators with a semilocal exchange-correlation potential. *Physical review letters*, 102(22):226401, 2009.

[164] Wu Li, Natalio Mingo, Lucas Lindsay, David A Broido, Derek A Stewart, and Nebil A Katcho. Thermal conductivity of diamond nanowires from first principles. *Physical Review B*, 85(19):195436, 2012.

[165] Fanchen Meng, Jinlong Ma, Jian He, and Wu Li. Phonon-limited carrier mobility and temperature-dependent scattering mechanism of 3C-SiC from first principles. *Physical Review B*, 99(4):045201, 2019.

[166] David Leslie Greenaway and Günther Harbeke. Band structure of bismuth telluride, bismuth selenide and their respective alloys. *Journal of Physics and Chemistry of Solids*, 26(10):1585–1604, 1965.

[167] Herbert Fröhlich. Electrons in lattice fields. *Advances in Physics*, 3(11):325–361, 1954.

[168] Junsoo Park, Yi Xia, and Vidvuds Ozoliņš. High thermoelectric power factor and efficiency from a highly dispersive band in Ba_2BiAu. *Physical Review Applied*, 11(1):014058, 2019.

[169] Brian K Ridley. *Quantum processes in semiconductors*. Oxford University Press, 2013.

[170] Jorge Osvaldo Sofo and GD Mahan. Optimum band gap of a thermoelectric material. *Physical Review B*, 49(7):4565, 1994.

[171] LD Zhao, B-P Zhang, J-F Li, HL Zhang, and WS Liu. Enhanced thermoelectric and mechanical properties in textured n-type Bi_2Te_3 prepared by spark plasma sintering. *Solid State Sciences*, 10(5):651–658, 2008.

[172] LP Hu, XH Liu, HH Xie, JJ Shen, TJ Zhu, and XB Zhao. Improving thermoelectric properties of n-type bismuth-telluride-based alloys by deformation-induced lattice defects and texture enhancement. *Acta Materialia*, 60(11):4431–4437, 2012.

[173] Lipeng Hu, Tiejun Zhu, Xiaohua Liu, and Xinbing Zhao. Point defect engineering of high-performance bismuth-telluride-based thermoelectric materials. *Advanced Functional Materials*, 24(33):5211–5218, 2014.

[174] Masaro Yoshida, Takahiko Iizuka, Yu Saito, Masaru Onga, Ryuji Suzuki, Yijin Zhang, Yoshihiro Iwasa, and Sunao Shimizu. Gate-optimized thermoelectric power factor in ultrathin WSe_2 single crystals. *Nano letters*, 16(3):2061–2065, 2016.

[175] Kedar Hippalgaonkar, Ying Wang, Yu Ye, Diana Y Qiu, Hanyu Zhu, Yuan Wang, Joel Moore, Steven G Louie, and Xiang Zhang. High thermoelectric power factor in two-dimensional crystals of MoS_2. *Physical Review B*, 95(11):115407, 2017.

[176] Wen Huang, Haixia Da, and Gengchiau Liang. Thermoelectric performance of MX_2 (M= Mo, W; X= S, Se) monolayers. *Journal of Applied Physics*, 113(10):104304, 2013.

[177] Appala Naidu Gandi and Udo Schwingenschlögl. WS_2 as an excellent high-temperature thermoelectric material. *Chemistry of Materials*, 26(22):6628–6637, 2014.

[178] S Kumar and U Schwingenschlogl. Thermoelectric response of bulk and monolayer $MoSe_2$ and WSe_2. *Chemistry of Materials*, 27(4):1278–1284, 2015.

[179] Appala Naidu Gandi, Husam N Alshareef, and Udo Schwingenschlögl. Thermoelectric performance of the mxenes M_2Co_2 (M= Ti, Zr, or Hf). *Chemistry of Materials*, 28(6):1647–1652, 2016.

[180] Guanpeng Li, Kailun Yao, and Guoying Gao. Strain-induced enhancement of thermoelectric performance of TiS_2 monolayer based on first-principles phonon and electron band structures. *Nanotechnology*, 29(1):015204, 2017.

[181] HY Lv, WJ Lu, DF Shao, HY Lu, and YP Sun. Strain-induced enhancement in the thermoelectric performance of a ZrS_2 monolayer. *Journal of Materials Chemistry C*, 4(20):4538–4545, 2016.

[182] Jie Zhang, Xiaolin Liu, Yanwei Wen, Lu Shi, Rong Chen, Huijun Liu, and Bin Shan. Titanium trisulfide monolayer as a potential thermoelectric material: a first-principles-based boltzmann transport study. *ACS applied materials & interfaces*, 9(3):2509–2515, 2017.

[183] Bo Peng, Hao Zhang, Hezhu Shao, Ke Xu, Gang Ni, Jing Li, Heyuan Zhu, and Costas M Soukoulis. Chemical intuition for high thermoelectric performance in monolayer black phosphorus, α-arsenene and aw-antimonene. *Journal of Materials Chemistry A*, 6(5), 2018.

[184] Brahim Marfoua and Jisang Hong. High thermoelectric performance in hexagonal 2D $PdTe_2$ monolayer at room temperature. *ACS applied materials & interfaces*, 11(42):38819–38827, 2019.

[185] Elie A Moujaes and WA Diery. Thermoelectric properties of 1T monolayer pristine and Janus Pd dichalcogenides. *Journal of Physics: Condensed Matter*, 31(45):455502, 2019.

[186] Zahid Rashid, Arun S Nissimagoudar, and Wu Li. Phonon transport and thermoelectric properties of semiconducting Bi_2Te_2X (X= S, Se, Te) monolayers. *Physical Chemistry Chemical Physics*, 21(10):5679–5688, 2019.

[187] Bo Peng, Haodong Mei, Hao Zhang, Hezhu Shao, Ke Xu, Gang Ni, Qingyuan Jin, Costas M Soukoulis, and Heyuan Zhu. High thermoelectric efficiency in monolayer PbI_2 from 300 K to 900 K. *Inorganic Chemistry Frontiers*, 6(4):920–928, 2019.

[188] Xiwen Zhang, Chenhan Liu, Yi Tao, Yunhai Li, Yilv Guo, Yunfei Chen, Xiao Cheng Zeng, and Jinlan Wang. High ZT 2D thermoelectrics by design: Strong interlayer vibration and complete band-extrema alignment. *Advanced Functional Materials*, 30(22):2001200, 2020.

[189] Zhibin Gao and Jian-Sheng Wang. Thermoelectric penta-silicene with a high room-temperature figure of merit. *ACS Applied Materials & Interfaces*, 12(12):14298–14307, 2020.

[190] Siqi Lin, Wen Li, Zhiwei Chen, Jiawen Shen, Binghui Ge, and Yanzhong Pei. Tellurium as a high-performance elemental thermoelectric. *Nature communications*, 7(1):1–6, 2016.

[191] Zhili Zhu, Xiaolin Cai, Seho Yi, Jinglei Chen, Yawei Dai, Chunyao Niu, Zhengxiao Guo, Maohai Xie, Feng Liu, Jun-Hyung Cho, et al. Multivalency-driven formation of Te-based monolayer materials: a combined first-principles and experimental study. *Physical review letters*, 119(10):106101, 2017.

[192] Jinglei Chen, Yawei Dai, Yaqiang Ma, Xianqi Dai, Wingkin Ho, and Maohai Xie. Ultrathin β-tellurium layers grown on highly oriented pyrolytic graphite by molecular-beam epitaxy. *Nanoscale*, 9(41):15945–15948, 2017.

[193] Xiaochun Huang, Jiaqi Guan, Zijian Lin, Bing Liu, Shuya Xing, Weihua Wang, and Jiandong Guo. Epitaxial growth and band structure of te film on graphene. *Nano letters*, 17(8):4619–4623, 2017.

[194] Zhibin Gao, Fang Tao, and Jie Ren. Unusually low thermal conductivity of atomically thin 2D tellurium. *Nanoscale*, 10(27):12997–13003, 2018.

[195] Zhibin Gao, Gang Liu, and Jie Ren. High thermoelectric performance in two-dimensional tellurium: An ab initio study. *ACS applied materials & interfaces*, 10(47):40702–40709, 2018.

[196] Sitansh Sharma, Nirpendra Singh, and Udo Schwingenschlögl. Two-dimensional tellurene as excellent thermoelectric material. *ACS Applied Energy Materials*, 1(5):1950–1954, 2018.

[197] Wu Li, Jesús Carrete, and Natalio Mingo. Thermal conductivity and phonon linewidths of monolayer MoS_2 from first principles. *Applied Physics Letters*, 103(25):253103, 2013.

[198] Xiaokun Gu and Ronggui Yang. Phonon transport in single-layer transition metal dichalcogenides: A first-principles study. *Applied Physics Letters*, 105(13):131903, 2014.

[199] Bo Qiu, Zhiting Tian, Ajit Vallabhaneni, Bolin Liao, Jonathan M Mendoza, Oscar D Restrepo, Xiulin Ruan, and Gang Chen. First-principles simulation of electron mean-free-path spectra and thermoelectric properties in silicon. *EPL (Europhysics Letters)*, 109(5):57006, 2015.

[200] Feliciano Giustino. Electron-phonon interactions from first principles. *Reviews of Modern Physics*, 89(1):015003, 2017.

[201] Samuel Poncé, Wenbin Li, Sven Reichardt, and Feliciano Giustino. First-principles calculations of charge carrier mobility and conductivity in bulk semiconductors and two-dimensional materials. *Reports on Progress in Physics*, 83(3):036501, 2020.

[202] Andrea Marini, Conor Hogan, Myrta Grüning, and Daniele Varsano. Yambo: an ab initio tool for excited state calculations. *Computer Physics Communications*, 180(8):1392–1403, 2009.

[203] Peter E Blöchl. Projector augmented-wave method. *Physical review B*, 50(24):17953, 1994.

[204] Terry M Tritt and MA Subramanian. Thermoelectric materials, phenomena, and applications: a bird's eye view. *MRS bulletin*, 31(3):188–198, 2006.

[205] Jinlong Ma, Arun S Nissimagoudar, Shudong Wang, and Wu Li. High thermoelectric figure of merit of full-heusler Ba_2AuX (X= As, Sb, and Bi). *physica status solidi (RRL)–Rapid Research Letters*, page 2000084, 2020.

[206] Thibault Sohier, Davide Campi, Nicola Marzari, and Marco Gibertini. Mobility of two-dimensional materials from first principles in an accurate and automated framework. *Physical Review Materials*, 2(11):114010, 2018.

[207] Wenbin Li, Samuel Poncé, and Feliciano Giustino. Dimensional crossover in the carrier mobility of two-dimensional semiconductors: The case of InSe. *Nano Letters*, 19(3):1774–1781, 2019.

[208] Bolin Liao, Jiawei Zhou, Bo Qiu, Mildred S Dresselhaus, and Gang Chen. Ab initio study of electron-phonon interaction in phosphorene. *Physical Review B*, 91(23):235419, 2015.

[209] Long Cheng, Chenmu Zhang, and Yuanyue Liu. The optimal electronic structure for high-mobility 2D semiconductors: Exceptionally high hole mobility in 2D antimony. *Journal of the American Chemical Society*, 141(41):16296–16302, 2019.

[210] Samuel Poncé, Debdeep Jena, and Feliciano Giustino. Hole mobility of strained GaN from first principles. *Physical Review B*, 100(8):085204, 2019.

[211] Wenxu Zhang, Zhishuo Huang, Wanli Zhang, and Yanrong Li. Two-dimensional semiconductors with possible high room temperature mobility. *Nano Research*, 7(12):1731–1737, 2014.

[212] Yongqing Cai, Gang Zhang, and Yong-Wei Zhang. Polarity-reversed robust carrier mobility in monolayer MoS_2 nanoribbons. *Journal of the American Chemical Society*, 136(17):6269–6275, 2014.

[213] Tue Gunst, Troels Markussen, Kurt Stokbro, and Mads Brandbyge. First-principles method for electron-phonon coupling and electron mobility: Applications to two-dimensional materials. *Physical Review B*, 93(3):035414, 2016.

[214] Xiaodong Li, Jeffrey T Mullen, Zhenghe Jin, Kostyantyn M Borysenko, M Buongiorno Nardelli, and Ki Wook Kim. Intrinsic electrical transport properties of monolayer silicene and MoS_2 from first principles. *Physical Review B*, 87(11):115418, 2013.

[215] Yuma Nakamura, Tianqi Zhao, Jinyang Xi, Wen Shi, Dong Wang, and Zhigang Shuai. Intrinsic charge transport in stanene: Roles of bucklings and electron-phonon couplings. *Advanced Electronic Materials*, 3(11):1700143, 2017.

[216] Massimo V Fischetti and William G Vandenberghe. Mermin-wagner theorem, flexural modes, and degraded carrier mobility in two-dimensional crystals with broken horizontal mirror symmetry. *Physical Review B*, 93(15):155413, 2016.

[217] Guangzhao Qin, Qing-Bo Yan, Zhenzhen Qin, Sheng-Ying Yue, Ming Hu, and Gang Su. Anisotropic intrinsic lattice thermal conductivity of phosphorene from first principles. *Physical Chemistry Chemical Physics*, 17(7):4854–4858, 2015.

[218] Arun S Nissimagoudar, Jinlong Ma, Yani Chen, and Wu Li. Thermal transport in monolayer InSe. *Journal of Physics: Condensed Matter*, 29(33):335702, 2017.

[219] Tianqi Deng, Xue Yong, Wen Shi, Chee Kwan Gan, Wu Li, Kedar Hippalgaonkar, Jin-Cheng Zheng, Xiaobai Wang, Shuo-Wang Yang, Jian-Sheng Wang, et al. 2D single-layer π-conjugated Nickel Bis (dithiolene) complex: A good-electron-poor-phonon thermoelectric material. *Advanced Electronic Materials*, 5(4):1800892, 2019.

[220] Wu Li and Natalio Mingo. Thermal conductivity of fully filled skutterudites: Role of the filler. *Physical Review B*, 89(18):184304, 2014.

[221] Wu Li and Natalio Mingo. Lattice dynamics and thermal conductivity of skutterudites $CoSb_3$ and $IrSb_3$ from first principles: Why $IrSb_3$ is a better thermal conductor than $CoSb_3$. *Physical Review B*, 90(9):094302, 2014.

[222] Qian Wang, Lihong Han, Liyuan Wu, Tao Zhang, Shanjun Li, and Pengfei Lu. Strain effect on thermoelectric performance of InSe monolayer. *Nanoscale research letters*, 14(1):1–9, 2019.

[223] Cheng Chang, Minghui Wu, Dongsheng He, Yanling Pei, Chao-Feng Wu, Xuefeng Wu, Hulei Yu, Fangyuan Zhu, Kedong Wang, Yue Chen, et al. 3D charge and 2D phonon transports leading to high out-of-plane ZT in n-type SnSe crystals. *Science*, 360(6390):778–783, 2018.

[224] JL Zhang, CM Wang, CY Guo, XD Zhu, Y Zhang, JY Yang, YQ Wang, Z Qu, L Pi, Hai-Zhou Lu, et al. Anomalous thermoelectric effects of $ZrTe_5$ in and beyond the quantum limit. *Physical review letters*, 123(19):196602, 2019.

[225] Honghui Wang, Xigang Luo, Kunling Peng, Zeliang Sun, Mengzhu Shi, Donghui Ma, Naizhou Wang, Tao Wu, Jianjun Ying, Zhengfei Wang, et al. Magnetic field-enhanced thermoelectric performance in Dirac semimetal Cd_3As_2 crystals with different carrier concentrations. *Advanced Functional Materials*, 29(37):1902437, 2019.

[226] Shengying Yue, Hamid T Chorsi, Manik Goyal, Timo Schumann, Runqing Yang, Tashi Xu, Bowen Deng, Susanne Stemmer, Jon A Schuller, and Bolin Liao. Soft phonons and ultralow lattice thermal conductivity in the Dirac semimetal Cd_3As_2. *Physical Review Research*, 1(3):033101, 2019.

[227] Brian Skinner and Liang Fu. Large, nonsaturating thermopower in a quantizing magnetic field. *Science advances*, 4(5):eaat2621, 2018.

[228] JunSen Xiang, SiLe Hu, Meng Lyu, WenLiang Zhu, ChaoYang Ma, ZiYu Chen, Frank Steglich, GenFu Chen, and PeiJie Sun. Large transverse thermoelectric figure of merit in a topological Dirac semimetal. *Science China Physics, Mechanics & Astronomy*, 63(3):1–7, 2020.

[229] Enrique Muñoz and Rodrigo Soto-Garrido. Thermoelectric transport in torsional strained Weyl semimetals. *Journal of Applied Physics*, 125(8):082507, 2019.

[230] Ipsita Mandal and Kush Saha. Thermopower in an anisotropic two-dimensional Weyl semimetal. *Physical Review B*, 101(4):045101, 2020.

[231] Shin-ichiro Tamura. Isotope scattering of dispersive phonons in Ge. *Physical Review B*, 27(2):858, 1983.

[232] Anupam Kundu, Natalio Mingo, DA Broido, and DA Stewart. Role of light and heavy embedded nanoparticles on the thermal conductivity of SiGe alloys. *Physical Review B*, 84(12):125426, 2011.

[233] Georg KH Madsen and David J Singh. Boltztrap. A code for calculating band-structure dependent quantities. *Computer Physics Communications*, 175(1):67–71, 2006.